

SVERDRUP BALANCE AND THREE DIMENSIONAL VARIABILITY OF THE MERIDIONAL OVERTURNING CIRCULATION

A thesis submitted to the
School of Environmental Sciences
of the
University of East Anglia
in partial fulfilment of the requirements for the degree of
Doctor of Philosophy

By
Matthew David Thomas
September 2012

© This copy of the thesis has been supplied on condition that anyone who consults it is understood to recognise that its copyright rests with the author and that use of any information derived there from must be in accordance with current UK Copyright Law. In addition, any quotation or extract must include full attribution.

Abstract

Two numerical models are used to gain an understanding of the spatial structure of Atlantic Meridional Overturning Circulation changes and the dynamical framework within which those changes occur.

Sverdrup balance is studied using the 16 year ECCO-GODAE state estimation. It is shown to hold well in the interior subtropics when integrating to a mid-depth level and when considered at spatial scales larger than approximately 5° . Outside of the subtropics, in western boundary currents and at short spatial scales, significant departures occur mostly due to a failure in the assumption that there is a level of no motion that can be integrated to and partly due to the assumption of linear vorticity. Sverdrup balance is reached when enough time is allowed for the ocean to adjust to forcing by the propagation of baroclinic Rossby waves.

A climate change simulation of the HiGEM high resolution coupled climate model is used to investigate to what extent a 30% reduction in the deep southward transport is balanced by a reduction in the northward flowing surface western boundary transport, or an increase in the southward upper interior transport. It is found that a reduction in the southwards deep transport is balanced solely by a weakening of the northward surface western boundary current. This is consistent with Sverdrup balance holding to a good approximation in the basin interior.

Overturning calculations in depth space and density space are found to differ within the subpolar gyre of a 120 year Control simulation of HiGEM. Depth space overturning is found to depend strongly on the transports of the Labrador current, which are strengthened by a spin-up of the horizontal subpolar gyre. Density space overturning is found to be strongly dependent on the densities of the Labrador Current, which increase following Labrador Sea water mass transformation and strong flow through the Denmark Straits.

Acknowledgements

My supervisory team has been fantastic. Agatha de Boer, David Stevens, and Helen Johnson, you have each brought so much to the project and I am sincerely grateful to each of you. In particular, I want to say a massive thank you to Agatha for being so dedicated and for having always made time. My thanks also go to the other members of the UEA and Oxford departments for providing great discussions and for generally creating such an inspiring atmosphere. I am grateful also to the Department of Environmental Sciences for funding me.

To my Mum, my brother James, my Grandad and the rest of my family, your consistent support means so much to me, thank you. A great deal of appreciation also goes to my friends. Rob and Paul, my time at UEA most certainly wouldn't have been the same without you. Helen and Sam, your hospitality and friendship at Oxford has meant a lot. Thank you Louise, Bekah, Jake and the rest of my friends for having never failed to take my mind off work. I dedicate this to my Dad, who is my inspiration.

Contents

Abstract	iii
Acknowledgements	v
1 Introduction	1
1.1 The Atlantic Meridional Overturning Circulation	1
1.1.1 The AMOC as part of a 3D System	4
1.1.2 AMOC Variability	6
1.1.3 Meridional Adjustment and Intergyre Differences	9
1.2 Sverdrup balance	12
1.2.1 Derivation	12
1.2.2 Relevance to the AMOC	16
1.2.3 Evidence for Sverdrup Balance and its Assumptions	17
1.3 Ocean General Circulation Models	21
1.4 Motivation and Thesis Outline	23
2 Sverdrup Balance in the Subtropical Ocean	27
2.1 Introduction	27
2.2 Theoretical Discussion	30
2.3 Model Description	31
2.4 Methodology	32
2.4.1 Calculation of Vorticity in ECCO	32
2.4.2 Defining the Study Domain	33
2.4.3 Sverdrup Balance Metrics	33
2.5 Validity of Sverdrup Balance	35
2.6 Deep Ocean Processes	44
2.7 Steady State Averaging Time	48
2.8 Discussion and Conclusions	51

3	Subtropical Upper Ocean Manifestations of a Reducing AMOC	55
3.1	Introduction	55
3.2	Model Description	57
3.3	Sverdrup Balance in the Subtropical Atlantic Ocean	59
3.4	Transport trends	64
3.5	Changes in Ocean Properties	72
3.6	Pacific Ocean transports	75
3.7	Heat transport changes	78
3.8	HiGEM steady state averaging time	80
3.9	Conclusions	81
4	An Investigation into Subpolar Variability of the AMOC	85
4.1	Introduction	85
4.2	Model Description	89
4.3	Coordinate representations of the AMOC	90
4.4	Variability of the AMOC	96
4.5	Meridional coherence of the AMOC	100
4.6	Depth space and density space overturning differences	106
4.6.1	High Latitude Ocean Processes	106
4.6.2	High Frequency AMOC variability	108
4.6.3	Low Frequency AMOC variability	109
4.7	Mechanisms of Subpolar AMOC Variability	115
4.8	Conclusions	119
5	Conclusions and Discussion	125
5.1	Sverdrup balance	125
5.2	Subtropical Manifestations of a Reducing AMOC	126
5.3	Subpolar AMOC Variability	128
5.4	Wider context and Future Work	129
6	Appendices	135
6.1	Appendix A: finding a Level of No Motion in ECCO-GODAE	135
6.2	Appendix B: calculating vertical velocities in ECCO-GODAE	142
6.3	Appendix C: statistical methods	146
6.3.1	Statistical significance of a trend in data containing autocorrelation	146

6.3.2	Statistical significance of a correlation between data containing autocorrelation	147
6.4	Appendix D: Glossary of Terms in Equations	150
6.5	Appendix E: Glossary of Acronyms and Abbreviations	152
7	Bibliography	155

Chapter 1

Introduction

This thesis is concerned with the sources and mechanisms related to changes in Meridional Overturning Circulation, with a particular focus on the North Atlantic. This chapter first describes the Atlantic Meridional Overturning Circulation (AMOC) along with what is known about its variability. A description of Sverdrup balance is then given and its relationship to the AMOC is outlined.

1.1 The Atlantic Meridional Overturning Circulation

The Atlantic Meridional Overturning Circulation (AMOC) dominates the Atlantic ocean northwards transport of heat and is an important contributor to European climate (Vellinga and Wood, 2002; Wood et al., 2003). Estimates from observations at 26°N in the Atlantic estimate the heat transport to exceed 1 PW (e.g. Ganachaud and Wunsch, 2003), and at 35°N the ocean is estimated to make up more than 20% of the combined atmosphere-ocean northward heat transport (Trenberth and Caron, 2001).

The AMOC summarises the system of currents that together comprise a net northwards upper ocean transport and southwards deep ocean transport. As buoyant upper ocean water flows northwards from low latitudes, heat and freshwater is gradually lost to the atmosphere until, on reaching high latitudes, it sinks into the deep ocean and flows southwards to complete an overturning cell (Ganachaud and Wunsch, 2000).

Climate models predict a slowing down of the AMOC over the 21st cen-

tury due to increases in high latitude buoyancy (Cubasch et al., 2001; IPCC, 2007). The added input of heat and fresh water (due to the melting of land and sea ice and the enhanced hydrological cycle) predicted for a warmer climate is expected to inhibit convective overturning and slow the flux of upper ocean water into the deep ocean. Such a disruption to the northward transport of heat would likely have important consequences for European climate (Vellinga and Wood, 2002). Following evidence that warming (Levitus et al., 2005) and freshening (Dickson et al., 2002; Boyer et al., 2007) has taken place in the North Atlantic over the last 50 years, there is some concern that an AMOC reduction could have already started (Lozier et al., 2010). However, although it has been suggested based on five hydrographic snapshots that the AMOC has slowed by 30% over the last 50 years (Bryden et al., 2005), the consensus is that the AMOC has not yet undergone any change (Searl et al., 2007; Wunsch and Heimbach, 2006).

The AMOC, denoted as a two dimensional streamfunction $\psi(y, z)$, is defined as the double integral of the meridional velocity at each latitude, or

$$\psi(y, z) = \int_z^0 \int_{x_{east}(y,z)}^{x_{west}(y,z)} v \, dx \, dz, \quad (1)$$

where v is the meridional velocity at cartesian location (x, y, z) . Horizontal and vertical integration limits are respectively from the eastern ($x_{east}(y, z)$) and western ($x_{west}(y, z)$) boundaries, and from depth z to the surface. This is known as depth space overturning. Alternatively, the AMOC can be calculated in density coordinates (density space) by using potential density, σ , as a vertical coordinate instead of z . The coordinates in equation (1) therefore become (x, y, σ) , which is a more relevant depiction of overturning since ocean transport predominantly takes place along density contours, not depth contours. Water masses of different density that flow in opposing directions at the same depth do not cancel out in density space as they do in depth space, but instead lead to density space overturning.

Figure 1.1 shows an example of the annual mean AMOC, in (a) latitude-depth space and (b) latitude-density space, from a density coordinate ocean model (based on the Princeton Ocean Model) with units marked in Sverdrups (Sv; $1 \text{ Sv} = 10^6 \text{ m}^3 \text{ s}^{-1}$). Zonally-integrated meridional mass transport, which follows streamlines, is northwards in the upper (low density)

ocean, southwards in the deep (dense) ocean and near-vertical at high latitudes. In density space, the continuous increase in density of the lightest waters between tropical and subpolar latitudes is clear. The AMOC strength is usually taken to be the maximum streamfunction at each latitude. Although there is a clear single overturning cell in the annual means of Figure 1.1, significant variability can be seen at smaller scales. The maximum strength of the AMOC in the two coordinate representations only differ appreciably in the SPG and to the north of it, where zonal density gradients are relatively strong (Zhang, 2010). Most studies to date have used the depth space definition, and accordingly discussions of the AMOC throughout this section refer to depth space overturning, unless stated otherwise.

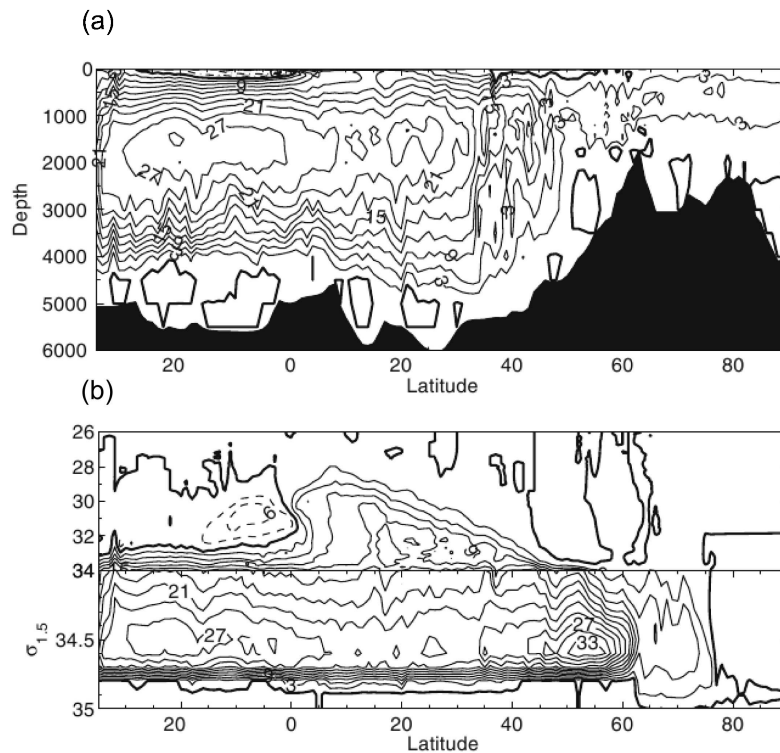


Figure 1.1: Annual mean climatological AMOC in (a) depth space and (b) density space (see text), from an ocean model. Units are in Sverdrups (Sv; $1 \text{ Sv} = 10^6 \text{ m}^3 \text{ s}^{-1}$). (Figure and caption from Bailey et al., 2005).

The traditional view of the AMOC is the ‘global ocean conveyor’ first described by Broecker (1987), which depicts the AMOC as a single coherent and continuous overturning cell. Recent developments, however, are revealing that the AMOC is a complex system undergoing large temporal

fluctuations (Cunningham et al., 2007) that vary with latitude (Lozier et al., 2010; Bingham et al., 2007) with complicated impacts on the distribution of heat throughout the Atlantic (Zhai et al., 2011). Variability arises through an interplay of the currents in the full 3D system that is currently not well understood (Lozier, 2010). Therefore, if the full implications of a possible future slowdown of the AMOC are to be determined then a better understanding of the 3D spatial structure of current variability will be required.

1.1.1 The AMOC as part of a 3D System

Derived according to equation (1), the AMOC is a 2D projection of the mass transports of the individual currents. Figure 1.2(a) shows a simplified schematic of the major horizontal currents (from Rahmstorf, 1997). The northwards flowing Gulf Stream (GS) splits roughly equally into the southwards subtropical gyre (STG) circulation and the northwards North Atlantic Current (NAC; or North Atlantic Drift as in Figure 1.2a). Convective mixing and downwelling at high latitudes then sources the southwards Deep Western Boundary Current (DWBC; marked in Figure 1.2(a) as North Atlantic Deep Water (NADW) to represent the dominant water mass composition).

The locations where surface water is able to reach high enough densities to allow convective mixing are known to be localised to specific regions of the high latitude ocean (e.g. Kuhlbrodt et al., 2007). These are primarily the Nordic Seas, the Irminger Sea and the Labrador Sea and are sourced by the NAC by northwards transport across the Greenland-Scotland Ridge (GSR) and cyclonic transport around the subpolar gyre (SPG). The NAC water in each case increases in density through water mass transformation (Medhaug et al., 2011) which, together with convective processes, leads to dense and deep water formation. Deep water formed in the Nordic seas eventually flows back across the GSR into the SPG as overflow via the Denmark Straits (DS) and Iceland-Scotland ridge, joining deep water from the Irminger and Labrador Sea convection sites to make up the deep water of the North Atlantic. The largest fraction of dense water ends up in the DWBC, which eventually transports water southwards to lower latitudes and eventually to the Southern Ocean. Observations suggest the DWBC is composed of approximately one third Labrador Sea water, one third GSR overflow water

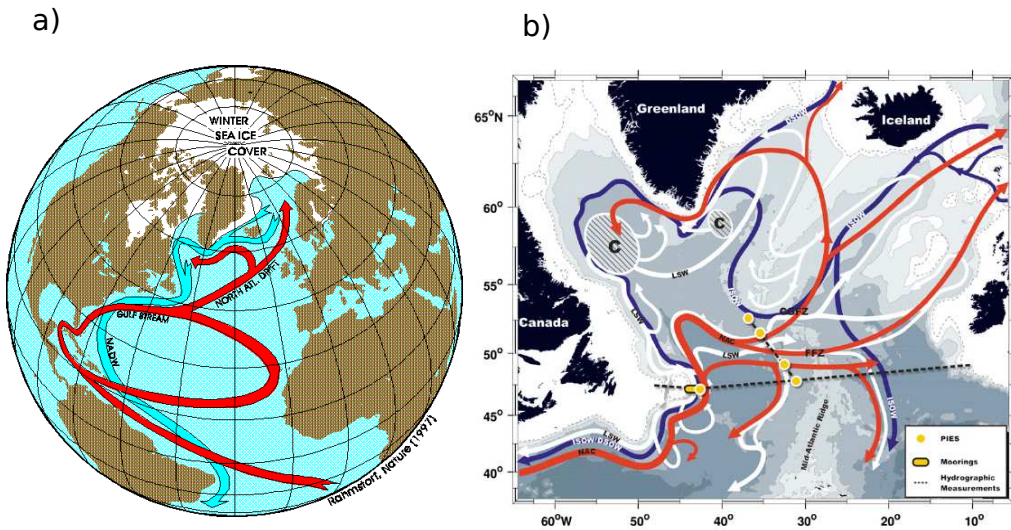


Figure 1.2: (a) Schematic of the major currents in the Atlantic (Rahmstorf, 1997). (b) Schematic of the currents in the northern North Atlantic. NAC: North Atlantic Current, LSW: Labrador Sea Water, ISOW: Iceland-Scotland Overflow Water, DSOW: DS Strait Overflow Water, C: convection regions. Red arrows depict the pathways of the NAC, the blue arrows depict the pathways of deep water formed in the Nordic Seas and white arrows depict the pathways of deep water formed in the SPG. (Figure and caption from Rhein et al., 2011).

and one third water entrained from the surroundings by the dense overflow water (Dickson and Brown, 1994). Figure 1.2(b) schematically represents the complicated possible pathways of the light and dense currents in the North Atlantic.

To compensate for the vertical mass flux into the deep ocean, water is returned to the upper ocean by Ekman induced upwelling in the Southern Ocean (Toggweiler and Samuels, 1995) and through diapycnal mixing that takes place in regions that are distributed throughout the ocean (Munk and Wunsch, 1998). Northwards transport into the equatorial North Atlantic from the South Atlantic northwards STG circulation completes the overturning cell. Figure 1.3 (from Kuhlbrodt et al., 2007) summarises the main processes that maintain the vertical structure of the AMOC, overlain onto the zonal mean density structure (determined from Levitus, 1982).

How the strength and variability of the AMOC is set by the sum of the various currents and processes is not yet fully understood (Lozier, 2010; Kuhlbrodt et al., 2007). However, there are indications that AMOC strength is in part determined by the strengths of convective mixing (Böning et al.,

2006; Latif et al., 2006), the DS overflow (Biaostoch et al., 2008; Gregory et al., 2005), diapycnal mixing (Munk and Wunsch, 1998) and Southern Ocean Ekman induced upwelling (Toggweiler and Samuels, 1995). Causes of AMOC variability remain poorly understood partly because of the complex spatial distribution and variable nature of the currents and processes involved.

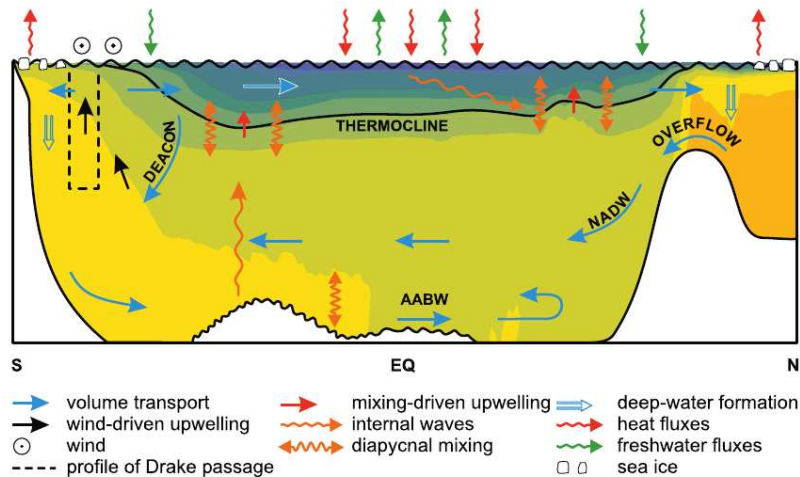


Figure 1.3: Idealized meridional section representing a zonally averaged picture of the Atlantic Ocean. Straight arrows sketch the AMOC. The color shading depicts a zonally averaged density profile derived from hydrographic data (Levitus, 1982). The two main upwelling mechanisms, wind-driven and mixing-driven, are displayed. Wind-driven upwelling is a consequence of a northward flow of the surface waters in the Southern Ocean, the Ekman transport, that is driven by strong westerly winds. Mixing along the density gradient, called diapycnal mixing, causes mixing-driven upwelling; this is partly due to internal waves triggered at the oceans boundaries. Deepwater formation (DWF) occurs in the high northern and southern latitudes, creating North Atlantic Deep Water (NADW) and Antarctic Bottom Water (AABW), respectively. The freshly formed NADW has to flow over the shallow sill between Greenland, Iceland, and Scotland. (Figure and caption from Kuhlbrodt et al., 2007).

1.1.2 AMOC Variability

Recent studies from the RAPID hydrographic observation programme (e.g. Kanzow et al., 2007) have revealed that the AMOC at 26.5°N undergoes large fluctuations (with a peak-to-peak range of approximately 30 Sv) on weekly to intra-annual timescales (e.g. Cunningham et al., 2007). Ocean

models suggest that large AMOC variability exists at timescales of up to multi-decadal in period (Hodson and Sutton, 2012; Bailey et al., 2005). These timescales are evident in Figure 1.4, a latitude versus time plot of the maximum AMOC in a 100 year climate model integration.

Short timescale variability is largely due to Ekman transport and eddy variability (Bjastoch et al., 2008). Ekman transport fluctuations directly modify the ageostrophic meridional transport (which is compensated barotropically at depth; Jayne and Marotzke, 2001), whilst eddies modify the eastern to western boundary density gradients and therefore the geostrophic currents. Long timescale variability is mostly the result of relatively slow oceanic adjustment mechanisms (e.g. Hodson and Sutton, 2012) that respond to atmospheric forcing such as the NAO. The NAO is characterised by the sea-level pressure difference between Iceland (the Iceland low) and the Azores (the Azores high) in the North Atlantic and is important for setting the strength and position of the westerly winds (Hurrell, 1995). By modifying the wind, the NAO directly affects the shape and strength of the SPG circulation (Rhein et al., 2011) and the net surface heat loss/gain from the ocean surface. Such changes are coupled to a number of processes (and those processes to each other) that can affect the strength of the AMOC.

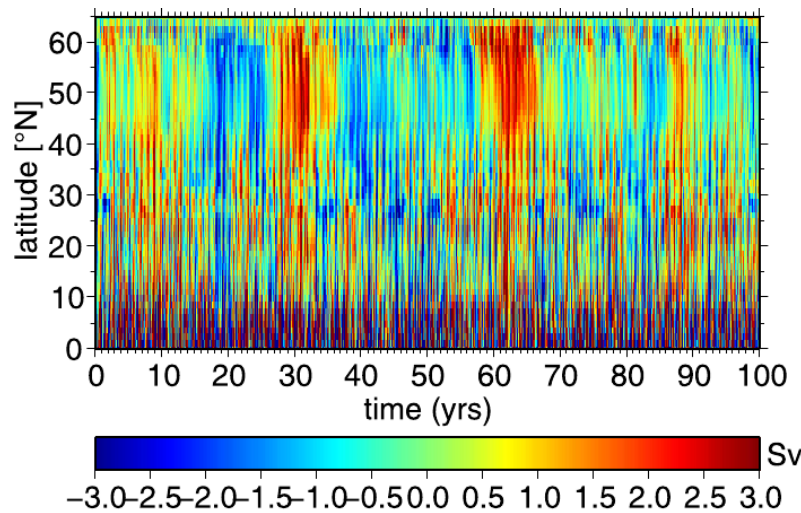


Figure 1.4: The AMOC strength displayed as a latitude-time plot and calculated as the maximum streamfunction between 100 and 1000 m depth, of a 100 year integration of a 1.25° coupled climate model (Figure adapted from Bingham et al., 2007).

The index dubbed the SPG strength (calculated as the basin-maximum

barotropic streamfunction, where the depth integrated meridional velocity equals the zonal derivative of the streamfunction) is commonly used to summarise the strength of the anti-clockwise circulation of the SPG. Proxies for the SPG strength observed from altimeter sea surface height data have shown the SPG strength is related to the NAO (Böning et al., 2006) and correlates to the maximum AMOC at 40°N (Zhang, 2008). A correlation between the maximum AMOC and the SPG strength is perhaps surprising at first since the SPG strength is a measure of the horizontal, and not vertical, circulation. They are related in part through vertical convective mixing that modifies the doming of the isopycnal structure and which in turn modifies the horizontal geostrophic flow (Häkkinen and Rhines, 2004; Kieke et al., 2007). Resultant geostrophic changes are such that convergent flow occurs in the upper ocean whilst divergent flow occurs at depth. This leads to downwelling (Marotzke and Scott, 1999), and therefore an increased DWBC strength and increased AMOC. Deep density anomalies then impose a negative feedback on the AMOC, on a cycle of approximately 10 years, by increasing (decreasing) the stratification and therefore suppressing (enhancing) convection. This has been reported in climate models (Hodson and Sutton, 2012) and in observations (Robson et al., 2012).

The SPG strength relates also to the horizontal extent (or size) of the SPG (Hátún et al., 2005). Though commonly attributed to fluctuations in the NAO, the SPG extent has recently been related to the strength of the wind stress curl (Häkkinen et al., 2011) and to negative feedback that arises due to preconditioned water masses that form under a persistent NAO (Lohmann et al., 2009). The effect of a contraction in the SPG extent is to allow more warm and salty water of STG origin to penetrate northwards along the eastern boundary (this process is described schematically in Figure 1.5; from Hátún et al., 2005). Alterations of the temperature and salinity of the north east Atlantic are likely to directly impact the AMOC by altering water mass transformation rates within the SPG and by modifying eastern boundary densities (Lozier et al., 2010). Additionally, that part of the warm salty water which crosses the DSR into the Nordic seas goes on to form the highest density waters of North Atlantic origin, since the salt remains once the water has cooled (Hátún et al., 2005). On re-entering the subpolar gyre this high density water then flows cyclonically around the basin and

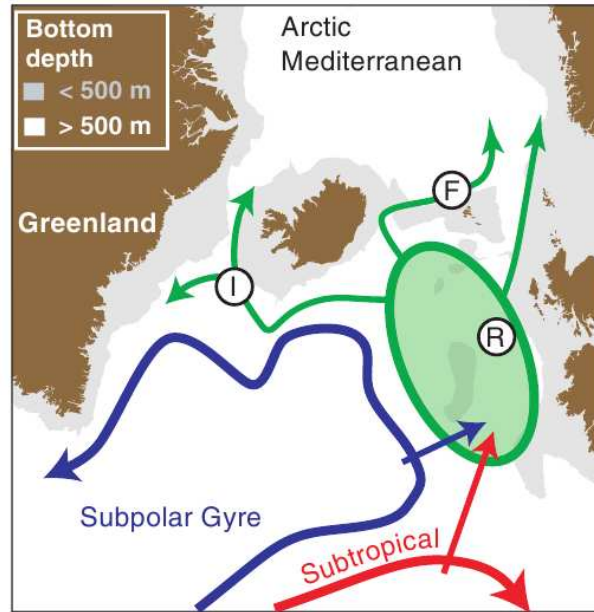


Figure 1.5: Schematic of the circulation features that regulate the quantity of STG origin water in the north east Atlantic. Green shading shows where subpolar and subtropical waters meet and mix, and subsequently flow into the Nordic Seas. From hydrographic data obtained in the Rockall Trough (R), Faroe Current (F), and Irminger Current (I) (Figure and caption from Hátún et al., 2005).

into the lower limb of the DWBC, strengthening the AMOC. It has been suggested that this will have a stabilising effect on the increasing volumes of freshwater observed in the region (Boyer et al., 2007) that might weaken convective activity and the AMOC (Hátún et al., 2005).

1.1.3 Meridional Adjustment and Intergyre Differences

A large part of AMOC variability is initiated at high latitudes and subsequently transmitted to lower latitudes through meridional adjustment processes (e.g. Hodson and Sutton, 2012). The fastest of these processes occurs by the equatorwards propagation of Kelvin waves that modify the east west pressure gradients as they travel down the coast (Johnson and Marshall, 2002). This process has been noted in both low (Johnson and Marshall, 2002) and high (Roussenov et al., 2008; Bingham et al., 2007) resolution models. On reaching the equator, the Kelvin waves propagate eastwards and then northwards up the eastern boundary where they excite westward propagating Rossby waves that bring the interior ocean into adjustment on

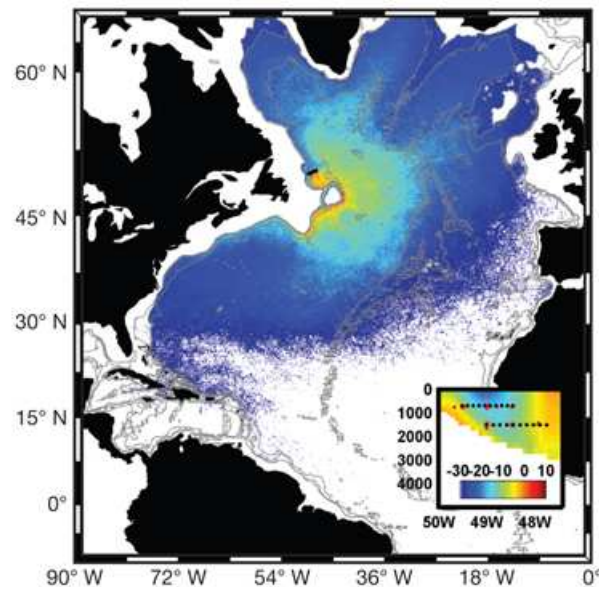


Figure 1.6: A 2D histogram map of the locations, after 15 years, of 7280 e-floats released into a $1/12^\circ$ eddy resolving ocean model. Floats were released at 50°N (marked by the black line), at which the cross sectional velocities are displayed in the inset. Units are probability. (Figure and caption from Bower et al., 2009).

longer timescales (that vary with latitude in accordance with the latitude dependent Rossby wave phase speed). Slower meridional adjustment occurs following advection of water masses along the western boundary (Marotzke and Klinger, 2000; Smethie et al., 2000; Bailey et al., 2005).

Although AMOC anomalies are transmitted from high to low latitudes, recent developments have revealed a distinct difference between the variability taking place at subpolar and subtropical latitudes (Lozier et al., 2010). These different timescales and magnitudes of variability can be seen in Figure 1.4 (Bingham et al., 2007). The mechanisms that lie behind the latitudinal dependence of AMOC variability are not well understood. Some possibilities are the latitudinal dependence of the Rossby wave phase speed (Bingham et al., 2007), the Ekman transport and the eddy variability (Bjastoch et al., 2008).

Observations of RAFOS floats have revealed a discontinuity in the DWBC inter-gyre advective pathway (Bower et al., 2009). It has been a commonly held belief that the DWBC is a continuous conduit of water from high to low latitudes, dominating the southwards cross-gyre export of cold water.

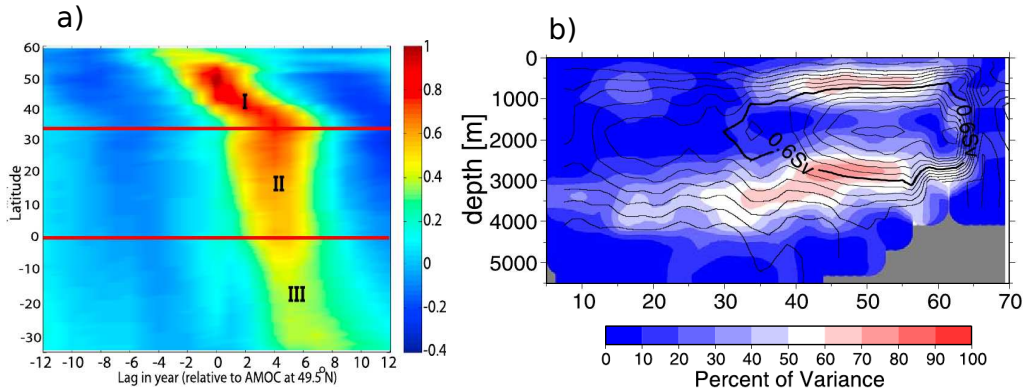


Figure 1.7: (a) Lagged correlations of the latitude dependent AMOC and the AMOC strength at 49.5°N from a 1000 year control simulation of a 1° ocean model (Zhang, 2010). (b) The first mode EOF of interannually low pass filtered AMOC in a 100 year run of a 1.25° coupled climate model (Bingham et al., 2007).

Instead of staying in the path of the DWBC, however, floats have been observed to routinely break away from the western boundary near to Flemish Cap (situated at approximately 47°N). Of those floats that continued southwards the dominant pathway was through the interior down to a latitude of approximately 35°N . However, most floats at Flemish Cap recirculated northwards and remained in the SPG. Simulated e-floats released into a numerical model support these findings (Bower et al., 2009; Getzlaff et al., 2006), and indicate that eddies are largely responsible for separating water from the boundary current (Gary et al., 2011). The locations of 7280 e-floats after 15 years of a $1/12^{\circ}$ numerical simulation are represented in Figure 1.6 (from Bower et al., 2009), a 2D normalised histogram map of e-floats released in the DWBC near 50°N . The subpolar recirculation and southwards interior pathways are well captured by the model. Whether complicated inter-gyre pathways are partly responsible for the latitudinal variation seen in Figure 1.4 is not clear, though it has been suggested that the interior pathways cause a slowdown in the meridional transmission of AMOC anomalies between latitudes 50°N and 34°N (Zhang, 2010).

This discussion has shown that the AMOC does not appear to behave according to the simple conveyor belt view of Broecker (1987). However, when considered on inter-annual timescales numerical models do reveal an underlying meridionally coherent structure to AMOC variations (Zhang, 2010; Bingham et al., 2007). Figure 1.7(a) shows that AMOC variabil-

ity is correlated, at appropriate time lag, with the AMOC at 49.5°N at all latitudes of the Atlantic when considered in density space coordinates (Zhang, 2010). The first mode Empirical Orthogonal Function (EOF) of the AMOC that is shown in Figure 1.4, also shows a consistent overturning cell (displayed in latitude-depth coordinates) when low pass filtered at one year period (Figure 1.7b). Note, however, that the models used to reach this conclusion are of coarse resolution and thereby do not resolve eddies, which have been shown to play an important role in determining some North Atlantic transport pathways (Gary et al., 2011).

1.2 Sverdrup balance

1.2.1 Derivation

In this section Sverdrup balance is discussed, which may act as a constraint on where AMOC changes can take place. Sverdrup balance equates the time-mean wind stress curl and depth-integrated meridional ocean transport. A part of its significance is that, where it is valid to a good order of approximation, the time-mean meridional transport can be estimated from a quantity that is routinely collected by satellites. A derivation of Sverdrup balance starts from the horizontal momentum equations in cartesian coordinates,

$$\partial_t u - fv = -\frac{1}{\rho_0} \partial_x p + A_h \nabla_h^2 u + \partial_z(A_v \partial_z u) - (\mathbf{u} \cdot \nabla) u, \quad (2)$$

$$\partial_t v + fu = -\frac{1}{\rho_0} \partial_y p + A_h \nabla_h^2 v + \partial_z(A_v \partial_z v) - (\mathbf{u} \cdot \nabla) v, \quad (3)$$

where f is the Coriolis parameter, p is the pressure, ρ_0 is a constant reference density (under the Boussinesq approximation), $\mathbf{u} = (u, v, w)$ is the velocity vector, A_h and A_v are the horizontal and vertical viscosity coefficients respectively, and $\nabla_h^2 = \partial_x^2 + \partial_y^2$. The first terms of equations (2) and (3) represent the local acceleration, the remaining terms represent acceleration due to Coriolis (second term), pressure gradients (third term), lateral viscosity (fourth term), vertical viscosity (fifth term) and advection (sixth term).

Considering only depths that lie below the Ekman layer and assum-

ing that frictional and advection terms are negligible and that the ocean reaches steady state on long time averages, equations (2) and (3) reduce to geostrophic balance, which can be written in vector form as,

$$f\hat{\mathbf{k}} \times \mathbf{u}_g = -\frac{1}{\rho_0}\nabla_h p, \quad (4)$$

where $\mathbf{u}_g = (u_g, v_g)$ is the geostrophic velocity vector and ∇_h is the horizontal gradient operator. The terms \mathbf{u}_g and p here represent the time-mean geostrophic velocity and pressure respectively. Taking the vertical component of the curl of equation (4), and invoking continuity ($\partial_x u + \partial_y v + \partial_z w = 0$), leads to linear vorticity balance for an incompressible flow,

$$\beta v_g = f \partial_z w, \quad (5)$$

where $\beta = \partial_y f$, v_g is the meridional geostrophic velocity and w is the vertical velocity. This linear vorticity balance describes how meridional velocities are produced as a result of stretching and squashing of the water column.

Integrating equation (5) from the bottom of the Ekman layer to a mid-depth, h , and incorporating $w_E = \hat{\mathbf{k}} \cdot \nabla \times (\boldsymbol{\tau}_s / \rho_0 f)$, where w_E is the vertical velocity at the base of the Ekman layer and $\boldsymbol{\tau}_s$ is the surface wind stress, gives

$$V_g = \frac{f}{\beta} \left(\hat{\mathbf{k}} \cdot \nabla \times \left(\frac{\boldsymbol{\tau}_s}{\rho_0 f} \right) - w_h \right), \quad (6)$$

where V_g is the meridional geostrophic transport and w_h is the vertical velocity at the integration depth. Assuming that the depth integrated transport is dominated by the geostrophic and Ekman terms, the total depth integrated transport, from the surface, s , to h is $V = V_g + V_E$, where $V_E = \tau_s^x / \rho_0 f$ is the Ekman layer meridional transport and τ_s^x is the zonal component of the surface wind stress. V can therefore be written

$$V = \frac{1}{\rho_0 \beta} \hat{\mathbf{k}} \cdot \nabla \times \boldsymbol{\tau}_s - \frac{f}{\beta} w_h. \quad (7)$$

The first two terms in equation (7) together form Sverdrup balance, which is valid if the depth h is a level of no motion (LONM) at which the vertical velocities are small and the non-linear vorticity terms are negligible. Since the assumptions that go into Sverdrup balance (or linear vorticity

balance) can never be perfect it becomes necessary, in any study aiming to quantify how good the balance is, to define a threshold at which the balance of terms can be said to hold to a good order of approximation. In this study, ‘a good order of approximation’ is defined as being achieved when the magnitude of the difference of the Sverdrup balance terms is approximately 30% or less of the magnitude of the wind stress curl term i.e. when the non-Sverdrup terms are 30% of the size of the Sverdrup wind forcing term. Like this the Sverdrup balance terms are the dominant balance in the depth integrated vorticity equation.

A qualitative description of the mechanism behind Sverdrup balance can be gained from a consideration of the conservation of potential vorticity,

$$\text{PV} = \frac{f + \zeta}{H_i}, \quad (8)$$

where $\zeta = \hat{\mathbf{k}} \cdot \nabla \times \mathbf{u}$ is the relative vorticity and H_i is the height of a column of water. It follows that the wind stress curl causes Ekman pumping/suction that creates vortex squashing/stretching and changes H_i . If we consider ζ to be small in equation (8), as in the geostrophic interior where the Rossby number is much smaller than 1, then in order to conserve potential vorticity vortex stretching must be compensated by meridional flow to change f (Figure 1.8). In an analogous process, vertical velocities may also be induced by interaction between deep flow and topography.

The deep vortex stretching related to the interaction between horizontal flow and topography is dubbed bottom pressure torque (BPT). Close to the ocean floor any interaction between currents and bottom topography can lead to BPT. The BPT is defined as $\hat{\mathbf{k}} \cdot \nabla \times (p_b \nabla H)$, where p_b represents pressure at the ocean floor and H is the ocean depth, and is derived as the curl of the full-depth integrated pressure term in the momentum equation (Hughes and de Cuevas, 2001). It can be shown using the kinematic boundary condition ($w_b = \mathbf{u} \cdot \nabla H$) that in a geostrophic flow,

$$\text{BPT} = -fw_b, \quad (9)$$

where w_b is the vertical velocity at the bottom (Lu and Stammer, 2004; Spence et al., 2012). Hence any non-zero BPT can lead to vertical velocities and accordingly to vortex stretching. This then induces meridional

velocities, a process analogous to the action of wind stress curl on the upper ocean. It is possible then to have upper and lower dynamical regimes, each creating meridional flows through vortex stretching. If independent of each other, one would lie above and one below a LONM, the former driven by wind (and in Sverdrup balance) and the latter driven by BPT. Conversely, should these transports overlap for some depths then there will not be a LONM that can be vertically integrated to and Sverdrup balance will break down. Mid-depth vertical velocities small enough to permit a good order of Sverdrup balance have been reported in hydrographic observations in the Pacific at 24°N (Hautala et al., 1994) and over approximately 40% of the subtropical oceans in a state estimation product (Wunsch, 2011).

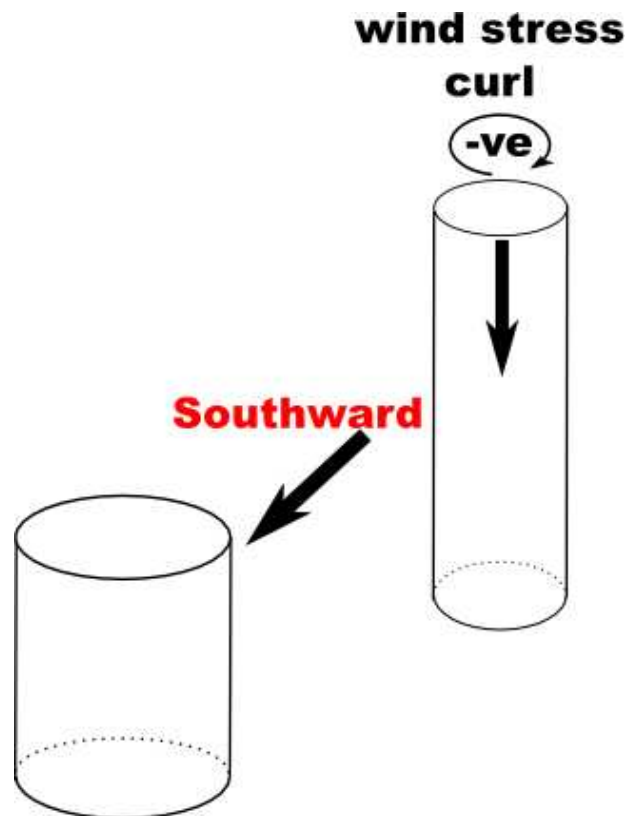


Figure 1.8: The dynamical mechanism behind Sverdrup balance. Wind Stress curl at the surface of the ocean drives Ekman pumping/suction (vertical arrow) that squashes/stretches the water column and changes its potential vorticity. The water column therefore changes latitude in order to conserve potential vorticity.

It is known that Sverdrup balance breaks down in the western boundary current where the assumptions, that the vorticity equation is linear and

that there is a LONM, break down (Roemmich and Wunsch, 1985; Bryan et al., 1995). This western boundary breakdown extends as far as the Antilles Current, which should not be included as part of an interior ocean in Sverdrup balance (Schmitz et al., 1992). Sverdrup balance is also not expected to hold polewards of the subtropical gyre because of barotropic flows (Hughes and de Cuevas, 2001). Whilst Sverdrup balance is possible in a barotropic flow over a flat seabed (as long as all of the transport is a result of wind forcing; Anderson and Gill, 1975), topographic interaction with the horizontal flow field forces vertical velocities that induce BPT and thereby invalidate Sverdrup balance.

1.2.2 Relevance to the AMOC

The relevance of the Sverdrup balance to the AMOC is that it might be expected to act as a constraint on where long time period AMOC changes can manifest themselves in the subtropics (de Boer and Johnson, 2007). Figure 1.9 depicts a zonal cross section of the subtropical North Atlantic currents in their present state (scenario a) and in two possible future climate change scenarios where a reduction in deep transport is compensated by an increase in the interior ocean transport (scenario b) or a reduction in the northwards upper ocean western boundary transport (scenario c). If the ocean is in Sverdrup balance, and the wind stress curl over the subtropical gyre (the regions where Sverdrup balance is expected to hold) is the same, then the zonally integrated southwards subtropical gyre transport must also be the same in all scenarios. A deep transport reduction would then by necessity be compensated by a reduction in the Gulf Stream transport such that scenario (b) is not a possible eventuality (de Boer and Johnson, 2007). This could have implications for the design of AMOC observing arrays in the subtropics, since it would mean that changes in the AMOC would be manifested entirely on the western boundary. Changes in the southward gyre transport may perhaps be measured via the wind stress curl.

Despite the potential importance of Sverdrup balance to the circulation there is not much evidence to support that its assumptions are valid in the subtropical ocean. This is partly because of an absence of long term measurements of the interior flow available during past studies of Sverdrup balance. In particular, it is not fully known if Sverdrup balance holds well

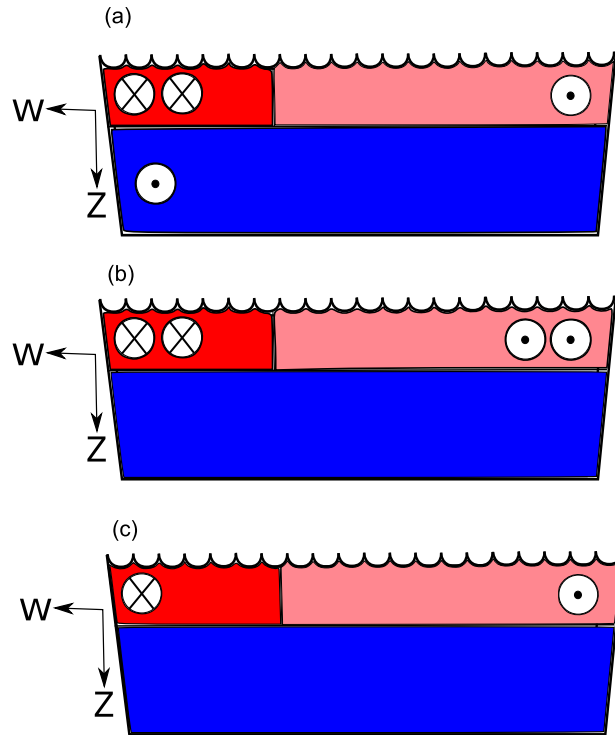


Figure 1.9: Schematic cross section of the Subtropical North Atlantic currents in (a) the present ocean state and in two possible future reduced AMOC states where a southwards deep transport (blue box) reduction is compensated by (b) an increase in the upper interior ocean (pink box) northwards transport and (c) a decrease in western boundary (red box) northwards transport. Arrows into and out of the page represent transport direction within each domain. More arrows indicates a stronger transport.

enough to act as a zonal constraint on where AMOC changes can occur (Wunsch, 2011), or how the validity of Sverdrup balance to describe the global circulation might change under a changing climate with a different stratification.

1.2.3 Evidence for Sverdrup Balance and its Assumptions

Studies undertaken to assess the validity of Sverdrup balance in hydrographic data suggest the subtropical upper interior layer is in Sverdrup balance to a good order of approximation over horizontal scales of about a few degrees or more, but not at shorter scales (Hautala et al., 1994; Roemmich and Wunsch, 1985). The zonally integrated Sverdrup balance, as summarised by Schmitz et al. (1992) from a variety of observational studies

(Leetmaa et al., 1977; Leetmaa and Bunker, 1978; Roemmich and Wunsch, 1985; Leetmaa and Bunker, 1978), appears to hold at 24°N with a 17 Sv upper interior transport that is balanced by 30 Sv northwards Florida Current and 13 Sv southwards deep transport.

An analysis into the assumption that the time mean vorticity is linear has suggested nonlinear vorticity terms can be significant in the top 500 m of the interior subtropics in state estimation data (Lu and Stammer, 2004). At depths below the thermocline the time mean linear vorticity balance holds reasonably well in mooring data (Bryden, 1980) and in a state estimation product (Lu and Stammer, 2004). Conversely, linear vorticity was observed to hold poorly in the deep ocean in hydrographic data (Wunsch and Roemmich, 1985). However, hydrographic data provides only a snapshot and so may not give a true impression of the time mean state. Although mid-depth linear vorticity appears to hold relatively well, vertical velocities were found to be in the opposite direction to the Ekman pumping direction in a 243 day mean at an ocean mooring site situated in the interior subtropical North Atlantic (Bryden, 1980). In such a case the system would appear to be dominated not by the Ekman pumping but by BPT.

In an idealised stratified ocean model with topography and forced by wind, bottom flow is first set up by barotropic Rossby waves (RW) and then cut off by the propagation of baroclinic RW modes that eventually confine the flow to an upper layer without altering the depth-integrated transport (Anderson and Killworth, 1977; Hughes and de Cuevas, 2001). This process of baroclinic adjustment continually further confines the flow to a thinner layer by the passing of the higher order modes. Any upper layer pressure gradients then do not penetrate as far as the sea floor and therefore do not induce BPT. It might therefore be expected that the topography becomes important at mid-latitudes and higher when the flow speed becomes comparable with the first baroclinic RW phase speed (Hughes and de Cuevas, 2001). When this happens the system becomes equivalent-barotropic (the direction of the bottom velocities matches that of the surface velocities) since it is no longer able to confine the barotropic response to an upper layer by baroclinic adjustment. This view is supported by the results from a linear wind driven analytical model with continuous stratification and realistic bathymetry (Marshall and Stephens, 2001). In this model the depth

integrated flow follows f contours in the interior subtropics but at higher latitude it follows f/H contours, indicating flow interaction with topography.

A comparison between the latitudinally dependent RW phase speed and the background flow might, therefore, conceivably set the location of the northern and southern boundaries (one per hemisphere) of the region where Sverdrup balance may hold to a good approximation. Polewards of these latitudes Sverdrup balance would break down, whilst equatorward of these latitudes the RW phase speed would set the amount of averaging time required before steady state is reached. This time scale would progressively increase polewards from the equator in accordance with the RW phase speed.

Modelling studies that are forced only by wind without the presence of an overturning (Anderson and Killworth, 1977; Marshall and Stephens, 2001) ignore the potential for sustained interaction between deep currents and topography. The presence of AMOC related deep currents could conceivably induce non-negligible BPT in the subtropical ocean. Scaling arguments have been used to show that vertical velocities at the sea floor could be large enough to bring into question the plausibility of Sverdrup balance even in the subtropics (Wunsch and Roemmich, 1985). This supports conclusions drawn from the time-mean vertical velocities taken at an ocean mooring site in the deep interior ocean (Bryden, 1980) and in localised regions in high resolution numerical models (Bryan et al., 1995; Hughes and de Cuevas, 2001). Figure 1.10 identifies strong BPT in the interior subtropical Pacific of a $1/4^\circ$ resolution model (Hughes and de Cuevas, 2001). Although high values of BPT appear only in specific regions of the subtropics, they could potentially rule out the possibility of a zonally integrated Sverdrup balance should they be included in the vertical integration used to form Sverdrup balance. AMOC changes would then not necessarily be restricted to the western boundary as depicted in Figure 1.9. If high BPT exists at the ocean floor then the upper ocean may only be in zonally integrated Sverdrup balance if a mid-depth LONM was everywhere to lie between the upper and lower dynamical regimes. Exactly such a situation has been observed in hydrographic data of the North Pacific (Hautala et al., 1994).

A recent study by Wunsch (2011) has used the ECCO-GODAE state estimation to conclude that a depth may be found in many regions of the

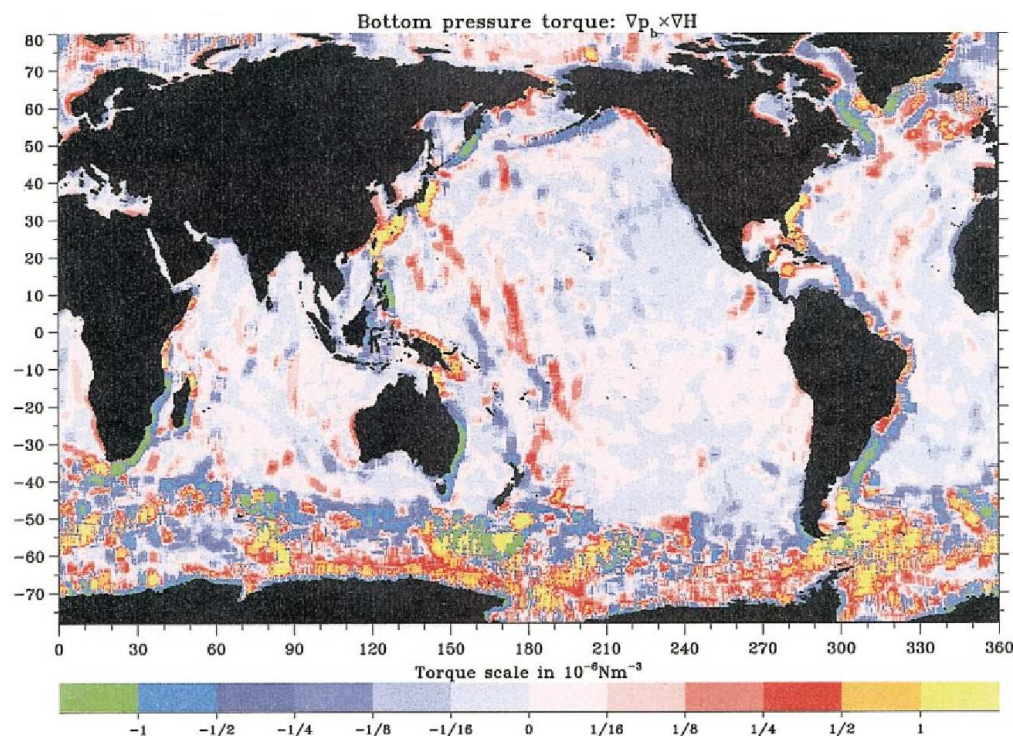


Figure 1.10: The BPT ($\hat{\mathbf{k}} \cdot \nabla \times (p_b \nabla H)$); see section 1.2.1) in a $1/4^\circ$ numerical model. Values are smoothed by 4° longitude by 1.75° latitude. The contour interval changes from $5 \times 10^6 \text{ m}^3 \text{ s}^{-1}$ north of 40°S to $15 \times 10^6 \text{ m}^3 \text{ s}^{-1}$ south of that latitude, in order to represent both gyre circulations and the ACC on the same plot. Units are 10^{-6} N m^3 . (Figure and caption from Hughes and de Cuevas, 2001).

subtropical ocean at which the vertical velocities become sufficiently small to be considered a LONM and for the ocean to be in Sverdrup balance (defined according to those regions where $f w_{115m} / \beta - V_g$ is 0.1 Sv or less (where w_{115m} is the vertical velocity at 115 m depth), and where the vertical velocity at the integration depth is $< 10^{-8} \text{ m s}^{-1}$ or less when considered on scales greater than 5°). A state estimation uses the so-called adjoint to include all available ocean observations into a model solution whilst retaining dynamical consistency. Figure 1.11 (from Wunsch, 2011) shows a 16 year mean of $f w_{115m} / \beta - V_g$ (see section 1.2.1) integrated from the surface to a reference level defined to be where the vertical velocities are smallest. Vertical velocities at 117 m are assumed to represent the Ekman pumping. Transports are multiplied by the grid width at each location to give units of Sverdrups. The regions of the ocean that are not considered to be in Sverdrup balance according to the above criteria are blanked out. Large

areas in Figure 1.11 that lie close to the eastern boundary of each ocean basin are considered to be out of Sverdrup balance, potentially indicating that zonally integrated Sverdrup balance is not valid.

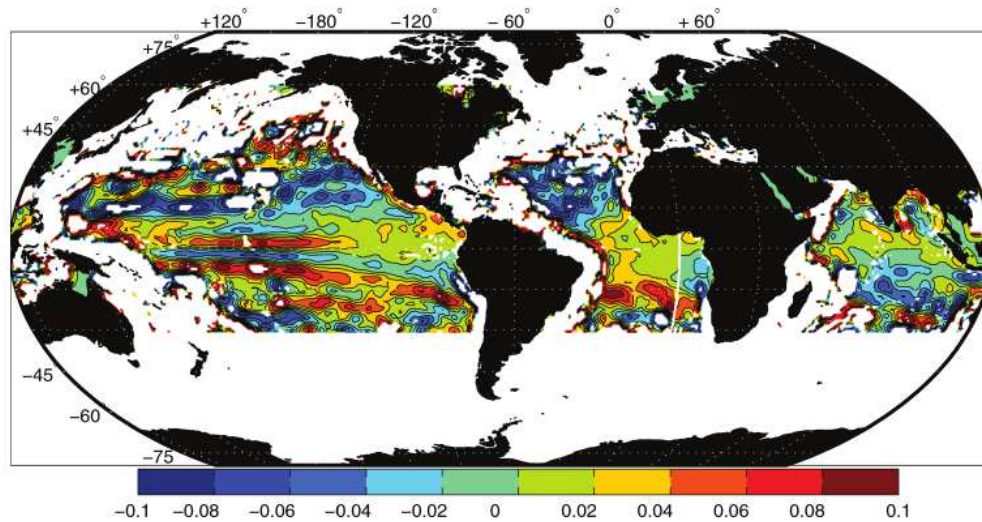


Figure 1.11: $fw_{115m}/\beta - V_g$ in Sverdrups per degree of separation. Regions where values are greater than 0.1 Sv and where vertical velocities exceed 10^{-8} m s^{-1} are masked to indicate they are not in Sverdrup balance. (Figure and caption from Wunsch, 2011).

1.3 Ocean General Circulation Models

Ocean General Circulation Models (OGCM's) enable us to study the ocean globally, with uniform data resolution in space and time. For this reason they are a particular advantage when observations are often not synoptic and are collected using a range of methodologies. The self consistent nature of OGCM's can be a particular advantage when observational estimates can sometimes come with assumptions regarding the consistency between observations that might be disparate in time or collected under a different methodology to other data used for comparison. Climate runs of OGCM's can be particularly useful for predicting the ocean response to e.g. the warming influence of increasing greenhouse gas concentrations. Running an OGCM under prescribed forcing scenarios can indicate which processes and regions are likely to show change, providing a starting place for the design of observational programmes or mitigation policy.

Using models to first gain a sufficient understanding of a system can be very advantageous when used to support observations (which can be very expensive to collect). For example they may aid in the design of an observational setup (e.g. Hirschi et al. (2003) in the design of the RAPID transatlantic array (Kanzow et al., 2007)), indicate a region or process requiring more detailed investigation or expand upon a limited number of observations (e.g. Bower et al., 2009).

While an increasing model fidelity to real world processes is being achieved with an increase in temporal and spatial resolution, the great computational requirements for long (decadal and greater) period global simulations in GCM's (such as those used in this study) limits the resolution, typically, to non-eddy resolving. These models instead rely on parameterisations of many unresolved ocean processes (Griffies, 2004). Despite this, state of the art climate models are able to exhibit similar magnitudes and patterns of decadal variability as seen in observations (e.g. Delworth and Mann, 2000). However, it is important to be aware of some of their shortcomings:

- Models with resolved eddies have been shown to better represent the time-mean and variable structure of the AMOC (Marsh et al., 2009). Eddies affect the AMOC by modifying the east-west density gradient in the ocean (Bjastoch et al., 2008), but also the pathways of currents (Gary et al., 2011) and recirculations (Lozier, 2010).
- High latitude processes associated with deep water formation require submesoscale resolution (Bjastoch et al., 2008). Problems in representation of these processes hold even for the highest resolution models, particularly in their representation of overflows (e.g. Cunningham and Marsh, 2010). The result can be a too-shallow overturning (Saunders et al., 2008).
- Kelvin wave speeds are impacted by spatial resolution, and have too-slow propagation speed at approximately non-eddy permitting resolutions (e.g. Hodson and Sutton, 2012).
- Unrealistic topography can lead to under or over representations of the width of particular Straits that are important for the climate system, such as the Florida Straits or Denmark Straits. This can lead to

erroneous estimations of mass transport in these regions (Shaffrey et al., 2009).

- Deep ocean circulation is too weak in almost all ocean models because of the long model spin-up time required for the deep ocean to reach equilibrium (Wunsch, 2011).
- Atmosphere-ocean-ice interactions are climatically important due to their importance for setting the global circulation, but often occur on smaller spatial scales than those typically resolved by OGCM's.

1.4 Motivation and Thesis Outline

Recent advances have revealed a complicated spatially and temporally varying AMOC (Bingham et al., 2007; Lozier et al., 2010) that is dependent on poorly understood components of the 3D ocean circulation (Lozier, 2010). It has now been observed that AMOC fluctuations equal in magnitude to the time-mean AMOC strength are common place at 26.5°N on time scales between weekly and intra-annual in period (Cunningham et al., 2007; McCarthy et al., 2012). Furthermore, climate models predict that large AMOC variability extends into time scales that exceed decadal in period (Biastoch et al., 2008; Hodson and Sutton, 2012; Medhaug et al., 2011). The variability arises initially through atmospheric forcing, but it is modulated by complex mechanisms such as deep water formation (Kieke et al., 2009) and slow adjustment processes (Hodson and Sutton, 2012). In light of possible future anthropogenic CO₂ induced reductions in AMOC strength, if the full implications of a weakening are to be predicted and understood then an understanding must be had on the 3D components of current variability. This includes gaining an understanding of the natural fluctuations of the AMOC, which must be accounted for when diagnosing climate change trends, and determining where AMOC changes might manifest themselves, which would have implications for purposes of detection and monitoring of the AMOC.

In the North Atlantic subtropical gyre a reducing AMOC might manifest itself in the upper ocean as a weakening of the northwards western boundary current or as a strengthening of the southwards gyre flow. If Sverdrup balance is valid in the interior subtropics, any changes in the southwards

gyre flow must be consistent with changes in the wind. Climate model simulations do not predict a strengthening of North Atlantic zonal wind stresses but rather a weakening of the trade winds and polewards shift of the westerlies (Lu et al., 2008). The implication is for a weakened wind stress curl which, along with an ocean that is in Sverdrup balance, implies reduced western boundary transports would occur under a future AMOC reduction. However, the extent to which Sverdrup balance holds in the ocean remains uncertain (Wunsch, 1996), particularly the extent to which it might constrain a future AMOC change. As well as providing insight into an important theory of the time mean ocean circulation, a detailed analysis of Sverdrup balance could provide a dynamical framework within which to hypothesise how a potential AMOC change might manifest itself in the subtropical gyre. Such a hypothesis is testable within a climate change scenario of a coupled climate model.

The complexity of the AMOC variability and its adjustment processes makes it difficult to isolate the sources of its variability. In particular, long time scales of up to decadal in period remain poorly understood partly because of the lack of observations that cover such periods and the high computational cost of running realistic ocean models over these time scales. Studies that have focused on inter-annual to decadal scale variability have revealed that the high latitude North Atlantic ocean is important for the AMOC (e.g. Gregory et al., 2005; Latif et al., 2006). Many of these investigations, however, were made using a depth space calculation of overturning. With evidence that the variability and meridional adjustment of the AMOC are best represented in density space (Mauritzen and Häkkinen, 1999; Zhang, 2010), there is a need to further study how the AMOC is manifested at high latitudes and how these manifestations differ between depth and density space representations of overturning. Improvements in our understanding of the mechanisms of decadal variability could help improve the interpretation of the causes and implications of variability in observational records as well as aid in the development of decadal prediction systems of future climate, which currently do not accurately hindcast North Atlantic AMOC changes (Smith et al., 2007).

In this thesis, an investigation based on 16 years of the ECCO-GODAE state estimation product will first be made into how well Sverdrup balance

describes the ocean circulation on various space and time scales. Chapter 3 will then address where in the subtropical ocean of an eddy permitting coupled climate model a decreasing AMOC will be spatially manifested, and whether these changes take place within a framework that is consistent with Sverdrup balance and geostrophic balance. In chapter 4 an analysis is made into the variability of the AMOC on inter-annual to decadal periods, with a particular emphasis on subpolar variability. The analysis includes an investigation into the high latitude processes that are important for AMOC variability in depth and density space, and the mechanisms by which these processes impact the AMOC are outlined. Chapter 5 concludes the thesis. Appendices are provided in chapter 6, which includes a glossary of acronyms and mathematical terms.

Chapter 2

Sverdrup Balance in the Subtropical Ocean

2.1 Introduction

Sverdrup balance has become one of the most important underpinnings for modern oceanic theory. It describes a simple yet powerful balance between the wind stress curl and the meridional transport in the ocean. The original theory was validated using thermal-wind geostrophic currents calculated relative to an assumed level of no motion (LONM) at 500 db (Sverdrup, 1947), although this choice of LONM and other assumptions may have led to a fortuitous match (Leetmaa et al., 1981). Later studies have highlighted the need to test the assumptions that are made in the formulation of Sverdrup balance, i.e. that there is a LONM to integrate to and that the ocean vorticity balance is approximately linear (Wunsch and Roemmich, 1985; Lu and Stammer, 2004).

The validity of Sverdrup balance to describe the subtropical gyre circulation has been addressed in a number of observational and modelling studies. Many of these have focused on only barotropic considerations (Zhang and Vallis, 2007; Hughes and de Cuevas, 2001), specific regions (Schmitz et al., 1992; Hautala et al., 1994), or instantaneous sections (Wunsch and Roemmich, 1985). Although these offer useful insights into the dynamics of the subtropical circulation, there have been few studies that address Sverdrup balance globally and the sensitivity of its assumptions to varying choices of integration depth and temporal/spatial averaging scales.

Studies of Sverdrup balance using hydrographic data have suggested that the interior subtropical upper ocean (from the surface to approximately 1 km depth) is in Sverdrup balance to a good order of approximation when considered over horizontal scales of about a few degrees or more, but not at shorter scales (Hautala et al., 1994; Roemmich and Wunsch, 1985). Short scale deviations from Sverdrup balance have been attributed to a breakdown in the assumption that the linear vorticity terms are small (Lu and Stammer, 2004). In the western boundary the ocean has been shown to deviate significantly from Sverdrup balance (Bryan et al., 1995). This is due to enhanced non-linear eddy activity close to the western boundary, and deep currents that ensure there is not a LONM. Polewards of the subtropics Sverdrup balance appears to break down entirely (Luyten et al., 1985; Bryan et al., 1995; Lu and Stammer, 2004). Most studies have focused on the Atlantic, but the findings are consistent for the Pacific (Hautala et al., 1994; Jiang et al., 2006) and Indian oceans (Godfrey and Golding, 1981).

Schmitz et al. (1992) formed a summary of the zonally integrated Sverdrup balance in the North Atlantic using the results from hydrographic surveys taken in the North Atlantic at 24°N (Leetmaa et al., 1977; Stommel et al., 1978; Roemmich and Wunsch, 1985) and from maps of the wind-derived Sverdrup transport streamfunction (Leetmaa and Bunker, 1978; Böning et al., 1991). They concluded that the zonally integrated upper interior North Atlantic along 24°N (east of the Antilles Current) is in Sverdrup balance, with southwards transports totalling 17 Sv. This is in balance with a 30 Sv northwards Florida Straits transport and a 13 Sv southwards deep transport. This conclusion was reached by combining the results of the aforementioned observational studies and in some cases modifying the results of those studies that included parts of the Antilles Current in their estimations (Schmitz et al., 1992). Any mis-representation of the western boundary edge (e.g. Leetmaa et al., 1977) can lead to large sensitivities in interior ocean transport estimations (Wunsch and Roemmich, 1985).

Care is required when interpreting observational evidence of Sverdrup balance due to assumptions made on the consistency between wind stress and ocean data. It has become apparent that the variety of available wind products can produce very different time-dependent (Landsteiner et al., 1990; Böning et al., 1991; Bryan et al., 1995; Townsend et al., 2000), and

time-mean (Josey et al., 2002; Aoki and Kutsuwada, 2008) wind stresses. Furthermore, most of the studies discussed present results that are either limited spatially or temporally.

A recent study (Wunsch, 2011) has suggested that large parts of the interior subtropical ocean are in Sverdrup balance when considered in a point by point manner in a 16 year time-mean of the ECCO-GODAE state estimation. This is possible due to the presence of a mid-depth level to integrate to at which the vertical velocities are small enough to be considered a LONM (see section 1.2.3). This is consistent with theoretical arguments for a wind-driven ocean, which suggest that on long enough time scales the deep flow from an initial barotropic response is eventually confined to the thermocline layer by the propagation of baroclinic Rossby Waves (Anderson and Killworth, 1977). Outside of the subtropics, where Rossby Wave phase speeds are slower than the background flow speed, this mechanism might be expected to break down since ocean changes happen faster than the ocean can adjust to them (Hughes and de Cuevas, 2001). In the case that the bottom flow is cut off then there can be no Bottom Pressure Torque (BPT; equation 9), which occurs when horizontal flow interacts with topography to produce vertical velocities. The squashing and stretching of the water column associated with these vertical velocities can lead to meridional flows at mid-depths in an analogous manner to Ekman pumping and suction in the upper ocean (see section 1.2.1). However, according to numerical models (Bryan et al., 1995; Hughes and de Cuevas, 2001), mooring data (Bryden, 1980) and scaling analysis (Wunsch and Roemmich, 1985), the BPT might still be large even in localised regions of the deep interior subtropics. This, however, is not likely to be related to wind forcing but rather to thermohaline driven deep currents that interact with topography. Depth ranges that are controlled by Ekman pumping and BPT will hereon be referred to as upper and lower layers respectively.

The aim of this study is to provide a full dynamical description of the processes involved in setting up Sverdrup balance and assessing over what time and spatial scales Sverdrup balance holds. The focus here is on the interior subtropical ocean away from the western boundary where Sverdrup balance is already known to break down. The ECCO-GODAE version 3 state estimate is used, which constrains the model solution to observational data

by use of its adjoint method (Marotzke et al., 1999). The ECCO-GODAE version 3 state estimate is the ideal framework within which to undertake such an investigation because it combines both observational and model attributes within a dynamically consistent environment. ECCO-GODAE gives a comparable estimate of the Atlantic overturning variability to that depicted by the RAPID array (Baehr et al., 2009).

In the following section the background theory is described. In section 2.3 the model is described, followed by an explanation of the methodology in section 2.4. Section 2.5 assesses the ability of Sverdrup balance to describe the subtropical circulation of the ocean. Section 2.6 then addresses whether the presence of deep ocean transports affect the assumption of a LONM. Section 2.7 addresses the question of how long it takes for the ocean to reach steady state, and finally section 2.8 summarises the main results and provides a discussion of their robustness and relevance to the real ocean.

2.2 Theoretical Discussion

The vorticity budget of the ocean is described by the curl of the steady state momentum equations (equations 2 and 3), which is written

$$\beta v = f \partial_z w + \hat{\mathbf{k}} \cdot \nabla \times \left(\partial_z \boldsymbol{\tau} + \nabla \cdot (A_h \nabla \mathbf{u}) - (\mathbf{u} \cdot \nabla) \mathbf{u} \right), \quad (10)$$

where f is the Coriolis parameter, $\beta = \partial_y f$, \mathbf{u} is the velocity vector of which u , v and w are the zonal, meridional and vertical components respectively, $\boldsymbol{\tau} = A_v \partial_z \mathbf{u}$ is the viscous stress and A_h and A_v are the horizontal and vertical viscosity coefficients respectively. The first two terms comprise the linear vorticity balance, the last two terms are the curl of the horizontal eddy viscosity and nonlinear advection respectively. The terms within the large brackets appear in this form in the momentum equation.

Integrating equation (10) from the surface, s , to some mid-depth level, h , and re-arranging for V , the depth integrated meridional velocity, we find that

$$\begin{aligned}
 V = & \frac{1}{\rho_0\beta} \hat{\mathbf{k}} \cdot \nabla \times \boldsymbol{\tau}_s - \frac{f}{\beta} w_h - \frac{1}{\beta} \left(\hat{\mathbf{k}} \cdot \nabla \times \boldsymbol{\tau}_h + \right. \\
 & \hat{\mathbf{k}} \cdot \nabla \times \int_{-h}^s \nabla \cdot (A_h \nabla \mathbf{u}) \, dz - \\
 & \left. \hat{\mathbf{k}} \cdot \nabla \times \int_{-h}^s (\mathbf{u} \cdot \nabla) \mathbf{u} \, dz \right). \tag{11}
 \end{aligned}$$

It has been assumed that there is no vertical flow through the surface. The first two terms comprise Sverdrup balance, which would hold if all other terms are negligible. This states that any time-mean meridional mass flux above a LONM is solely a consequence of a non-zero wind-stress curl. A physical description is that the effect of squashing and stretching (vortex stretching) caused by Ekman pumping is compensated by a change in latitude in order to conserve potential vorticity. The second term on the RHS is here called the LONM error, Δ_{LONM} . The remaining terms on the RHS, the curl of the horizontal viscosity term, $\hat{\mathbf{k}} \cdot \nabla \times HV$, and nonlinear advection term, $\hat{\mathbf{k}} \cdot \nabla \times ADV$, are together called the linear vorticity error, Δ_{LV} (the depth-integrated form of the depth-dependent linear vorticity error, δ_{LV} , which is the sum of the last two terms on the RHS of equation 10). The two error components combined is called the Sverdrup error, Δ_{SB} . Hereafter, the LHS of equation (11) is referred to as the ocean transport and the first term on the RHS as the Sverdrup transport. The definition of Sverdrup balance used here is a description of the time-mean and not time-dependent meridional flow. The extent of time averaging required for the ocean to reach a time-mean state will be assessed in section 2.7.

2.3 Model Description

In this study the global state estimation product, ECCO-GODAE, is used, which incorporates ocean observations into the solution of the Massachusetts Institute of Technology general circulation model (MITgcm; Marshall et al., 1997). The version 3 product is used which, unlike the previous version, features a full sea ice model and the use of atmospheric bulk formulae

to calculate wind stress. Ocean observations employed in the model solution include satellite based sea surface height, temperature, wind stress and geoid products, as well as in-situ collected observations (from ARGO floats and hydrographic sections) of salinity and temperature. See Wunsch and Heimbach (2007) for a more complete description of the data included and methods of incorporation.

The model solves the primitive equations using the Boussinesq approximation. The horizontal resolution is 1° in longitude and latitude (between 80°S and 80°N) and there are 23 levels in the vertical. Output is given in monthly intervals from January 1992 to December 2007 (although year 1992 is removed to avoid any residual model spin up). Horizontal viscosity is parameterised as a Laplacian and solved explicitly with a coefficient of $10^4 \text{ m}^2\text{s}^{-1}$. Vertical viscosity is solved implicitly according to the KPP parameterisation of Large et al. (1994) with background viscosity coefficient set at $10^{-3} \text{ m}^2\text{s}^{-1}$. Bottom and Lateral boundaries are non-slip and free-slip respectively.

The consortium for Estimating the Circulation and Climate of the Oceans (ECCO) was set up to synthesize datasets produced as a result of the World Ocean Circulation Experiment (WOCE). It provides four dimensional estimates of oceanic variables which would otherwise be difficult to produce from observations alone. The model solution is optimised by use of its model adjoint (Marotzke et al., 1999), which reduces the model-to-data misfit by a gradient descent approach using multiple iterations to minimise a cost function. The advantage over an observations-only dataset is that the model outputs onto a complete and regular grid, effectively filling in the gaps between observations. The adjoint methodology additionally leads to terms in the momentum and vorticity equations that are dynamically consistent with each other leaving no residual.

2.4 Methodology

2.4.1 Calculation of Vorticity in ECCO

ECCO-GODAE solves the discretised momentum equation on an Arakawa C grid (Arakawa and Lamb, 1977, see Appendix B for a description of the velocity locations on the C grid) according to the method described

in the MITgcm online manual found at the website, http://mitgcm.org/sealion/online_documents/node2.html. ECCO-GODAE also employs the so-called CD scheme (Adcroft et al., 1999) to calculate the Coriolis term, which uses velocities located in the D grid configuration.

The time average is taken over the period 1993-2007 and assumed to be representative of the time mean state. All vorticity terms are calculated so that they are located on the vorticity point of the C grid. The last three terms of equation (10) are calculated as the finite difference curl of the equivalent terms in the momentum equation. The LHS of equation (10) is calculated as the zonal average of the neighbouring D grid meridional velocities multiplied by β . The averaging locates the term onto the vorticity point of the grid. The first term on the RHS of equation (10) is calculated as the (negative of the) horizontal divergence of the D grid velocities multiplied by f (see Appendix B for a discussion of the importance of correctly considering the grid when making calculations of vorticity). Any plots that present terms in equation (11) are given as depth-integrated transports with units m^2s^{-1} .

2.4.2 Defining the Study Domain

In light of the break down of Sverdrup balance at western boundaries and at high latitudes, a mask is defined to exclude regions between the western boundary and 1000 km east of the 2000 m depth contour. Anything poleward of 35° latitude is also masked. These limits are chosen qualitatively based on the data. The results presented throughout this study are largely insensitive to small changes of approximately 200 km in the size of the mask at the boundaries. Regions lying within the masked regions will be excluded in any calculations of integrated or averaged quantities. Regions outside of the mask are considered to be the ocean interior. The mask is displayed as white in maps of transport.

2.4.3 Sverdrup Balance Metrics

Two metrics are defined to characterise how well Sverdrup balance holds, one that concerns the pointwise field and the other the zonally integrated field. Both definitions of Sverdrup balance are of interest since each one

provides us with a different understanding of the system. The zonally integrated metric is the more important in considerations of how Sverdrup balance would affect e.g. basin-wide mass balance and the pointwise metric is more important in considerations of how Sverdrup balance would affect e.g. the heat transport.

Of interest is the magnitude of the Sverdrup error relative to the magnitude of the Sverdrup transport. Therefore the pointwise metric, M_{pw} , is defined as the horizontal-mean of the absolute pointwise Sverdrup error divided by the horizontal-mean absolute pointwise Sverdrup transport. Likewise, the zonally integrated metric, M_{zi} , is the meridional-mean absolute zonally integrated Sverdrup error divided by the meridional-mean absolute zonally integrated Sverdrup transport, or

$$M_{pw} = \frac{\langle |\Delta_{SB}| \rangle}{\langle |\frac{\hat{\mathbf{k}} \cdot \nabla \times \tau}{\rho_0 \beta}| \rangle}, \quad (12)$$

$$M_{zi} = \frac{\langle |\int_{x_{west}}^{x_{east}} \Delta_{SB} dx| \rangle}{\langle |\int_{x_{west}}^{x_{east}} \frac{\hat{\mathbf{k}} \cdot \nabla \times \tau}{\rho_0 \beta} dx| \rangle}, \quad (13)$$

where the angle brackets represent horizontal and meridional domain averages in equation (12) and (13) respectively. First taking a horizontal average removes the problem of dividing by localised regions of zero (or small) Sverdrup transport. As such, the metrics are quite strongly domain dependent and best used over a large domain. Both metrics are applied to all interior ocean unmasked regions. Values are expressed as percentages, where 0% implies a perfect balance and 100% implies the errors are as large as the Sverdrup transport. To assess and compare Sverdrup balance over different spatial scales, 2D boxcar smoothing functions of different sizes (as stated in the relevant sections) are applied to the transport fields prior to the application of each metric.

The metrics here are sensitive to a small number of grid cells with anomalously large transport values that remain after application of the mask. These grid points are all located at the poleward and western boundaries of the mask, around islands or in eastern boundary currents, and act to bias the metrics in favour of an imbalance in Sverdrup balance. They are mostly due to strong values of Δ_{LONM} . For this reason the 99th percentile of the Sverdrup error field is first removed in any calculation of Sverdrup balance

to ensure that significant outliers are not considered.

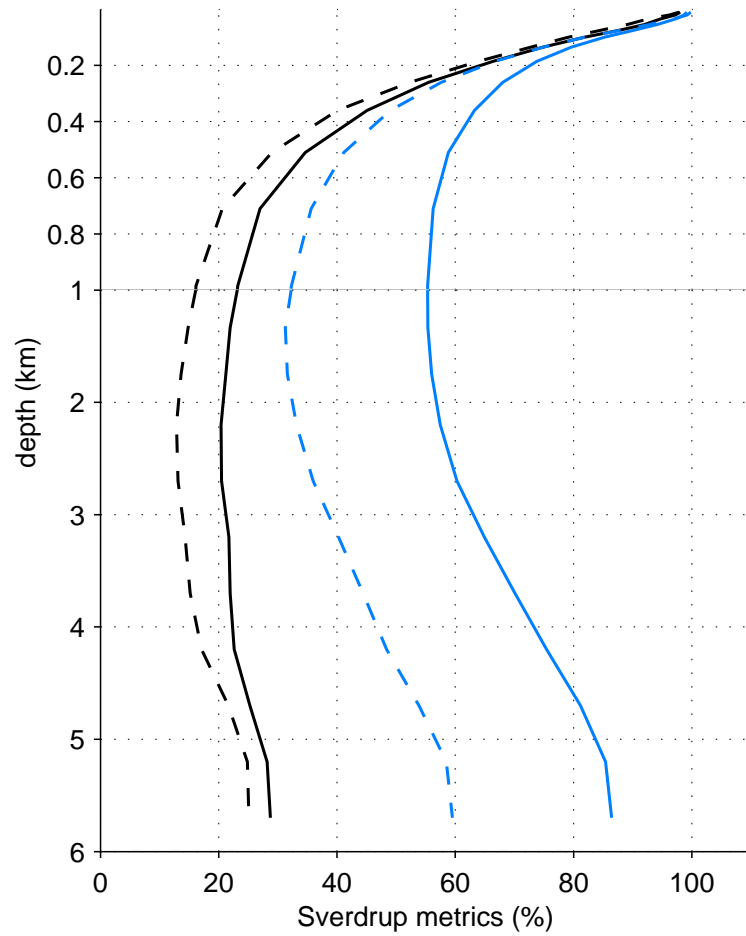


Figure 2.1: M_{pw} (blue) and M_{zi} (black) versus integration depth. The metrics are applied to unmasked regions between 35°S and 35°N . Solid lines represent unsmoothed values and dashed lines represent 2D smoothing of the transport fields over 5° . Note the change in y-axis scale at 1 km depth.

2.5 Validity of Sverdrup Balance

Figure 2.1 shows how the Sverdrup balance metrics, M_{pw} (blue line; equation 12) and M_{zi} (black line; equation 13) change with the choice of integration depth (i.e. the depth to which the ocean transport is integrated from the surface down) when applied over the masked subtropical domain. The first metric describes the percentage to which Sverdrup balance holds on a pointwise basis and the second describes how it holds on a zonally in-

tegrated basis. Both metrics initially reduce with integration depth before increasing again after the optimal depths of 985 m and 2200 m are reached for M_{pw} and M_{zi} respectively. The initial reduction corresponds to an increasing amount of wind-driven flow being included in the depth-integral. The later increase corresponds to an increasing amount of non-wind-driven flow being included in the integral.

Sverdrup balance holds poorly in the subtropics when evaluated point-wise (per unsmoothed grid cell). The optimum value of M_{pw} is 56% (i.e. the Sverdrup error is 56% of the magnitude of the Sverdrup transport). Application of 2D smoothing to the transport fields greatly reduces M_{pw} to 31% at scales of 5° and pushes the minimum to a deeper level. The reason for this is that small scale variability present in the wind stress curl is smoothed out by averaging. Further increasing the smoothing scale continues to reduce M_{pw} up until scales of about 9° , at which it is 21%. Beyond this scale, smoothing makes little difference. Sverdrup balance therefore holds to a good order of approximation at scales of approximately 5° or more, but not at scales shorter than this (see section 1.2.1 for a brief discussion of what is considered to be a good order of magnitude). The findings support earlier studies based on hydrographic measurements (Hautala et al., 1994; Roemmich and Wunsch, 1985).

The optimum zonally integrated unsmoothed metric, M_{zi} , is 20% for an integration depth of 2200 m. The reduced size of M_{zi} compared to M_{pw} is because the zonal integration removes some zonal spatial variability. For this reason, the 2D smoothing (applied prior to integrating) only significantly affects the transport fields in the meridional direction, reducing the unsmoothed value of M_{zi} to 13% at 5° smoothing. As with M_{pw} , smoothing stops being effective after approximately 9° when M_{zi} becomes 10%. The zonally integrated subtropical ocean is therefore in a good order of Sverdrup balance, even when unsmoothed.

The use of a depth plane as an integration depth is a relatively simple approach to calculate Sverdrup balance, which might be expected to hold over different layer thicknesses in different regions. An investigation has been made into finding a more complicated LONM that changes geographically according to the local velocity characteristics. The results of this investigation are described in Appendix A. The main conclusion from

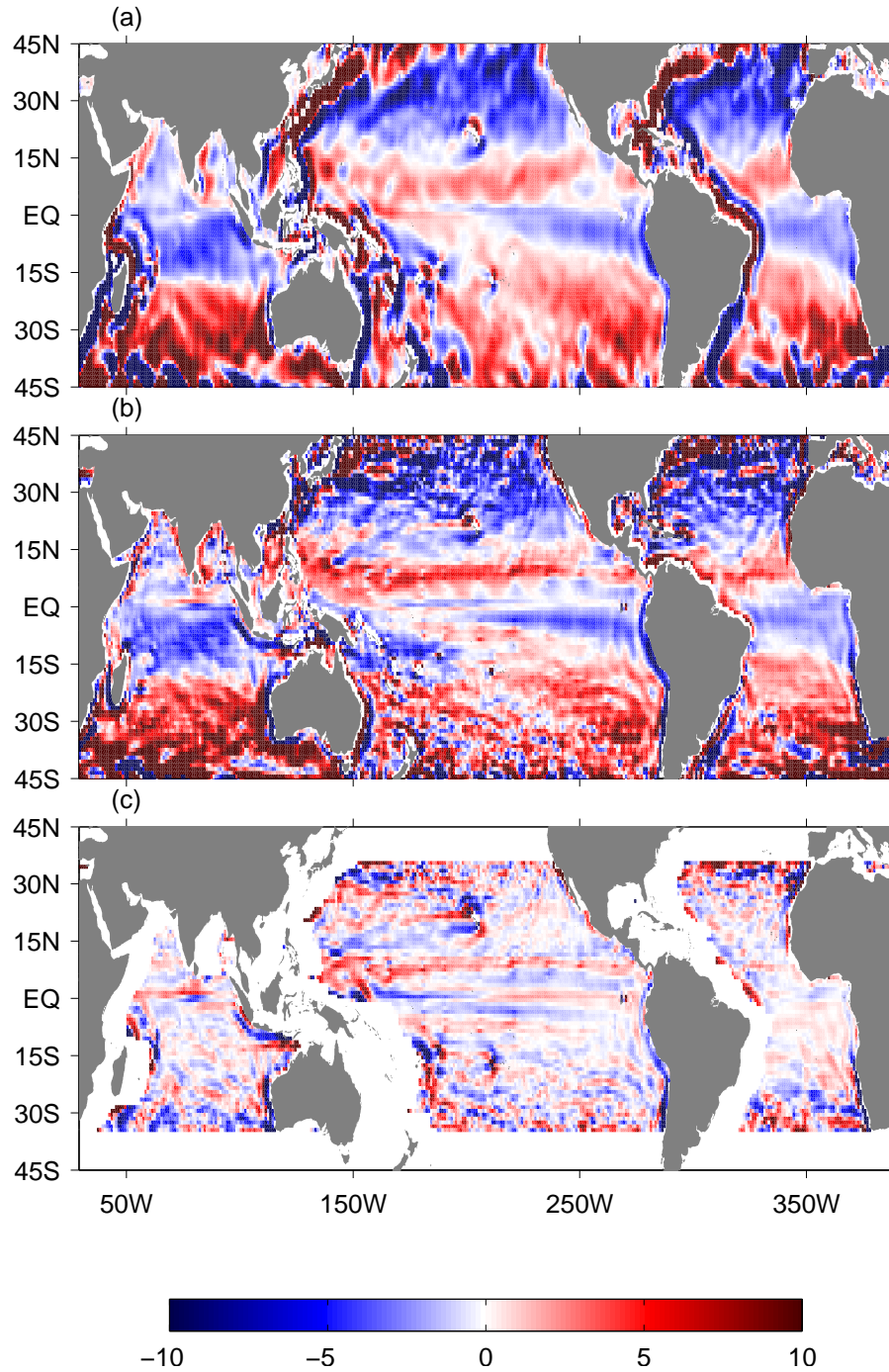


Figure 2.2: The terms in the 15 year time averaged Sverdrup balance. (a) V (using an integration depth of 2200 m), (b) $\frac{1}{\rho_0\beta} \hat{\mathbf{k}} \cdot \nabla \times \boldsymbol{\tau}_s$ and (c) the Sverdrup error, $\frac{1}{\rho_0\beta} \hat{\mathbf{k}} \cdot \nabla \times \boldsymbol{\tau}_s - V$. The white border in (c) indicates masked regions that are not included in the determination of any integrated quantities. Units are m^2s^{-1} .

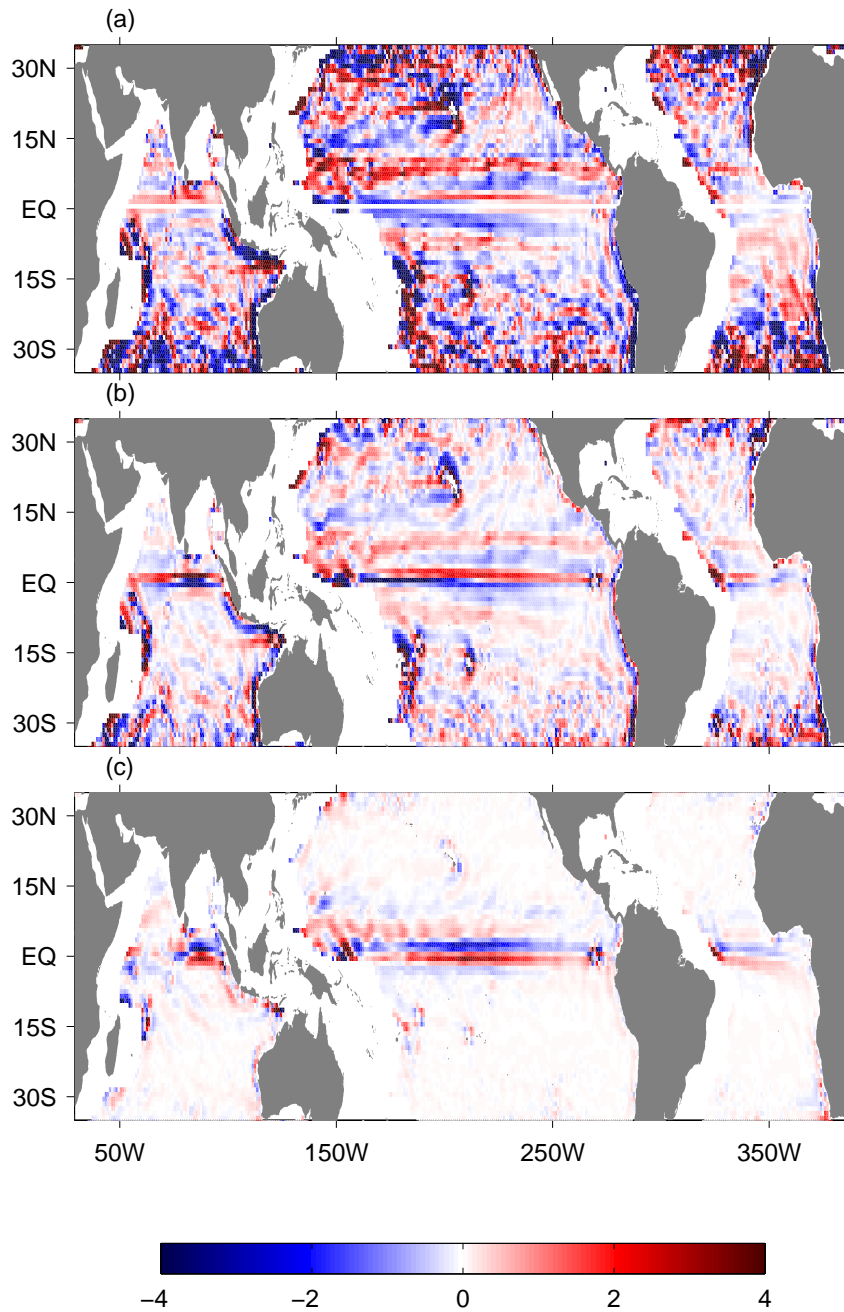


Figure 2.3: Component errors of the Sverdrup error, Δ_{SB} , (a) LONM error, $\Delta_{LONM} (fw_h/\beta)$, (b) $\hat{\mathbf{k}} \cdot \nabla \times \text{HV}$ and (c) $\hat{\mathbf{k}} \cdot \nabla \times \text{ADV}$. The linear vorticity error, Δ_{LV} is the sum of (b) and (c). Depth integrations are made to 2200 m. Units are m^2s^{-1} .

the analysis is that it is relatively unimportant which depth is integrated to, so long as it is locally deeper than the main body of the thermocline and not so deep as to include the deep transports. The results from using a geovarying LONM therefore do not greatly differ from the use of a plane at 2200 m. All analysis of Sverdrup balance throughout the rest of the chapter uses an integration depth plane at 2200 m depth.

Figure 2.2 shows the 15 year time-mean ocean transport (V) depth-integrated to 2200 m, the Sverdrup transport ($\frac{1}{\rho_0\beta} \hat{\mathbf{k}} \cdot \nabla \times \boldsymbol{\tau}_s$) and the Sverdrup error ($\frac{1}{\rho_0\beta} \hat{\mathbf{k}} \cdot \nabla \times \boldsymbol{\tau}_s - V$). Both transport fields exhibit similar large scale structure, such as equatorward subtropical mass transport, and polewards near-equatorial transport. These are formed respectively by the downwards Ekman pumping induced by the anticyclonic wind stress forcing and by the trade winds. Consistent with theory (Pedlosky, 1987) and modelling studies, Sverdrup balance does not hold in the model at western boundaries (Bryan et al., 1995) and at high latitudes (Bryan et al., 1995; Gent et al., 2001). These regions are mostly excluded by the mask shown in Figure 2.2(c). Some small regions with large Sverdrup error remain in the interior ocean due to boundary related processes that are uncaptured by the mask near its edge.

As discussed in section 2.1, the Sverdrup error (Figure 2.2c) can be decomposed into two component errors, the LONM error, Δ_{LONM} (Figure 2.3a) and the linear vorticity error, Δ_{LV} . The linear vorticity error can be further split into two component parts, the horizontal viscosity term, $\hat{\mathbf{k}} \cdot \nabla \times HV$ (Figure 2.3b), and the advection term, $\hat{\mathbf{k}} \cdot \nabla \times ADV$ (Figure 2.3c). The advection component makes small contributions in the western boundary currents, in near equatorial regions and at high latitudes, but can generally be considered negligible everywhere in the subtropical gyre. The horizontal viscosity term can therefore be considered the sole contributor to the linear vorticity error throughout the subtropics in this state estimate.

The two error components, Δ_{LV} and Δ_{LONM} , each increase in magnitude at higher latitudes and tend to have the same polarity so that they constructively contribute to the Sverdrup error in the subtropical interior ocean. The dominant term in the Sverdrup error is Δ_{LONM} which is on average approximately twice as large as Δ_{LV} in the domain shown. Zonal sections and zonal integrals of both Δ_{LV} (red line) and Δ_{LONM} (cyan line)

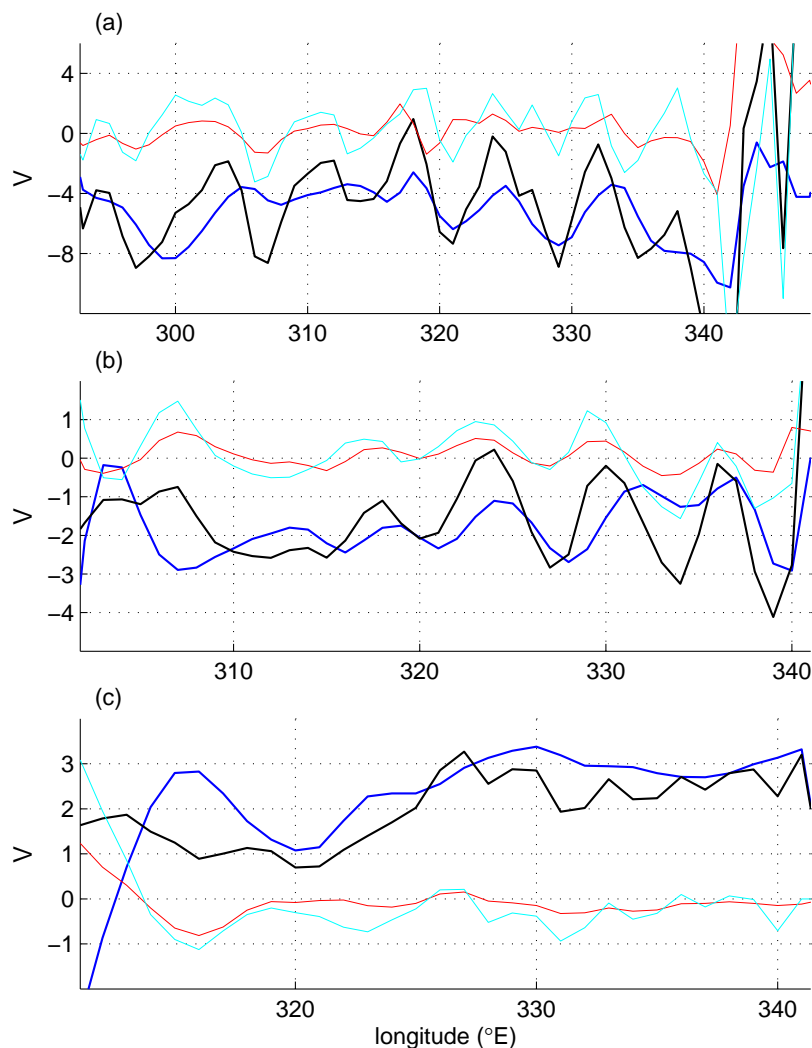


Figure 2.4: Atlantic zonal sections of the terms in Sverdrup balance: V (using an integration depth of 2200 m; thick blue line) and $\frac{1}{\rho_0\beta} \hat{\mathbf{k}} \cdot \nabla \times \boldsymbol{\tau}_s$ (thick black line) at (a) 30°N, (b) 20°N and (c) 10°N. Thin lines represent the linear vorticity error (thin red line) and LONM error (thin cyan line). See text for how these are derived. Units are m^2s^{-1} .

are shown in Figure 2.4 and Figure 2.5 respectively. The spatial patterns of Δ_{LONM} and Δ_{LV} are very similar with the approximate 2:1 ratio mentioned above holding in most places. The in-phase variability of the two error terms may be due to the requirement to conserve potential vorticity (equation 8). Considering an idealised scenario on an f -plane (where $PV = \zeta/H_i$; see equation 8), in which a wind-driven layer of depth H_i lies above a LONM, the sudden presence of any nonlinearity in the vorticity equation will contribute to ζ and will accordingly be compensated by a change in H_i that modifies the depth of the LONM. A change in the depth

of the LONM will mean the vertical profile of vertical velocities must also change. If some arbitrary level above the LONM were used as the integration depth in Sverdrup balance, then the vertical velocities and therefore Δ_{LONM} would be different before and after the appearance of the nonlinear vorticity term. Whether correlations between Δ_{LV} and Δ_{LONM} would be positive or negative would likely depend upon both the depth of integration used and the pre-existing vertical profile of vertical velocities. This is suggested for further work.

Values of Δ_{LV} and Δ_{LONM} presented here differ from those presented in Lu and Stammer (2004), who use an earlier version of the ECCO-GODAE model. Lu and Stammer (2004) attribute most of the error in the interior subtropics within 35° of the Equator to the linear vorticity error, comprised mostly of $\hat{\mathbf{k}} \cdot \nabla \times \text{ADV}$, and suggest that Δ_{LONM} only becomes significant polewards of 20° latitude. This may be due to the different way the vorticity equation is calculated in Lu and Stammer (2004). The reader is referred to Appendix B for a discussion of how the vorticity equation is calculated in this study.

Sverdrup errors close to the eastern boundaries are in places large in all ocean basins other than the North Pacific and North Indian. Additional large Sverdrup errors occur at the island chains of Hawaii in the North Pacific and French Polynesia in the South Pacific. In each case large Sverdrup and model transports are arranged into dipole patterns around the island chains. However, the dipole patterns are not similarly oriented and so the pointwise Sverdrup errors (i.e. the difference between them) in this region are large. It is unclear exactly why these patterns are created, although the wind stress curl pattern may be caused by interaction between orography and the mean wind stress. The modified wind stress curl may then produce similar dipoles in the ocean that are subsequently distorted by bathymetry.

In our unmasked domain, the wind-derived Sverdrup transport contains small scale variability that is not present everywhere in the ocean transport (Figure 2.2c). This explains the large deviations from Sverdrup balance described by the pointwise Sverdrup metric. The small scale spatial variability of the Sverdrup transport is seen more clearly in Figure 2.4 which shows zonal sections of the ocean and Sverdrup transports in the North Atlantic at latitudes 10°N , 20°N and 30°N . Ocean and Sverdrup transports follow a

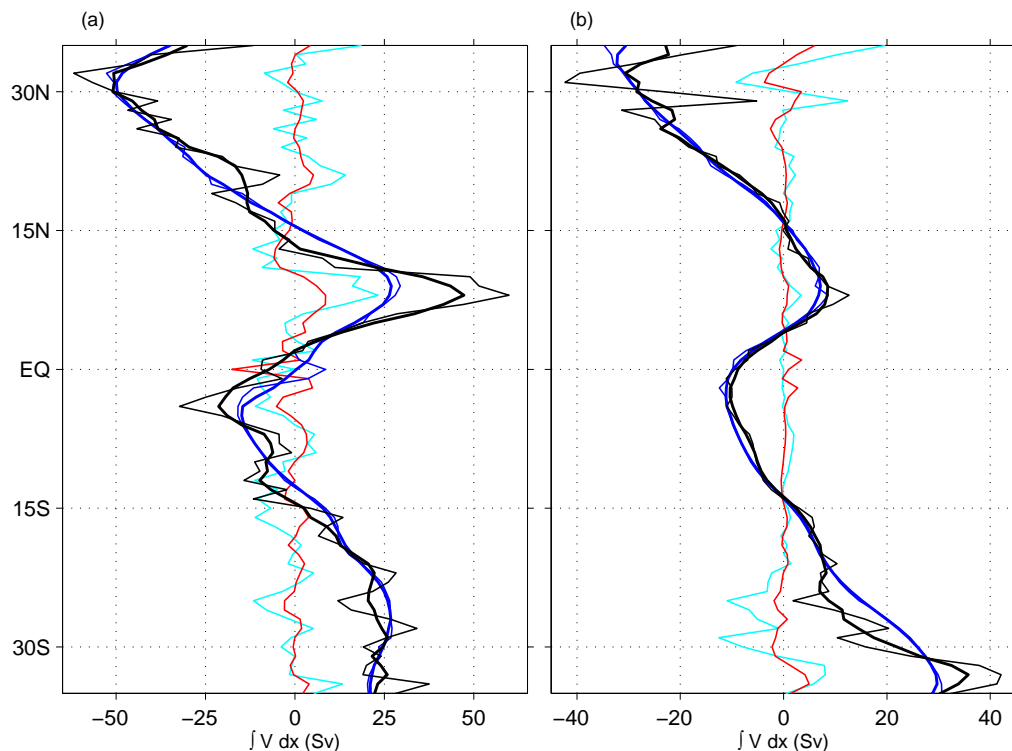


Figure 2.5: Zonally integrated values of the terms in Sverdrup balance: V (using an integration depth of 2200 m; thin blue line) and $\frac{1}{\rho_0 \beta} \hat{k} \cdot \nabla \times \tau_s$ (thin black line) versus latitude in the (a) Pacific and (b) Atlantic. The other thin lines represent the linear vorticity error, Δ_{LV} (red), and LONM error, Δ_{LONM} (cyan), respectively (see text for how these are derived). Thick lines represent 2D smoothing of the transport fields over 5° . Only values outside of the masked region shown in Figure 2.2(c) are used in the integrals. Units are Sv.

similar broad scale structure, but the Sverdrup transport exhibits greater variance at smaller zonal scales, particularly at the higher latitudes. This is consistent throughout all ocean basins. High variability in the Sverdrup transport is also present in the 5 year mean of Quikscat derived wind stress curl at 25 km resolution (Chelton et al., 2004). Despite the difference between Sverdrup and model transport on small scales, the zonal integrals of these transports in the Atlantic (Figure 2.5 right panel) and Pacific (Figure 2.5 left panel) are in good agreement, particularly if 5° meridional smoothing is applied (thick lines).

Large deviations remain in the smoothed curves of zonally integrated Sverdrup balance in the South Atlantic region south of approximately 30°S and at 8°N in the Pacific. The first of these is possibly related to the

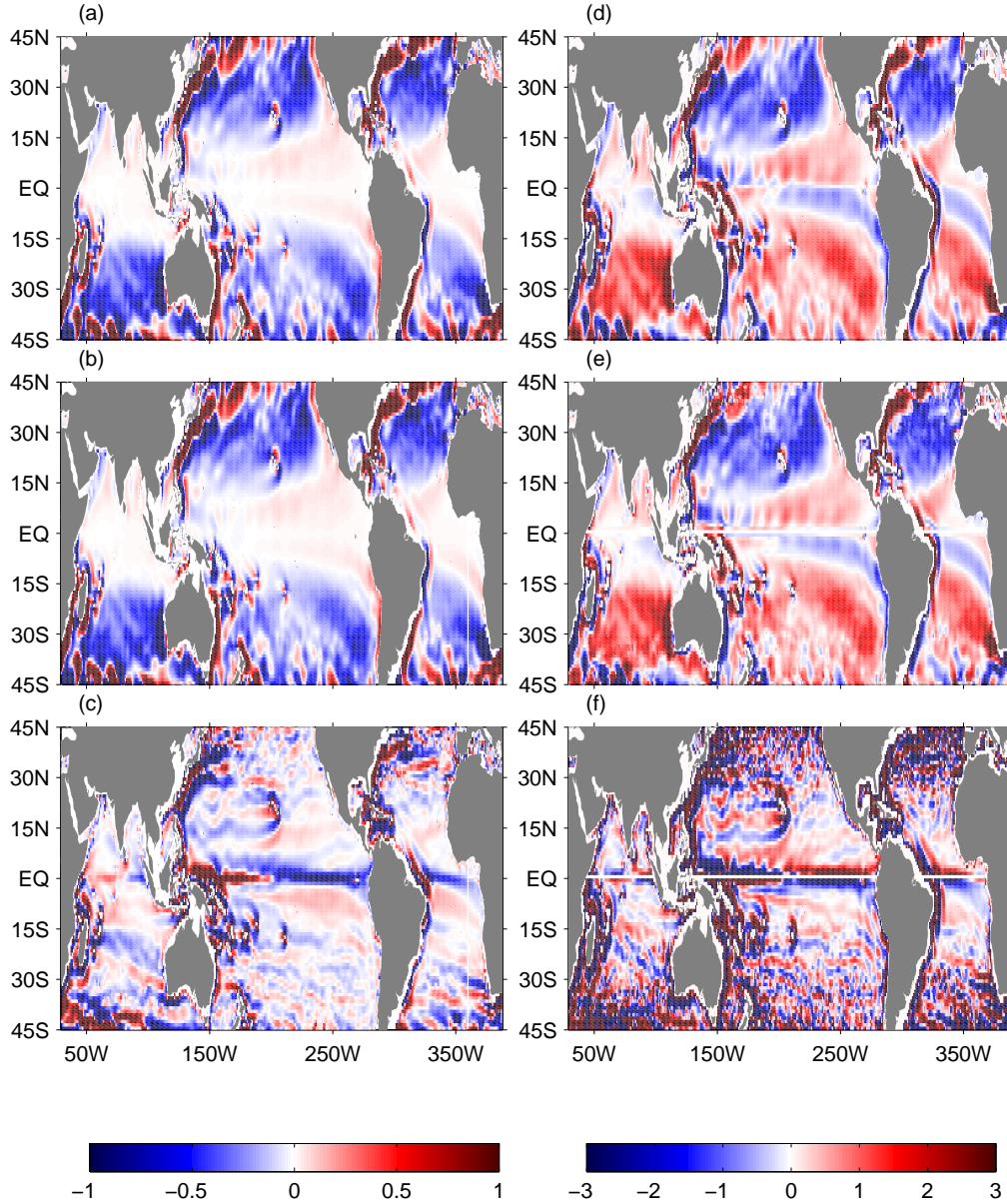


Figure 2.6: The terms in the 15 year time-averaged geostrophic equation at 310 m depth (a) fv , (b) $-\frac{1}{\rho_0}\partial_x p$ and (c) their difference. The terms in the 15 year time-averaged linear vorticity equation at 310 m depth (d) βv , (e) $f\partial_z w$ and (f) their difference. Units in (a-b) are 10^{-6} m s^{-2} and in (c) are 10^{-8} m s^{-2} . Units in (d-e) are 10^{-13} s^{-2} and in (f) are 10^{-14} s^{-2} .

Agulhas Current leakage into the South Atlantic. The second is associated with stronger Sverdrup transports in the trade wind belt. This may be related to the fact that a lot of the Sverdrup transport variability is structured into near-zonal bands. Such zonal banding may be produced by the model adjoint (Lu and Stammer, 2004), which modifies the wind observations (within their rather large uncertainties) to fit consistently with the other constraining datasets and the model physics. Problems in one of the other constraining datasets or in the model physics (e.g. exaggerated viscosity) may therefore be the source of the banding.

In ECCO-GODAE the momentum balance is more geostrophic (equation 4) than the vorticity balance is linear (equation 10). This is despite linear vorticity being derived as the curl of geostrophy. To demonstrate this, Figure 2.6 shows, at a depth of 310 m, 15 year time-means of the zonal geostrophic terms (a) fv , (b) $-\frac{1}{\rho_0}\partial_x p$ and (c) their difference ($fv + \frac{1}{\rho_0}\partial_x p$), and of the linear vorticity terms (d) βv , (e) $f\partial_z w$ and (f) their difference ($\beta v - f\partial_z w$). While the residual of the geostrophic terms (the sum of the ageostrophic terms) is two orders of magnitude smaller than either of the geostrophic terms, the linear vorticity error is only one order of magnitude smaller than the linear vorticity terms at this depth. The implication is that the ageostrophic terms become of greater importance only when the curl is taken.

2.6 Deep Ocean Processes

Past studies have suggested that BPT can be large in the subtropical ocean. This section addresses the magnitude of BPT in the deep ocean and the impact of BPT and topography on Sverdrup balance. Considerable depth integrated transports exist in the model below 2200 m depth (Figure 2.7a) that are in places comparable in magnitude to the upper ocean transports (Figure 2.2a). In the interior ocean, the (pointwise domain-integrated) magnitude of the depth-integrated transports below 2200 m is 55% of the size of the equivalent in the upper 2200 m. Deep transports in ECCO-GODAE are largely induced by BPT (equation 9) as shown in Figure 2.7(b) (by BPT divided β). The BPT compares well to that from an eddy permitting ocean model (Hughes and de Cuevas, 2001, c.f. Figure 1.10), and supports

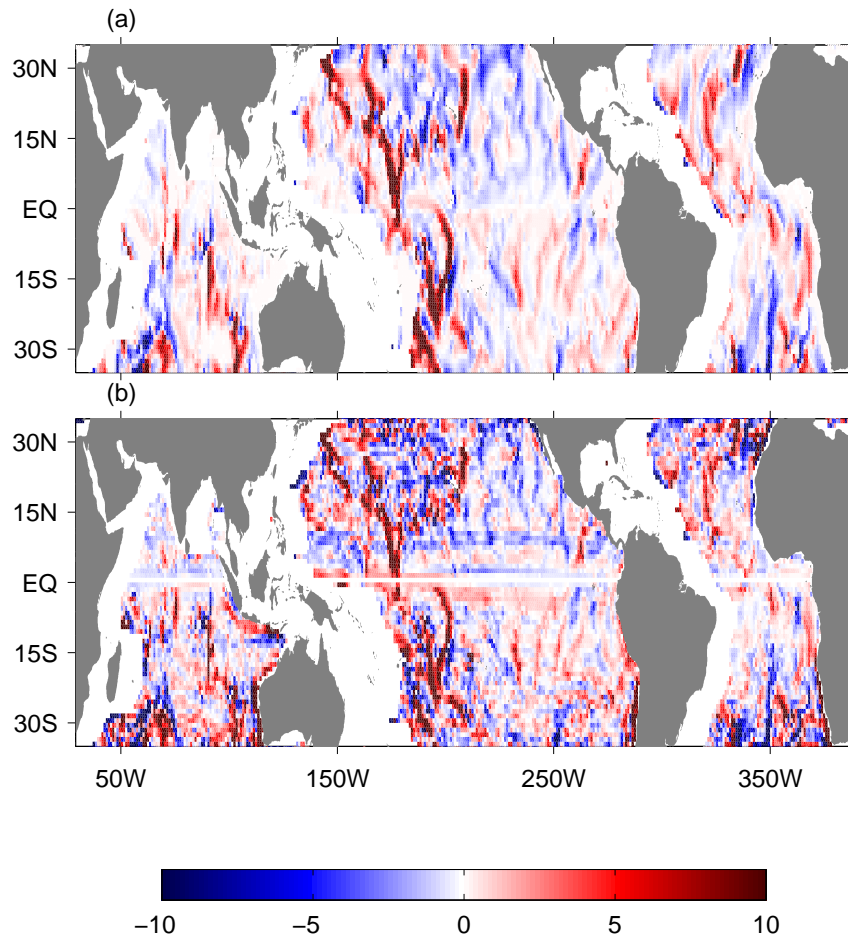


Figure 2.7: (a) Meridional transport depth integrated from 2200 m depth to the bottom (b) BPT expressed as a transport (fw_b/β). Units are in m^2s^{-1} .

past estimates of BPT in the deep subtropical ocean (Bryan et al., 1995; Hughes and de Cuevas, 2001). If equation (11) was obtained by integrating to the ocean floor, then the bottom vertical velocities (w_b) would cause large Sverdrup errors even in the subtropical interior ocean (Figure 2.1).

The deep velocities in Figure 2.7(a), however, do not resemble either of the upper layer 2200 m depth integrated LONM error or LV error shown in Figure 2.3. This suggests that the Sverdrup errors in the 2200 m depth-integrated Sverdrup balance arise from wind driven processes and not BPT driven processes. The Δ_{LONM} shown in Figure 2.3 is therefore the result of Ekman pumped vertical velocities that are driven by small scale fluctuations in the time mean wind stress curl. These vertical velocities do not diminish enough with depth before deep BPT induced vertical velocities are encoun-

tered, which is why there is not a LONM to integrate to when considered on a pointwise basis (Figure 2.1). Although BPT does have a significant impact on the vorticity equation in the deep ocean, as will be discussed in the following paragraphs, the results indicate that BPT is not important to the circulation of the upper 2200 m of the ocean when considered at scales greater than approximately 5° . Note that flow directions are not perpendicular to bathymetry contours but are instead rather more parallel (not shown). According to the kinematic boundary condition, $w_b = \mathbf{u} \cdot \nabla H$, where H is the full depth of the ocean, the BPT would be significantly higher if the flow were less parallel to bathymetry contours.

To assess the depth to which the BPT affects Sverdrup balance, linear vorticity balance is composited into two sets: 1) all interior ocean grid cells that are located above or immediately adjacent to sloping topography, 2) all grid cells located above flat topography. Only unmasked regions are considered. For each set, the modulus of the terms of the linear vorticity relation, $|\beta v|$ and $|f\partial_z w|$, are calculated at each depth level and horizontally averaged. The modulus is first taken before averaging in order to avoid cancellation of positive and negative values. The absolute linear vorticity error, $|\delta_{LV}| = |\beta v - f\partial_z w|$, is also calculated which tells us the magnitude of the pointwise linear vorticity error for each set at each depth. (Note that the vertical integral of horizontal-mean absolute values does not necessarily equal the horizontal-mean absolute value of a vertical integral. Vertical integrals of $|\beta v|$ and $|f\partial_z w|$ cannot therefore be compared to any values presented earlier.)

Lower layer values of $\langle |\beta v| \rangle$ (black curves) and $\langle |f\partial_z w| \rangle$ (blue curves) (where angle brackets denote horizontal averaging) are higher in regions above sloping topography (Figure 2.8), which is suggested here to be due to the effects of BPT. The domain averaged effects of BPT reach only so far as approximately 1500 m, above which the profiles of the two terms calculated above sloping and flat topography are then mostly forced by the wind and so follow similar curves up to the surface. Although the BPT induced deep transports are large, when considered over large scales the deep transports are effectively isolated from the upper ocean by a mid-depth LONM.

The linear vorticity balance, $\langle |\delta_{LV}| \rangle$, is shown to be worse throughout the water column in regions above sloping topography (red curves; Figure

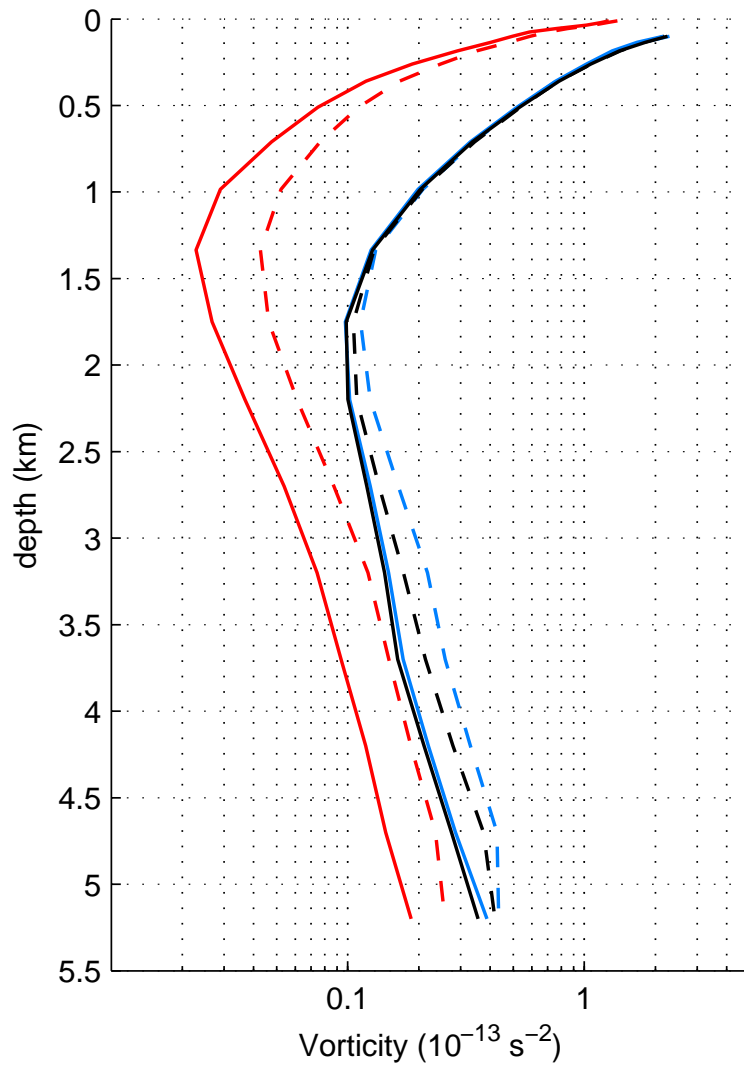


Figure 2.8: Mean values of the composite sets of $|\beta v|$ (black) and $|f\partial_z w|$ (blue) for grid cells above or adjacent to sloping topography (dashed) and flat topography (solid). The mean depth-dependent linear vorticity error, $|\delta_{LV}|$, is shown in red for each composite set.

2.8). It should be noted, however, that continental slopes will affect the upper water column of the sloping topography composite set, so the higher average pointwise linear vorticity error in the upper ocean does not necessarily indicate that BPT in the abyssal ocean impacts the upper ocean linear vorticity balance. Although linear vorticity error is larger over topographic slopes, this is not because of higher BPT (since bottom vortex stretching induces meridional currents through the linear vorticity terms themselves) but instead because of increased $\hat{\mathbf{k}} \cdot \nabla \times \mathbf{H}V$ near topography (not shown). This is perhaps due to frictional drag.

Linear vorticity balance holds very well in the subtropics on large scales, particularly in the upper 1.5 km (Figure 2.8). A large scale consideration of linear vorticity balance, calculated as $(\langle |\beta v| \rangle - \langle |f \partial_z w| \rangle) / \langle |f \partial_z w| \rangle$, is typically 5% in the upper ocean (below the Ekman layer), and 5% and 20% in the deep ocean above sloping and flat topography respectively. A pointwise consideration of linear vorticity balance, calculated as $\langle |\beta v - f \partial_z w| \rangle / \langle |f \partial_z w| \rangle$, is worse, indicating that small scale linear vorticity errors average out over large scales. Pointwise linear vorticity balance errors are typically 19% and 24% of $\langle |f \partial_z w| \rangle$ respectively above flat and sloping topography in the top 1335 m. In the lower layer below 1335 m this worsens, where the pointwise linear vorticity errors reach up to approximately 55% and 70% of $\langle |f \partial_z w| \rangle$ over flat and sloped regions respectively. Thus, while pointwise linear vorticity balance in the upper layer holds to a good order of approximation, it breaks down entirely in the deep ocean because of $\hat{\mathbf{k}} \cdot \nabla \times \mathbf{H}V$ near topography.

2.7 Steady State Averaging Time

Here it is investigated what adjustment time scale is required for the ocean to reach equilibrium i.e. the time averaging required before the time-dependent terms in the vorticity equation become negligible. When enough time averaging is applied such that the ocean is no longer adjusting then the system will have reached the best possible Sverdrup balance that it can achieve. The equilibrium time scale is determined by first calculating the 15 year time series of the zonally integrated Sverdrup error (Δ_{SB} ; see section 2.2) at each latitude, from 2200 m depth-integrated Sverdrup balance, and cumulatively averaging it in steps from 1 month to 15 years. A five month running standard deviation is then applied at each latitude giving what is called the Sverdrup error fluctuation (Figure 2.9). A high Sverdrup error fluctuation means that the ocean has not yet reached equilibrium. There is a clear latitude dependence on the amount of time taken to reach equilibrium, increasing polewards from the Equator.

The ocean is theorised to adjust to wind forcing by the propagation of Rossby Waves (Anderson and Killworth, 1977), whose phase speed decreases away from the Equator. The black line in Figure 2.9 represents the

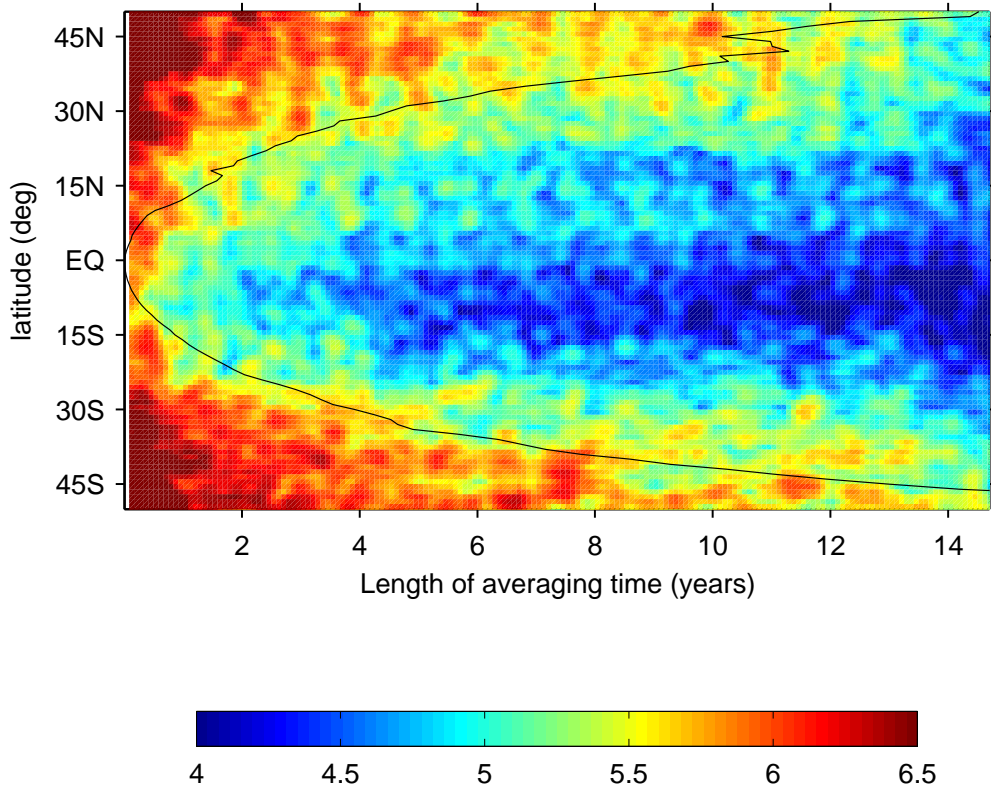


Figure 2.9: The Sverdrup error fluctuation (i.e. the running standard deviation of the zonally integrated Sverdrup error from 2200 m depth-integrated Sverdrup balance; see text) at every latitude of the subtropical Atlantic for averaging time periods of up to 15 years. The black line is the basin crossing time of a Rossby Wave propagating at the non-dispersive limit according to the bottom pressure compensation theory of Tailleux and McWilliams (2001). The resulting field has been 2D smoothed over 3° latitude and 3 months. Units are $\log_{10}(\text{m}^3 \text{s}^{-1})$.

basin crossing time for a theoretical Atlantic Rossby Wave propagating at the non-dispersive phase speed, according to the bottom pressure compensation theory of Tailleux and McWilliams (2001). The Rossby wave theory accounts for modifications to the vertical baroclinic modes made by bottom topography (data provided courtesy of Dudley Chelton), and predicts faster Rossby Waves than those predicted by the standard linear theory (Gill, 1982). An excellent fit is found between the basin crossing time for a Rossby Wave and the equilibrium time scale.

To demonstrate the extent that Sverdrup balance holds on these averaging time scales, Figure 2.10 shows M_{zi} (equation 13) calculated at each latitude and time-averaging extent (the numerator and denominator are

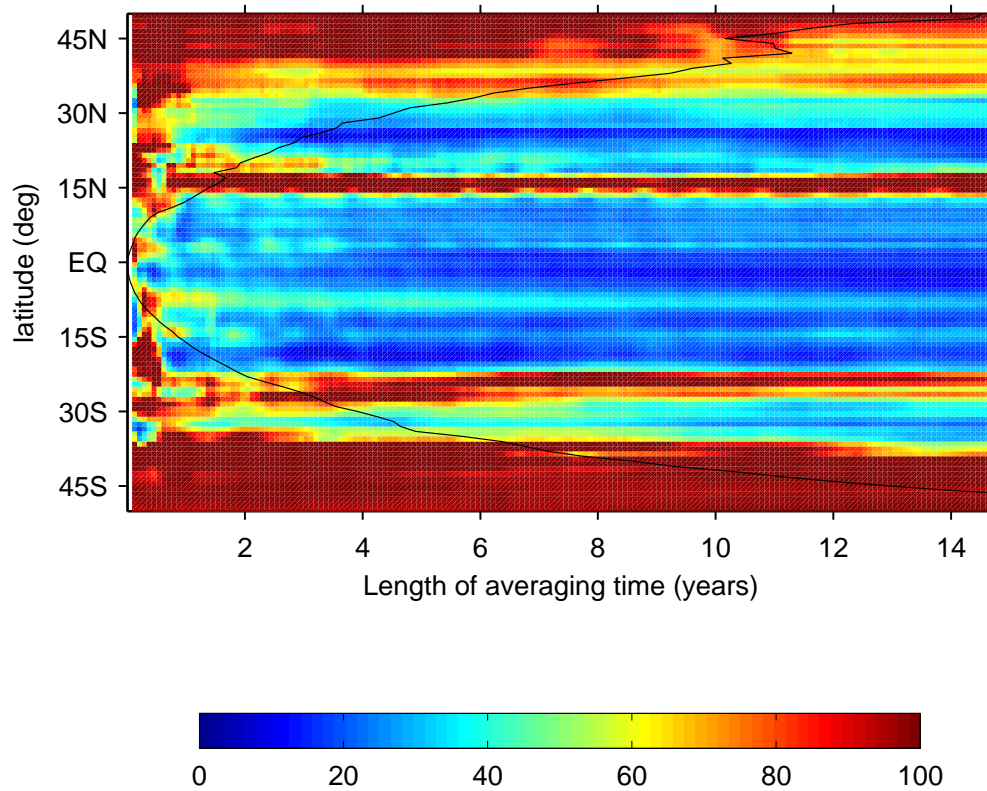


Figure 2.10: M_{zi} in the Atlantic calculated at different latitudes and for different amounts of time averaging. The black line is the basin crossing time of a Rossby Wave propagating at the non-dispersive limit according to the bottom pressure compensation theory of Tailleux and McWilliams (2001). Units are percentages.

smoothed by 5° to lessen the effects of dividing by small values). Consistent with Figure 2.5 Sverdrup balance holds well within the subtropics. The large deviations at approximately 15°N and 24°S are due to dividing by small Sverdrup transports (note that all values of the zonally integrated Sverdrup metric that have been discussed up until this point have been applied over the full interior subtropical domain and so are not affected by problems of dividing by zero). Polewards of approximately 35° the zonally integrated Sverdrup errors are consistently large, even though the time-mean ocean is nearing steady state after 15 years. However, at this latitude the time scale required for the Rossby waves to cross the Atlantic basin is of a similar size to the length of time available in ECCO-GODAE. With the future availability of longer run times it might be found that higher latitude regions are in Sverdrup balance given sufficiently long time averaging.

2.8 Discussion and Conclusions

Results have been presented from the ECCO-GODAE state estimation that show Sverdrup balance holds to a good order of approximation in the subtropical interior ocean when considered over horizontal scales greater than approximately 5° and time averaging scales greater than the Rossby wave basin-crossing time. In particular, when using an optimised integration depth of 2200 m Sverdrup balance explains 69% of the time-mean interior subtropical circulation according to the 5° smoothed pointwise metric M_{pw} , and the basin wide zonally integrated Sverdrup balance explains approximately 80% of the circulation according to the zonally integrated metric M_{zi} (Figure 2.1). On short spatial scales, variability that is present in the wind stress curl but not in the ocean transport invalidates Sverdrup balance. The Sverdrup error is due to a combined error resulting from the assumptions that, a) there is a LONM to integrate to and, b) the ocean vorticity is linear. The LONM error is about a factor of 2 larger than the linear vorticity error when a LONM is chosen at 2200 m depth (Figure 2.3).

It has been verified that the results are largely unaffected by different choices of integration depth. These include the use of a more complicated geovarying depth, such as the depth of an isopycnal (as used in Hautala et al., 1994, not shown) or a mapped depth of small velocity (as used in Wunsch, 2011, and described in Appendix A). So long as the integration depth is everywhere deeper than the main body of the thermocline, but not so deep as to impinge too greatly on deep currents, then the results are not found to vary greatly with the choice of LONM. This is in part because the linear vorticity error alone contributes 21% to the Sverdrup error, which cannot be improved upon by integrating to some optimal depth. Although some improvement in pointwise Sverdrup balance might still be gained by using a method to find a level of smaller vertical velocities, Sverdrup balance at scales greater than 5° are unlikely to change much.

Evidence has been presented in the literature for large Sverdrup errors in the upper interior subtropics (Lu and Stammer, 2004), and eastern boundary (Wunsch, 2011). Additionally, high BPT has been reported in the deep ocean (Bryden, 1980; Bryan et al., 1995) which can potentially put the ocean out of Sverdrup balance. These are valid concerns that are indeed problematic if Sverdrup balance is considered in a pointwise manner

or depth integrated to below approximately 3000 m. In ECCO-GODAE small scale fluctuations introduce Sverdrup errors that are 56% of the magnitude of the Sverdrup transport at an optimum depth of 1 km. When integrated to the bottom, M_{pw} is worsened from 56% to 86% as a result of BPT induced deep currents (Figure 2.7) and a breakdown in linear vorticity balance (Figure 2.8). However, when considered over scales larger than approximately 5° , deep Sverdrup errors lie below a mid-depth LONM that Sverdrup balance can be integrated to (Figure 2.1). Further, when considered over basin wide scales, full-depth integrated Sverdrup balance holds to a good order of approximation since both the linear vorticity errors and level of no motion errors become relatively small at these scales. Note that our results on linear vorticity balance contrast with earlier findings that suggest linear vorticity balance holds well in the deep ocean below 500 m (Lu and Stammer, 2004; Bryden, 1980) but poorly above this depth (Lu and Stammer, 2004).

The extent to which the results can be interpreted as applicable to the real ocean is complicated by inaccuracies in the model physics, the impacts of which can only be speculated on. Perhaps of greatest importance to the realism of Sverdrup balance in ECCO-GODAE is the strength of the deep ocean circulation, which in most models is inaccurate (Wunsch, 2011). In ECCO-GODAE the strength of the time mean North Atlantic Deep Water is more than 5 Sv weaker than that deduced from the RAPID/MOCHA array at 26.5°N (Baehr et al., 2009). If the deep circulation was stronger and its structure unchanged (e.g. the amount of cross isobath flow were to remain the same) then the BPT should increase proportionately. An increased overlap between the upper and lower dynamical regimes may then further disrupt Sverdrup balance beyond what has been shown here. Figure 2.8 is therefore likely to be an underestimate of the effects of BPT, which has been shown to be large in ECCO-GODAE but effectively isolated from the upper layer flow in large scale considerations.

At 1° resolution ECCO-GODAE does not resolve ocean eddies and requires an unrealistically high horizontal viscosity to achieve numerical stability (Griffies, 2004). This may mean that calculations of the curl of advection ($\hat{\mathbf{k}} \cdot \nabla \times \text{ADV}$) in the real ocean would be larger than those presented here, and the curl of horizontal viscosity ($\hat{\mathbf{k}} \cdot \nabla \times \text{HV}$) smaller in the real

ocean. The effect on calculations of Sverdrup balance is unclear, however, since there may be a simple trade off between the contributions of the HV and ADV terms to the Sverdrup error.

The wind stress curl contains more small scale variability in the model than is contained in the ocean transport. In order for ECCO-GODAE to achieve dynamical consistency the adjoint method modifies the input data to achieve a solution that accounts for observational uncertainty. It is possible therefore that model deficiencies have led to modifications of the wind stresses such that the wind stress curls are larger (Lu and Stammer, 2004). For example, the wind stress may have to adopt increased levels of small scale noise in order to accommodate ECCO-GODAE's high frictional dissipation of external forcing. Conversely, it is also possible that in order to account for the high model viscosity the model velocities are made smoother. In the high resolution model, HiGEM (that employs a $1/3^\circ$ eddy permitting ocean), more small scale structure is contained in the ocean transport than in the Sverdrup transport (see Chapter 3). The extent to which Sverdrup balance holds, however, is similar in both models, possibly suggesting that a shift to higher resolution results in a similar magnitude Sverdrup error but a trade off in what is the dominant contributor to the Sverdrup error.

A feature of ECCO-GODAE is that vertical velocities located on different parts of the model grid (the centre point and corner point; Figure 6.3) can be very different, with differences being most pronounced at middle depths where the vertical velocities are at their weakest (Figure 6.4; see Appendix B). Velocities located on the corner point are generally stronger and more variable than those on the centre point. This is worrying and brings into question the realism of the vertical velocities, and particularly Δ_{LONM} which forms the dominant component of the Sverdrup error. It may be the case that, if centre point vertical velocities are more realistic than corner point vertical velocities as a representation of the real ocean vertical velocities, there would possibly exist a more distinct mid-depth LONM to integrate to and therefore an improved Sverdrup balance that holds without requiring horizontal averaging.

Chapter 3

Subtropical Upper Ocean Manifestations of a Reducing AMOC

3.1 Introduction

The northward heat flux associated with the Atlantic Meridional Overturning Circulation (AMOC) is an important part of the climate system, and contributes to the relatively warm temperatures of north west Europe. Climate simulations of the remainder of the twenty first century suggest that growing quantities of atmospheric carbon dioxide will cause a reduction in the strength of the AMOC (IPCC, 2007; Gregory et al., 2005; Thorpe et al., 2001). A significant decrease in northward ocean heat flux may follow. Yet there is currently no clear understanding of how the circulation of the subtropical upper ocean will change. To compensate for a weakened southward deep ocean transport, either the northward surface western boundary current (the Gulf Stream) must weaken, or the southward transport integrated across the basin interior (east of the western boundary current) must increase (or some combination of the two). These two responses could have different implications for ocean heat transport.

Sverdrup theory (Sverdrup, 1947) relates the time-mean depth-integrated circulation in the upper ocean to the curl of the wind stress. In the subtrop-

A concise version of this chapter has been published in *Geophysical Research Letters*. The reference, Thomas et al. (2012), is listed in the bibliography.

ics Sverdrup theory is believed to hold to a good order of approximation in the interior (east of the western boundary current), where the ocean is in linear vorticity balance and there is a presumed level of no motion. Therefore we might expect that, in the absence of a change in the wind, any change in the AMOC will be confined to the western boundary and will manifest itself as a weakening of the southward deep transport compensated by a weakening of the northward flowing surface boundary current. It is non trivial to test the validity of Sverdrup balance in the ocean because the ocean takes a few years to reach this balance (Anderson and Killworth, 1977) and at these time scales wind stress and ocean velocity data are not consistent with each other (Josey et al., 2002). In chapter 2 results were presented from a state estimation product that show Sverdrup balance holds to first order on decadal timescales in the subtropical gyre when considered on scales of the order of 5° or more. However, how Sverdrup balance might change in a warmer climate and its constraint on future change in the AMOC have yet to be established.

Based on hydrographic sections at 25°N , it has been suggested that the AMOC weakened by 30% between the years 1957-2004 (Bryden et al., 2005), a result that has come under question (Searl et al., 2007; Wunsch and Heimbach, 2006). Regardless of whether the AMOC has reduced in strength, the study raises interesting questions about how the 3D structure of the AMOC might change in a warming climate and what the implications are for ocean heat transport. Bryden et al. (2005) suggested that the weakened deep western boundary return flow has been compensated by an increased upper layer southward flow in the basin east of the Florida Straits because no reduction has been observed in the Florida Strait transport (Meinen et al., 2010). Given that the wind stress curl has been constant at this latitude (Atkinson et al., 2010), such a change would imply that this part of the ocean is not in complete Sverdrup balance. The Antilles Current, which is not expected to be in Sverdrup balance (Lu and Stammer, 2004), is included as part of this ‘interior’ basin east of the Florida Straits in the methodology of Bryden et al. (2005). If the Antilles region is the only part east of the Florida Straits that is not in Sverdrup balance, so that AMOC changes are manifested here, then the question of where we define the edge of the western boundary becomes important.

The aim of this chapter is to address the question of how a change in the AMOC will manifest itself in the subtropical North Atlantic. Using a climate projection experiment in the high resolution coupled climate model HiGEM, we establish how upper ocean meridional transport will change when the DWBC weakens, and we determine whether the changes are consistent with Sverdrup balance. This involves clearly defining the interior as that part of the ocean that is expected to be in Sverdrup balance.

In section 3.2 details of the HiGEM model are given and descriptions of the simulations used in the analysis are provided. Section 3.3 describes the extent to which Sverdrup balance holds and continues to hold in the North Atlantic throughout climate change. Section 3.4 identifies how the meridional transport in the interior and western boundary regions of the subtropical North Atlantic arrange themselves to compensate for a weakened southwards deep transport. Section 3.5 then describes how the structure of the temperature, salinity and density are modified as a result of climate change. Section 3.6 outlines changes in the North Pacific and section 3.7 describes what effect the transport reductions have on meridional heat transport. Finally, conclusions are drawn and discussed in section 3.9.

3.2 Model Description

The data used here are from the coupled climate model, HiGEM (Shaffrey et al., 2009), which is based on the Met Office HadGEM1 model (Johns et al., 2006) but has a higher spatial resolution. It uses a spherical lat-lon grid between 90°S and 90°N with a horizontal resolution of 0.83° latitude \times 1° longitude in the atmosphere and an eddy permitting 1/3° \times 1/3° resolution ocean. The increase in ocean grid resolution relative to HadGEM1 allows for a better representation of topographic straits and improvements have been noted in the transport through, for example, the Fram Strait, the Denmark Strait and the Bering Strait (Shaffrey et al., 2009). The ocean component has 40 vertical levels and the atmosphere component has 38 vertical levels, each with uneven spacing to allow higher boundary layer resolution. The ocean and atmosphere initial conditions are taken from the World Ocean Atlas 2001 and ECMWF analysis, respectively.

Annual mean output from two simulations is used. The first is a 150

year control integration in which greenhouse gases are kept constant at present day concentrations. Hereafter this integration is labelled Control. The second simulation is a 100 year integration that is initiated from the Control integration at year 30. The atmospheric concentration of CO_2 is increased by 2% per year for the first 70 years until levels reach 4 times starting values and is then stabilised for the remaining 30 years. Henceforth this run will be labelled $2\%\text{CO}_2$. Since the initial 30 years are not important here, year 1 refers in each case to the first year after that period. Despite the relatively short 30 year spin up time, AMOC drift in the control run is small at $0.004 \text{ Sv year}^{-1}$.

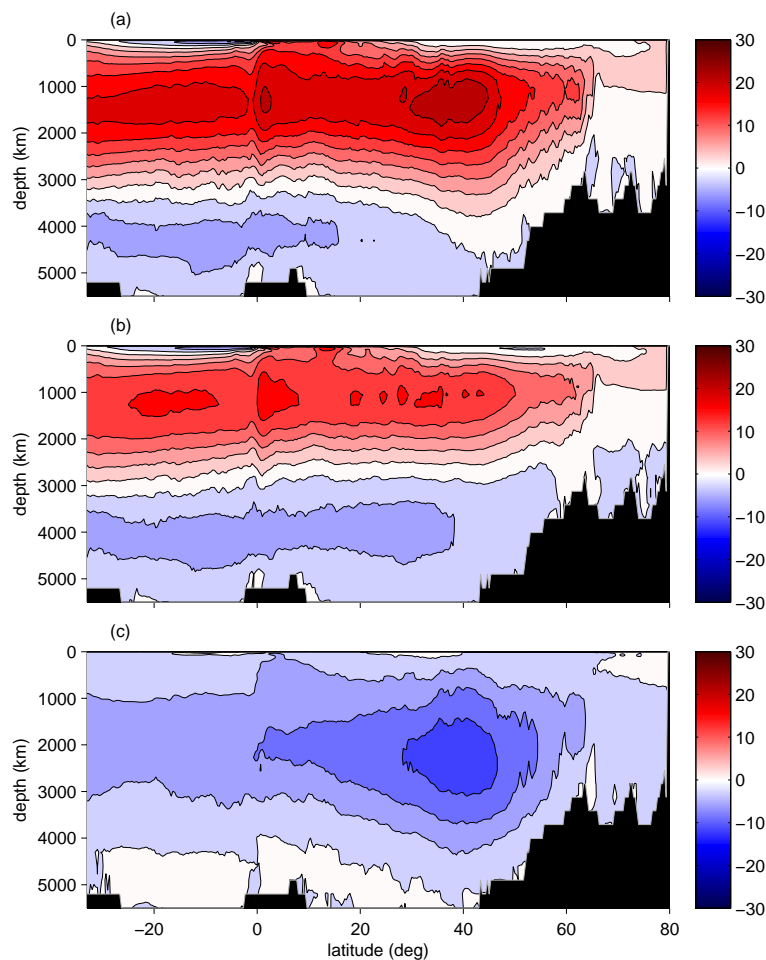


Figure 3.1: The 30 year (years 70-100) time-mean Atlantic meridional overturning streamfunction for (a) the Control run (b) the $2\%\text{CO}_2$ run and (c) their difference ($2\%\text{CO}_2$ minus Control).

The Atlantic meridional overturning streamfunction (equation 1) time-averaged over years 70-100 in the Control and $2\%\text{CO}_2$ scenarios are shown

in Figure 3.1(a) and Figure 3.1(b) respectively, and their difference (2%CO₂ minus Control) is shown in Figure 3.1(c). In each case, the southernmost displayed latitude aligns with the southern tip of the African continent at 33°S since the calculation breaks down here due to the unboundedness of the Southern Ocean. The net northwards flow at each depth follows streamlines clockwise around positive values and vice versa. In the Control and 2%CO₂ runs the northwards flow respectively lies above approximately 1200 m and 1000 m depth throughout the Atlantic. At a latitude of approximately 40°N the net zonal mean meridional flow begins to sink and subsequently return at depth. The overturning cell in the 2%CO₂ run is shallow and weaker (Figure 3.1c) than that in the Control run throughout the Atlantic, particularly north of approximately 20°N. This allows an anticlockwise cell of Antarctic Bottom Water to penetrate further northwards in the 2%CO₂ run relative to the Control.

3.3 Sverdrup Balance in the Subtropical Atlantic Ocean

It is assessed here how well Sverdrup balance holds in the North Atlantic and whether the balance is affected by climate change. The degree to which the ocean is in Sverdrup balance will affect how the meridional transport in the subtropical ocean will change if the AMOC weakens (assessed in section 3.4).

Sverdrup balance refers to the balance between vorticity input to the ocean by the wind and advection of planetary vorticity in the ocean interior. Re-writing equation (11) to incorporate all Sverdrup error terms into a single Sverdrup error, Δ_{SB} (according to the notation defined in section 2.2), gives

$$V = \frac{\hat{\mathbf{k}} \cdot \nabla \times \boldsymbol{\tau}_s}{\rho_0 \beta} + \Delta_{SB}, \quad (14)$$

where Sverdrup balance is the balance between the first two terms and is the depth integral of the linear vorticity terms. As in chapter 2, V is the depth integrated meridional transport (integrated from the surface to some assumed mid-depth level of no vertical motion), $\boldsymbol{\tau}_s$ is the surface wind stress, β is the meridional gradient of the Coriolis frequency, ρ_0 is a

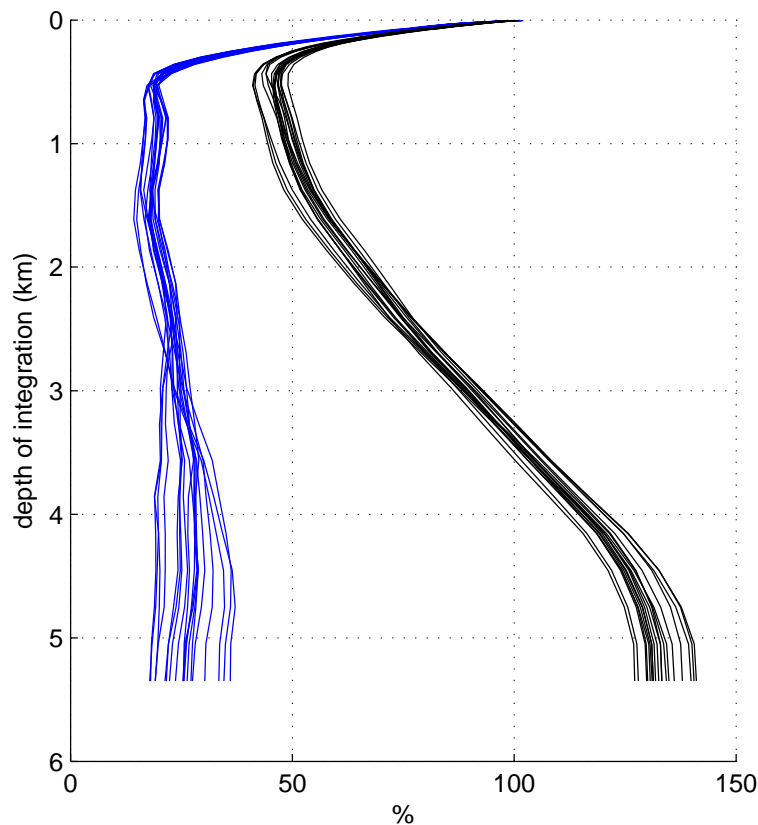


Figure 3.2: Decadal mean M_{zi} (blue) and M_{pw} (black) versus integration depth for 20 different periods of the 2%CO₂ run separated by 5 years. The metrics are applied to interior ocean regions between 35°S and 35°N (see text).

reference density and Δ_{SB} is called the Sverdrup error. The Sverdrup error is the sum of the errors incurred from assuming both linear vorticity, Δ_{LV} , and the existence of a level of no vertical motion, Δ_{LONM} (see Section 2.2). Henceforth V is referred to as the ocean transport and the first term on the right of equation (14) is referred to as the Sverdrup transport.

The ocean comes into Sverdrup balance with the wind forcing by the propagation of baroclinic Rossby waves (Anderson and Killworth, 1977) which limit the transport to the thermocline and isolate it from the bottom topography. To allow for the adjustment period, an averaging time scale of 10 years is applied to all analysis of the Sverdrup balance in this chapter. This period is considered long enough to allow Rossby wave adjustment at any subtropical latitude (Gill, 1982).

The ocean transport is depth-integrated to 1500 m. This depth is chosen from 10 year time averages of two metrics, M_{pw} and M_{zi} , that are used

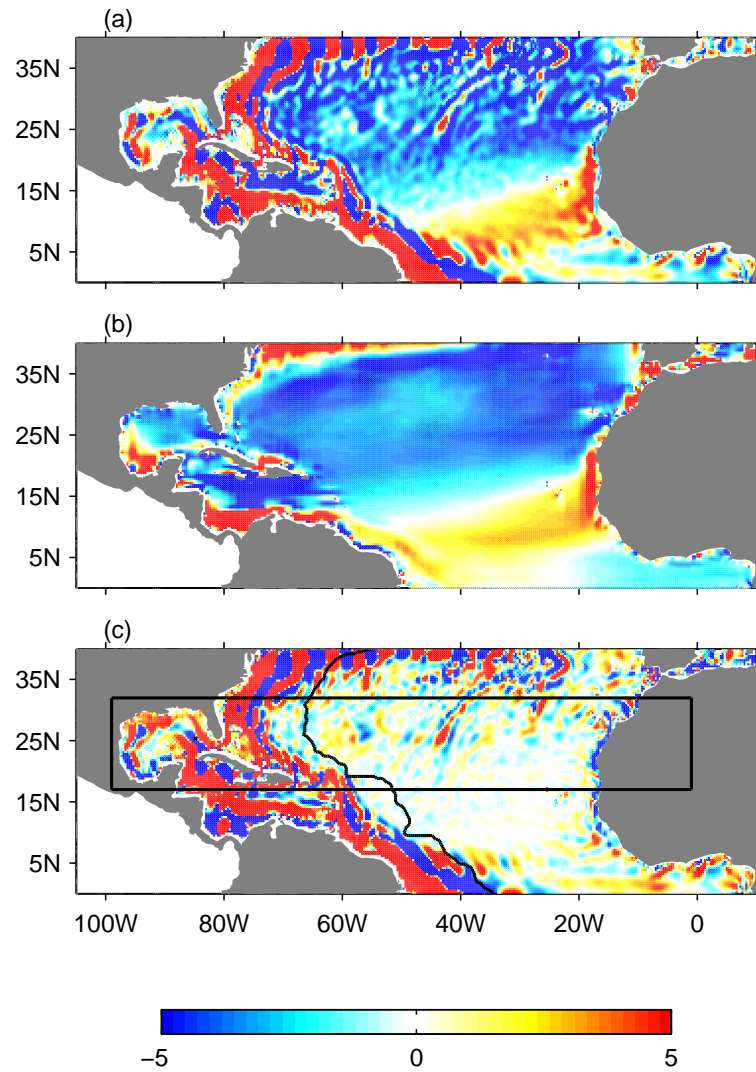


Figure 3.3: North Atlantic transport terms from equation (14), averaged over the first 10 years of the Control run: (a) meridional ocean transport depth-integrated from the surface to 1500 m, (b) Sverdrup transport derived from the wind field and (c) Sverdrup error (the difference between (b) and (a)). The box in (c) outlines the region of focus throughout this chapter and the black line separates the interior ocean and western boundary domains, as defined in the text. Units are $\text{m}^2 \text{s}^{-1}$.

to evaluate how well Sverdrup balance holds in the ocean within a specified domain. The first metric, M_{pw} , describes how well on average Sverdrup balance holds on a pointwise basis while the second metric, M_{zi} , describes how well zonally-integrated Sverdrup balance holds (see section 2.4.3). Figure 3.2 shows the Sverdrup metrics for the 2%CO₂ run for every depth of integration, applied to interior ocean regions away from the western boundary between 35°S and 35°N (according to the same mask as defined in section

2.4.2). The metrics are determined for 20 different decadal means (spaced by 5 years) within the interior domain. Although there exist large transports in the deep ocean associated with topography that cause significant departures from Sverdrup balance when equation (14) is depth integrated to the bottom, 1500 m can be seen to lie consistently between the bulk of the upper ocean currents and the deep currents. Note the similarity between Sverdrup balance in HiGEM, according to Figure 3.2, and Sverdrup balance in ECCO-GODAE, according to Figure 2.1, thereby lending support to the validity of the representation of the ocean circulation in the two models.

Figure 3.3 shows an example of Sverdrup balance in the Control scenario. Each term in equation (14) is time-averaged over the first 10 years. Note that the 10 year Sverdrup balance is similar to that achieved from longer averaging times of e.g. 30 years. Equivalent maps for the 2%CO₂ scenario are not shown since they differ only slightly. Sverdrup balance holds very well in the interior of the ocean under these simple assumptions when considered over scales larger than a few degrees, but relatively poorly on a pointwise basis (Figure 3.2).

The Sverdrup error, Δ_{SB} , can be decomposed into the contributing errors from the assumption of linear vorticity, Δ_{LV} , and of a LONM, Δ_{LONM} (Figure 3.4). Away from the equator the two contribute relatively equally. In the western boundary region between the equator and 35°N, the domain integrated Δ_{LV} is an order of magnitude larger than the domain integrated Δ_{LONM} . This is opposite to the findings in ECCO-GODAE as outlined in the previous chapter, which is likely related to the different resolutions of the two models. Also contrary to the findings from ECCO-GODAE (using an integration depth of 2200 m), in which the two error components commonly spatially vary in phase, the error components in HiGEM (using an integration depth of 1500 m) tend to spatially vary out of phase. It is hypothesised here that conservation of potential vorticity is responsible for the relationship between the two error components (as described in section 2.5 earlier). The differences between the two models may therefore be because of the different effects of permitting eddies rather than parameterising them, or because of the different integration depths used for Sverdrup balance. Further work is warranted to address the differences.

Small scale features in the ocean transport are not reproduced in the

Sverdrup transport, in particular over parts of the Mid-Atlantic Ridge. In this region the assumptions of linear vorticity and of a level of no vertical motion break down due to interactions with the topography (Figure 3.4). Close to the western boundary and at latitudes greater than approximately 35°N Sverdrup balance breaks down entirely. North of this latitude the first baroclinic Rossby wave phase speeds match the background flow speeds so that the ocean transport is not able to fully adjust to wind forcing. When this happens the water column becomes more barotropic which acts to increase the Sverdrup error, Δ_{SB} , because the interaction between wind driven currents and topography leads to vertical motion (Hughes and de Cuevas, 2001). The western boundary break down occurs generally within about 700 km of the coast, but in some regions the break down extends as far as 1000 km from the coast. It occurs because non-linearity is relatively large in the vorticity equation here, and there is substantial deep flow. Deviations from Sverdrup balance are also evident close to the eastern boundary where small non-linearities and interaction with bottom topography become more important. The ocean is henceforth split into two domains which are defined as a western boundary domain that includes most of the regions where Sverdrup balance entirely breaks down in the Control run when integrated to a mid-depth level, and a remaining interior ocean domain (see section 2.4.2). The black line in Figure 3.3(c) delineates the boundary between the two domains and is chosen as the line that runs 1000 km east of the 2000 m depth contour. At 27°N this definition means that the western boundary region includes both the Florida and Antilles Currents. It has been verified that the use of a more complicated boundary delineation based on the Sverdrup error, Δ_{SB} , makes little difference to the results.

Of primary interest in the context of a changing AMOC is the zonally integrated Sverdrup balance. To assess differences in the Sverdrup interior transport between the Control and $2\%CO_2$ scenarios, zonally integrated decadal mean transports (depth-integrated to 1500 m) are calculated for the years 70-80, a period after the point at which atmospheric CO_2 has stopped increasing. Figure 3.5 shows the zonally integrated interior ocean transport and Sverdrup transport in the interior domain for each scenario at each latitude between the equator and 40°N . Zonally integrated Sverdrup balance holds very well in the subtropics for both the Control and $2\%CO_2$ scenarios.

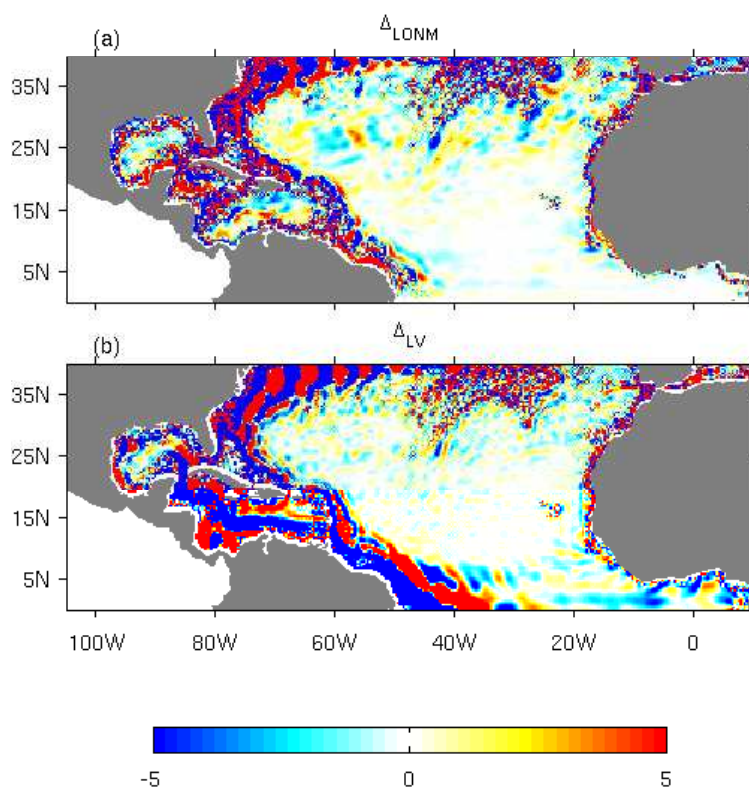


Figure 3.4: Decadal mean (years 1-10) component errors of the Sverdrup error, Δ_{SB} , (a) LONM error, Δ_{LONM} , (b) linear vorticity error, Δ_{LV} . Depth integrations are made to 1500 m. Units are m^2s^{-1} .

This indicates that zonally integrated Sverdrup balance holds to first order throughout a changing climate, and that the small scale interior Sverdrup errors evident in Figure 3.3c tend to cancel out once zonally integrated.

The zonally integrated interior ocean transport is weaker throughout the subtropical gyre in the 2%CO₂ experiment and this is consistent with a weakened Sverdrup transport relative to the control (Figure 3.5). This decrease in zonally-integrated meridional transport in the interior takes place at all latitudes in the subtropical North Atlantic (Figure 3.5c). This is unrelated to the changes in AMOC and therefore is not one of the two possible flow compensation scenarios outlined in the introduction.

3.4 Transport trends

Here we analyse how variables relevant to Sverdrup balance change during a reducing AMOC in the 2%CO₂ run. The AMOC at 26.7°N (defined as the

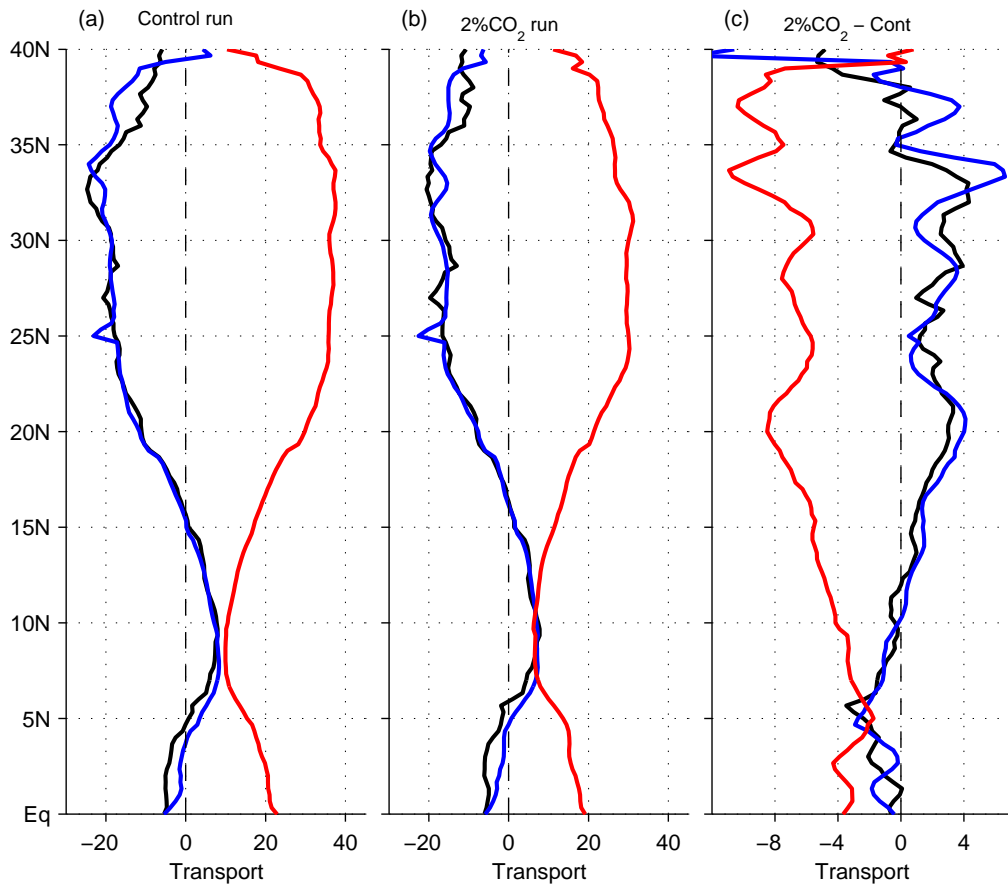


Figure 3.5: Decadal mean (years 70 to 80) North Atlantic zonally integrated Sverdrup transport (black line), interior ocean transport (depth integrated to 1500 m; blue line) and western boundary transport (red line) versus latitude. Transports are shown for (a) the Control run, (b) 2%CO₂ run and (c) the difference (2%CO₂ minus Control). The dashed vertical line marks zero transport. Transports are positive northwards and units are Sverdrups ($10^6\text{m}^3\text{s}^{-1}$).

maximum streamfunction between depths 500 m and 2500 m) reduces from approximately 21 Sv to 15 Sv between years 1 and 70 whilst CO₂ levels are increasing, and then stabilises once CO₂ is kept constant (Figure 3.6a). A Control run AMOC of 21 Sv lies within the error margins of the RAPID array estimates (<http://www.noc.soton.ac.uk/rapidmoc/>). Figure 3.6 shows time series of (b) the deep southward transport, (c) the upper ocean western boundary current, (d) the upper ocean interior transport, and (e) the Sverdrup transport during the 2%CO₂ run. Throughout this section, unless stated otherwise, transport values refer to the annual mean, meridionally averaged, zonally integrated, transport within the domains shown

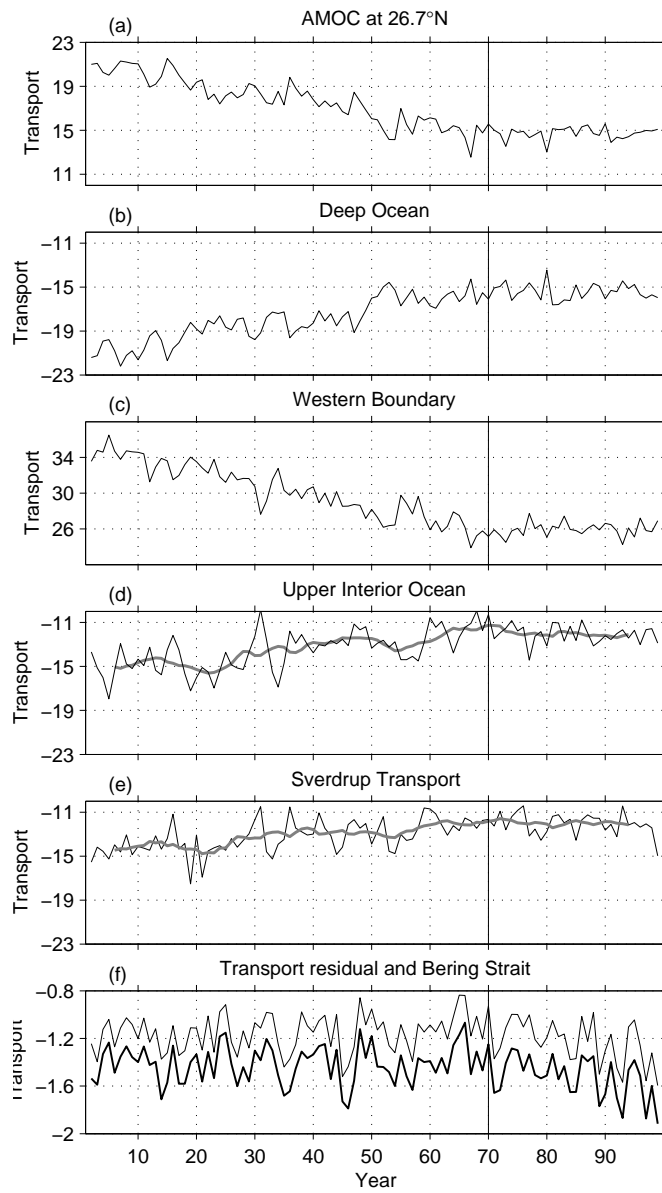


Figure 3.6: Time series in the North Atlantic of (a) maximum AMOC at 26.7°N, (b) transport in the deep ocean, (c) upper ocean western boundary transport, (d) transport in the upper interior ocean, (e) Sverdrup transport, (f) the sum of the component transports in (b)-(d) (bold line) and the Bering Strait transport (thin line). The transports in (b)-(e) are zonally integrated and averaged between 17°N and 32°N. Grey lines show smoothing at 10 years. The vertical line marks the year at which CO₂ stops increasing and remains steady. All transports are positive northwards and units are Sverdrups.

in Figure 3.3(c). The southern boundary of the integration region is chosen to lie at 17°N and is approximately at the southern edge of the subtropical gyre. The northern boundary is at 32°N and is where Sverdrup balance errors begin to become large. To calculate the upper ocean western boundary transport the depth of integration used is the one that encompasses the maximum northward transport and this depth is calculated at each time step. The depth of integration in the interior is kept constant at 1500 m. The deep ocean transport is calculated as a basin wide integral over the remaining ocean cross-section. This methodology means it can be ascertained whether changes in the total southwards deep transport are balanced in the northwards boundary current transport or the southwards Sverdrup interior transport.

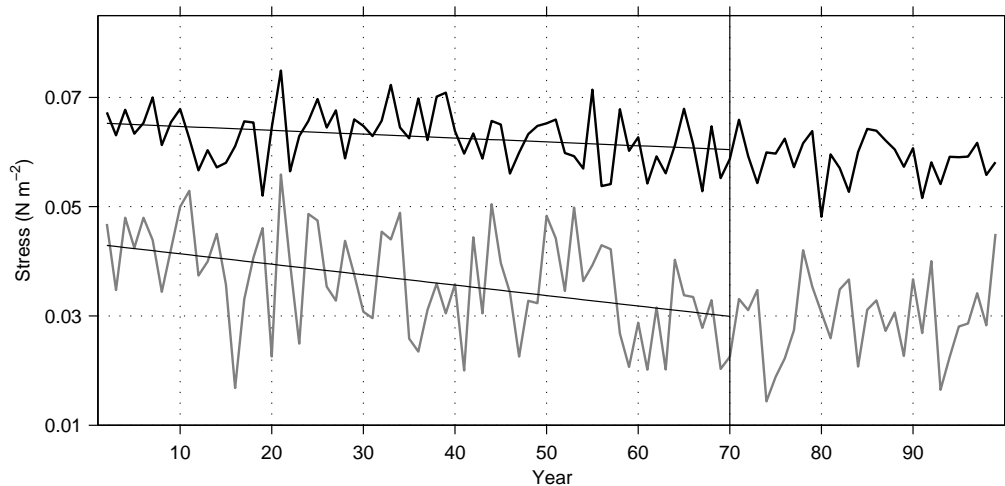


Figure 3.7: Atlantic interior ocean domain averaged zonal wind stress in the region of the trade winds (black line; averaged between 10° - 25°N) and westerlies (grey line; averaged between 35° - 45°N). The vertical line marks the year at which CO_2 stops increasing. Black lines show the linear trends calculated over the first 70 years. Units are N m^{-2} .

The domain integrated southward deep ocean transport reduces by 5.3 Sv during the 70 years of increasing CO_2 before stabilising (Figure 3.6b). The reduction is calculated by subtracting a 30 year mean of the Control from the final 30 years of the $2\%\text{CO}_2$ simulation. This decrease is large in comparison with the interannual standard deviation of approximately 1.3 Sv. The interior ocean transport reduces by 3.0 Sv (compared to an interannual standard deviation of approximately 1.4 Sv). The smoothed time series of interior ocean transport corresponds closely to the time series of

Sverdrup transport; weakening of both is a result of climate change induced weakening of the wind stress curl at subtropical latitudes. The warming climate leads to weaker trade winds and westerlies. Figure 3.7 shows the trade winds and westerlies calculated as the interior ocean domain averaged zonal wind stress between 10° - 25° N and 35° - 45° N respectively (the latter lies over a southern section of the westerlies, but the effect on the subtropics is of interest here). A full description of the atmospheric changes in the HiGEM 2%CO₂ run can be found in Catto et al. (2011). A reduction in trade wind strength appears to be a robust feature of future climate model simulations as a result of a weaker Hadley Cell. However, westerly winds are more commonly shifted polewards than they are weakened (Lu et al., 2008). Only a relatively minor northwards shift takes place here in the 2%CO₂ run (Catto et al., 2011). Figure 3.8 shows decadal mean (years 70-80) zonal wind stress in the Atlantic during the Control and 2%CO₂ run, and their difference and zonal integrals (within the interior ocean domain). Reductions in zonal wind stress are greater at mid-latitude and take place quite uniformly away from the western boundary.

The upper ocean western boundary current weakens by 8.4 Sv (Figure 3.6c) in total since it changes to compensate for both the 5.3 Sv decrease in deep ocean transport (a weakened AMOC) and the 3.0 Sv decrease in interior upper ocean transport (a weakened subtropical gyre). The 0.1 Sv residual (after taking account of the Bering Straits throughflow) can be explained by a difference in the freshwater flux between the Control and 2%CO₂ scenarios.

The meridional averaging applied to the transports provides an overall picture of the meridional overturning trends instead of showing only the details of a few single latitudes that each undergo a different circulation response to climate change (Figure 3.5c). Figure 3.9 shows the time series and trends of the transports at 10 individual latitudes between 23° N and 33° N. While transports and trends in the deep ocean and upper western boundary current are strongly consistent at each latitude, the interior ocean transports and Sverdrup transports show more latitudinal differences. Of the 10 trends shown, 8 of the ocean transport trends are statistically significant at 95% over the first 70 years (significance is calculated according to appendix B) and 7 of the Sverdrup transport trends are significant at 95%.

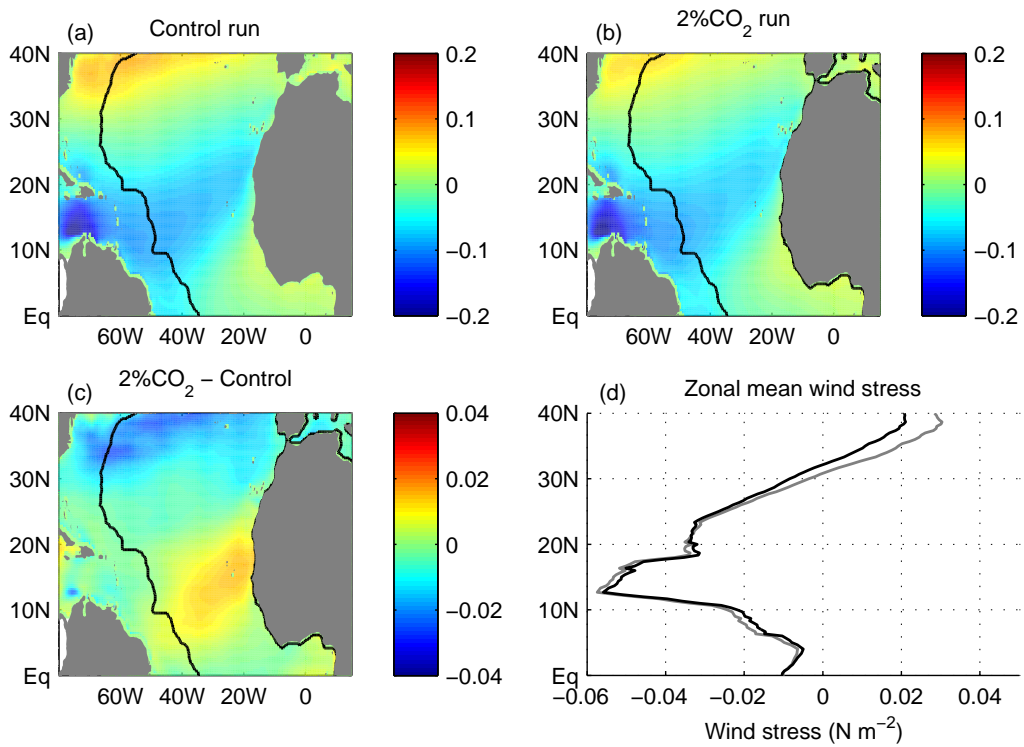


Figure 3.8: Decadal mean (years 70-80) zonal wind stress in the North Atlantic in (a) the Control run (b) the 2%CO₂ run and (c) their difference (2%CO₂ - Control). (d) Zonal wind stress for the Control (Grey) and 2%CO₂ (black), zonally averaged in the ocean interior (from the eastern boundary to the black line in plots (a) to (c)). Units are N m⁻².

All transport trends in Figure 3.6 are significant at 95%.

Under conditions of increasing CO₂ it might be expected that Sverdrup balance will improve. There are two reasons to expect this. Firstly, a reduction in deep ocean transport implies a smaller Bottom Pressure Torque (BPT; see section 1.2.1) and hence smaller Δ_{LONM} . Secondly, increased subtropical surface warming can be expected to increase the upper layer stratification. Anderson and Killworth (1977) posited that the steady state circulation in a wind forced ocean is confined to the strongly stratified layer. An increase in stratification therefore implies a more strongly bounded upper ocean time mean circulation that might be more isolated from deep transports and topography. To test changes in Sverdrup balance, time series of the mean absolute pointwise (Figure 3.10a) and zonally integrated (Figure 3.10b) sverdrup errors (Δ_{SB}) are calculated within the upper interior domain shown in Figure 3.3(c). No trend, significant at the 95% level,

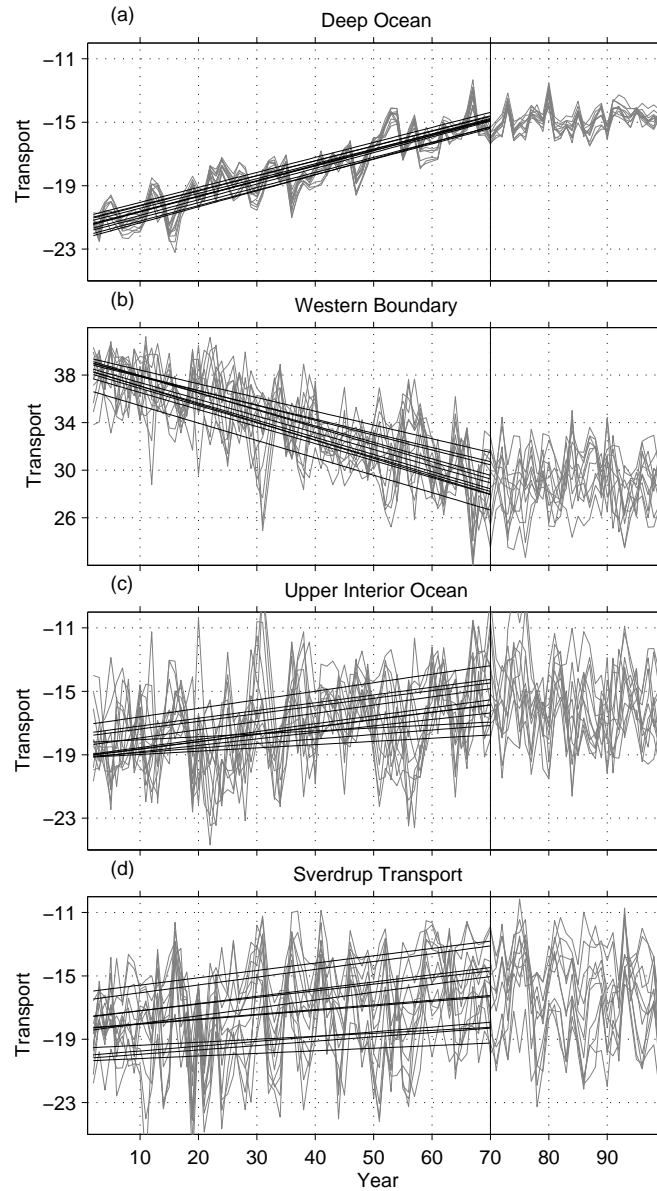


Figure 3.9: Time series at 10 latitudes between 23°N and 33°N in the North Atlantic (grey lines) of (a) transport in the deep ocean, (b) upper ocean western boundary transport, (c) transport in the upper interior ocean, (d) Sverdrup transport. Trends over the first 70 years of each time series are shown (black lines). The vertical line marks the year at which CO₂ stops increasing and remains steady. All transports are positive northwards and units are Sverdrups.

was found in either the pointwise or zonally integrated Sverdrup error in the Atlantic over the first 70 years of the 2%CO₂ scenario. The time averages of the zonally-integrated Sverdrup error in the Control and 2%CO₂ scenarios are respectively 1.1 Sv and 0.9 Sv when meridionally averaged between 17°N and 32°N.

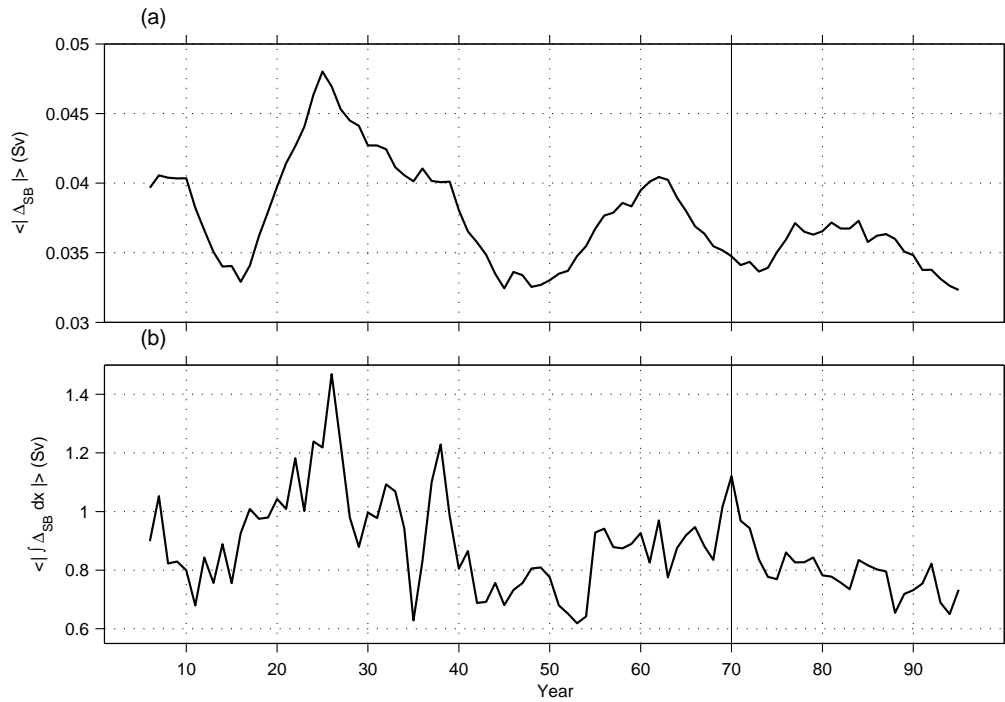


Figure 3.10: Time series of the Atlantic interior domain-averaged absolute (a) pointwise ($\langle |\Delta_{SB}| \rangle$) and (b) zonally integrated ($\langle |\int \Delta_{SB} dx| \rangle$) Sverdrup error for decadal mean transports. Values are meridionally averaged between 17°N and 32°N and calculated using an integration depth of 1500 m. The vertical line marks the year at which CO₂ stops increasing and remains steady.

The upper western boundary domain defined in this study encompasses a portion of the ocean that is commonly included as part of the interior ocean in hydrographic calculations made at 26.5°N (e.g. Bryden et al., 2005). It is important, however, to remember that the Antilles Current to the east of the Bahamas is a part of the western boundary current system that is not constrained by Sverdrup balance (Figure 3.3). To understand how the distribution of changes take place within the upper western boundary region in our model 2%CO₂ simulation at 27°N, timeseries of the Antilles Current and Florida Current are calculated. The Antilles and Florida currents are defined as the zonally integrated transport on the east and west sides of the

Bahamas at 27°N respectively (Figure 3.11).

Both the Florida Current and Antilles Current weaken, with the latter reducing most. The different degrees of weakening suggest that the Antilles Current may be controlled by dynamics that differ from those in the Florida Straits. Note that the trends in Figure 3.6(f) could be misleading because the Antilles Current in HiGEM is too strong relative to observations (Meinen et al., 2004) since it is compensating for a too weak transport through the Florida Straits (Shaffrey et al., 2009). The results, however, suggest that not all potential changes in the upper western boundary current will necessarily occur in the Florida Current, and hence in order to gain a full understanding of the structure of AMOC changes in the subtropical ocean, the full upper western boundary region must be considered.

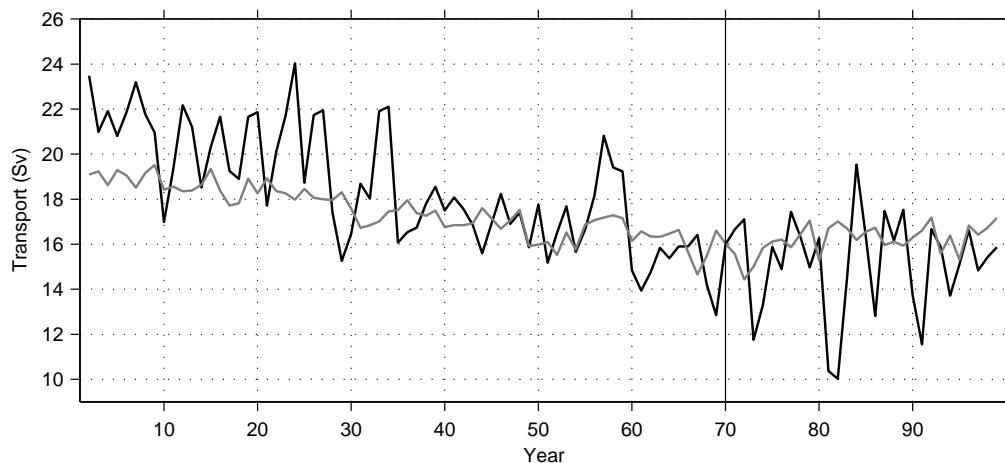


Figure 3.11: Transport time series of the Florida Current (grey line) and the Antilles Current (black line) calculated as zonal integrals at 27°N between 280°-282°W and 283°-288°W respectively. The vertical line marks the year at which CO₂ stops increasing. Units are Sverdrups.

3.5 Changes in Ocean Properties

Warming of the upper North Atlantic Ocean during the second half of the 20th century has been more pronounced on the western side of the basin than on the eastern side (Bryden et al., 2005; Levitus et al., 2000). Such western warming would lead to an enhanced zonal temperature gradient across the Atlantic basin and, if salinities remained unchanged, a greater zonal density gradient. In such a case, interior upper ocean southward

transport would increase in accordance with thermal wind balance. However, Figure 3.5 and Figure 3.6 show a weakening of the upper ocean interior transport, suggesting an important role for salinity in the circulation changes.

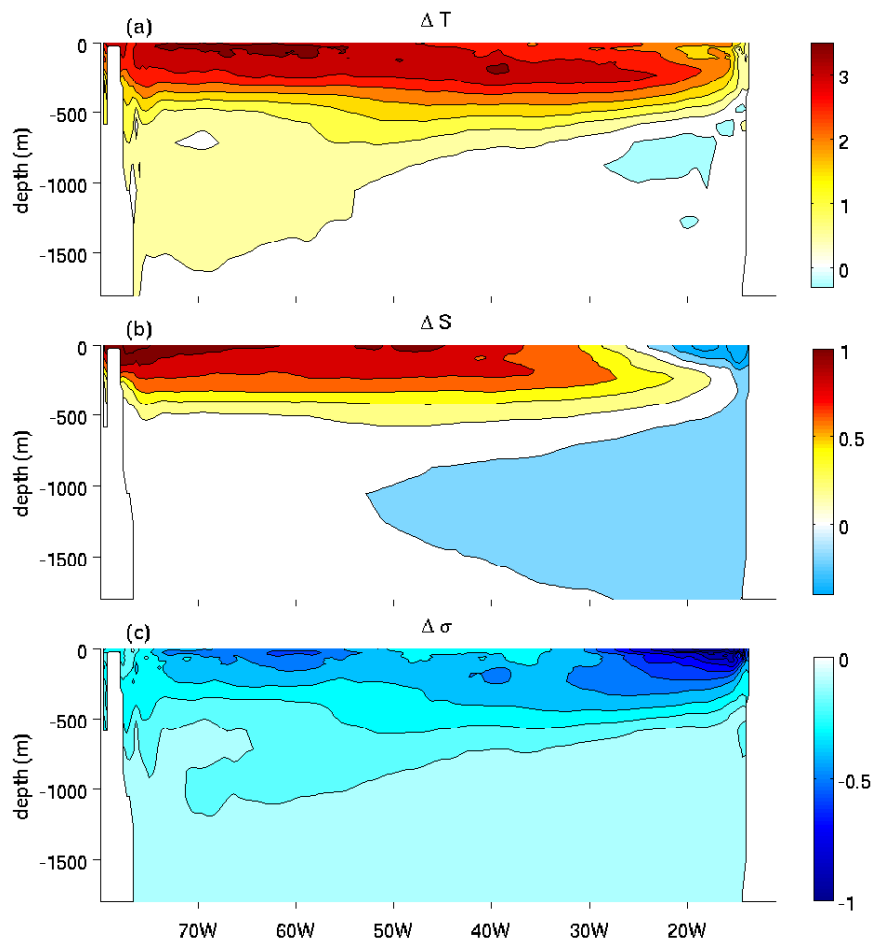


Figure 3.12: Decadal mean (years 70-80) zonal cross-section differences in (a) temperature ($^{\circ}\text{C}$), (b) salinity and (c) potential density (referenced to 2000 m; kg m^{-3}) between the 2% CO_2 and Control scenarios (2% CO_2 minus Control) along 27°N in the Atlantic.

To investigate how the change in upper interior ocean transport relates to ocean property changes, zonal cross-sections of the temperature, salinity and potential density (referenced to 2000 m) fields at 27°N in the Atlantic are considered. Figure 3.12 shows the differences between the 2% CO_2 and Control runs for these variables time-averaged over years 70 to 80. Consistent with the observations, the western side of the basin warms the most under climate change in HiGEM. However, salinification also occurs in the

upper ocean and is greatest in the west. Whereas warming occurs across the full zonal extent of the basin, salinification occurs only over about 70% of the basin in the west. The combined effect of changes in temperature and salinity on the density is that warming in the west is largely offset by a rise in salinity, while (relatively less) warming in the east is reinforced by freshening. As a result, the largest density reductions take place at the eastern end of the zonal section. Zonal density gradients are therefore reduced and the southward geostrophic transport decreases accordingly. At depths greater than approximately 500 m the pattern is reversed such that the density in the east is increased relative to the west. However, density changes of the upper 500 m dominate the change in the geostrophic flow.

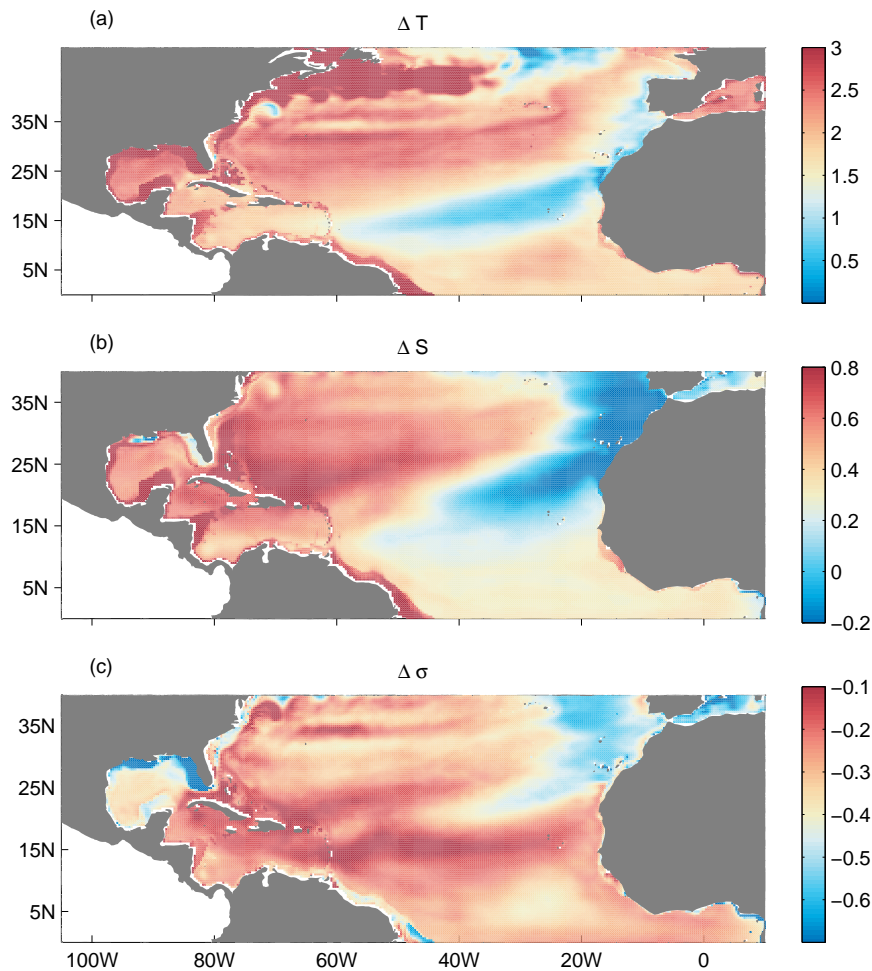


Figure 3.13: Decadal mean (years 70-80), upper 1500 m average, difference in (a) temperature ($^{\circ}\text{C}$), (b) salinity and (c) potential density (referenced to 2000 m; kg m^{-3}) between the 2%CO₂ and Control scenarios (2%CO₂ minus Control) in the Atlantic.

Figure 3.13 shows maps of the difference between the Control 2%CO₂ runs, in temperature, salinity and potential density (referenced to 2000 m) depth-averaged over the upper 1500 m and time-averaged between years 70 and 80 in the North Atlantic. The patterns shown in Figure 3.12 along 27°N are similar throughout the subtropical gyre, with a freshening and warming of the eastern side of the basin that leads to the greatest density reductions in the subtropical gyre. Despite strong salinification of the western subtropics densities are reduced everywhere because of the dominant effect of warming.

3.6 Pacific Ocean transports

In this section, an analysis of the transport and wind stress changes is made for the North Pacific Ocean. Because the Pacific overturning is so small, any transport responses to climate change might be expected to be due only to wind stress curl changes. Similar to the analysis described for the Atlantic ocean in section 3.4, transports in this section refer to the annual mean, meridionally averaged, zonally integrated, transport within equivalent domains to those shown in Figure 3.3(c). The upper ocean western boundary transport is integrated down to the depth that encompasses the maximum northward transport and this depth is calculated at each time step. The depth of integration in the interior is kept constant at 1500 m. The deep ocean transport is calculated as a basin wide integral over the remaining ocean cross-section.

Figure 3.14 shows the North Pacific transports in (a) the deep ocean, (b) the upper ocean western boundary, (c) the upper interior ocean, (d) the Sverdrup transport and (e) their residual and Bering Strait transport. Fluctuations in the residual transport closely resemble those in the Bering Strait transport, and the difference between them is suggested to represent the freshwater flux. Transport differences between the 30 year mean (years 70-100) Control and 2%CO₂ runs are 1.9 Sv, 3.7 Sv and 5.6 Sv in the deep ocean, upper western boundary and interior domains respectively. As with the North Atlantic, interior ocean transports are correlated with Sverdrup transports, when smoothed at 10 years. In the North Pacific, contrary to the North Atlantic, the reduced wind stress curl is due to a weakening

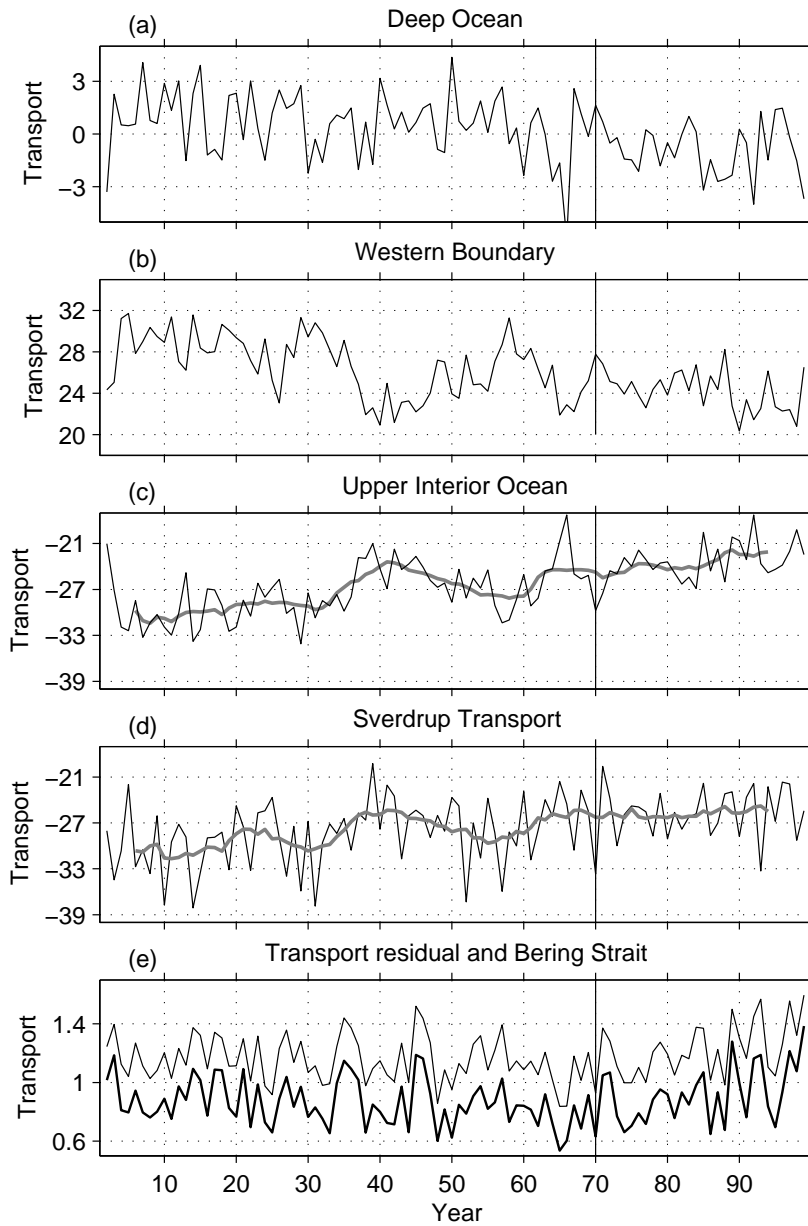


Figure 3.14: Time series in the North Pacific of (a) transport in the deep ocean, (b) upper ocean western boundary transport, (c) transport in the upper interior ocean, (d) Sverdrup transport, (e) the sum of the component transports in (a)-(c) (bold line) and the Bering Strait transport (thin line). The transports in (a)-(d) are zonally integrated and averaged between 17°N and 32°N . Grey lines show smoothing at 10 years. The vertical line marks the year at which CO_2 stops increasing and remains steady. All transports are positive northwards and units are Sverdrups.

trend in the trade winds (calculated as the interior domain-mean wind stress between 10°N - 25°N) that is significant to 95% confidence. The westerly winds (calculated as the interior domain-mean wind stress between 35°N - 45°N) have a small yet not significant (at the 95% level) increase over the years 1-70 (Figure 3.15). The reductions in trade winds are consistent across the interior domain (Figure 3.16). At mid-latitudes reduced wind stress on the western side of the basin is compensated by increased wind stress on the eastern side with the result that the zonal mean change is small.

It is interesting that in the North Pacific, the deep transport switches from being northward to southward during the $2\%CO_2$ run. The result is that the largest changes take place in the interior ocean transport due to changes in the wind stress curl, since the upper western boundary current reduction must also compensate (by increasing slightly) for the reversal in deep transport. This implies an increase in water mass sinking at high North Pacific latitudes, opposite to the North Atlantic. Such competition between North Atlantic and North Pacific sinking has been noted before by studies using an ocean general circulation model coupled to an energy-moisture balance model (de Boer et al., 2008; Saenko et al., 2004).

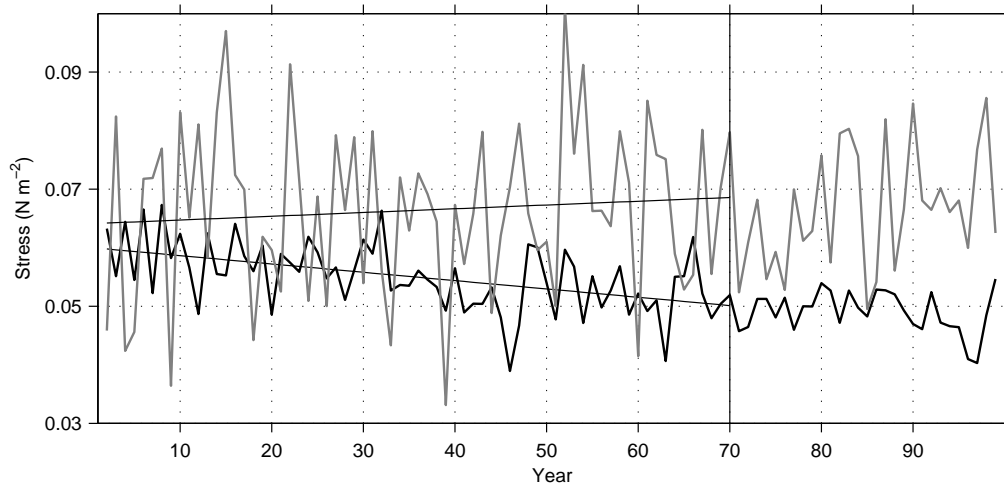


Figure 3.15: Pacific interior ocean domain averaged zonal wind stress in the trade winds (black line; averaged between 10° - 25°N) and westerlies (grey line; averaged between 35° - 45°N). The vertical line marks the year at which CO_2 stops increasing. Black lines mark show the linear trends calculated over the first 70 years. Units are N m^{-2} .

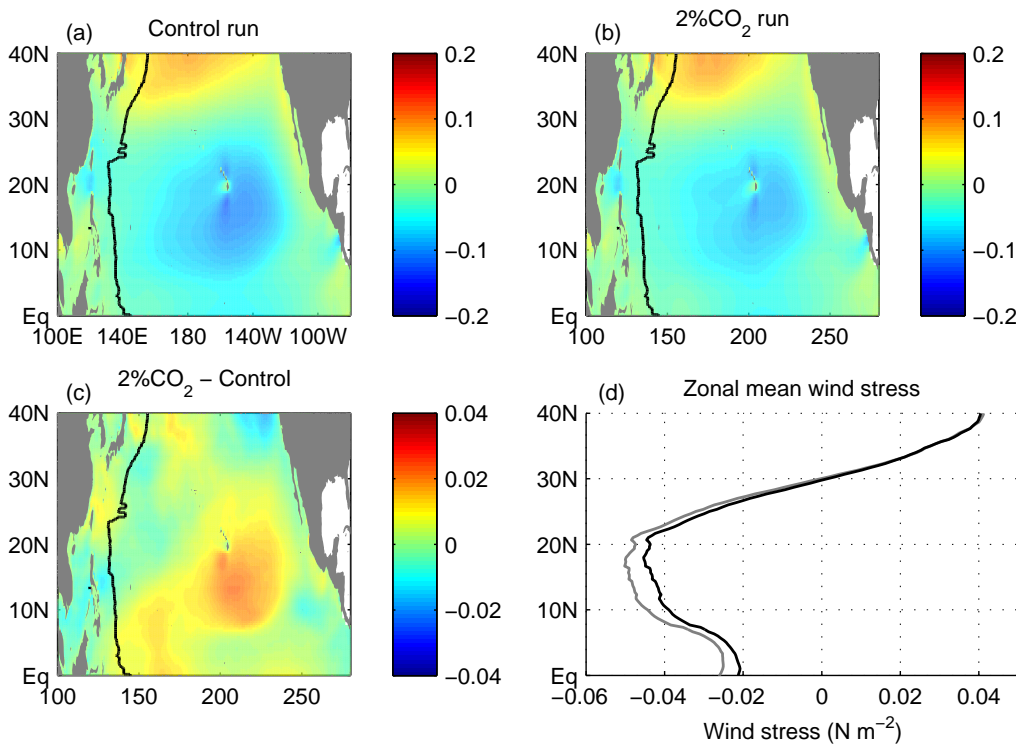


Figure 3.16: Decadal mean (years 70-80) zonal wind stress in the North Pacific in (a) the Control run (b) the 2%CO₂ run and (c) their difference (2%CO₂ - Control). (d) Zonal wind stress for the Control (Grey) and 2%CO₂ (black), zonally averaged in the ocean interior (from the eastern boundary to the black line in plots (a) to (c)). Units are N m⁻².

3.7 Heat transport changes

The heat transported meridionally by the ocean is important for the climate. This section addresses the importance, with respect to heat transport, of whether weakened southwards deep Atlantic transports are compensated by increased southwards interior ocean transports or by decreased northwards upper western boundary transports. This is investigated using a cross section of decadal mean velocities and temperatures at 26.7°N in the Atlantic, a latitude that is representative of the subtropical gyre circulation and can be used for comparison to the RAPID array measurements (Johns et al., 2011). The cross section is split into three domains, an upper western boundary domain, an upper interior domain and a deep domain (c.f. Figure 1.9). The boundary between the western boundary and interior ocean lies 1000 km offshore of the 2000 m isobath (the location of the black line at 26.7°N in Figure 3.3). In the upper western boundary domain the depth of integration

used is the one that encompasses the maximum northward transport. The depth of integration in the interior is kept constant at 1500 m. The deep ocean domain is the remaining cross-section region.

To simulate an overturning reduction, idealised adjustments are made to the Control velocities in the deep ocean and separately compensated by idealised adjustments made in one of the upper domains. An idealised reduction to velocities in the deep domain is done by uniformly changing all velocities in the domain such that the total transport is weakened by 30%. The velocities in one of the upper domains then compensate in a similar manner. Two scenarios are calculated in response to a 30% reduction in deep transport. In scenario 1 the upper western boundary velocities are uniformly weakened to compensate for the reduction in the southwards deep transport. In scenario 2 the interior velocities are uniformly strengthened as compensation for the reduction in deep transport.

The total heat transport within each domain is calculated according to,

$$Q = \int \int \rho c_p v \theta \, dx \, dz, \quad (15)$$

where ρ is the seawater density, c_p is the specific heat of seawater and θ is the potential temperature (in °C). The net cross section meridional heat transport is then the sum of Q from each of the three domains. In scenarios 1 and 2 the modified velocities are used with decadal mean temperatures from the 2%CO₂ run. The scenarios are compared to a reference scenario that uses decadal mean velocities and temperatures from the Control run. Note that the meridional velocity changes made here are not consistent with the thermal wind relation and so the methodology can be expected to give only an approximation.

In scenario 1 the net cross section meridional heat transport is 21% weaker than in the reference scenario. In scenario 2 the net heat transport is 22% weaker than in the reference scenario. Note that the percentage reductions in the net heat transport are smaller than the 30% percentage reduction in the deep heat transport because of the higher upper ocean temperatures in the 2%CO₂ run.

In HiGEM it is therefore of little consequence to heat transport if compensation to a deep transport reduction is made in the interior or upper western boundary circulation. This is because the temperature of water

flowing northwards in the upper western boundary current is similar to the temperature of the southwards interior ocean flow. As a result, the model heat transport of the horizontal gyre circulation in the North Atlantic is small compared with that of the overturning circulation which involves a large temperature difference between the surface and deep ocean transports. This result is supported by a diagnosis of the heat transported by the horizontal and vertical components of the circulation in HiGEM (Shaffrey et al., 2009) and with ocean observations taken at 26.5°N (Johns et al., 2011). The heat transfer to the atmosphere in the North Atlantic is therefore sensitive to changes in the strength of the deep transport but not to changes in the strength of the gyre circulation. In the South Atlantic, however, the gyre contributes more significantly to the total northward heat transport (Shaffrey et al., 2009) suggesting that the structure of changes in the AMOC may have a larger impact on heat transport here.

3.8 HiGEM steady state averaging time

The results in the previous chapter have indicated that Sverdrup balance holds to a good order of approximation (see section 1.2.1 for a definition of a good order of approximation) in the North Atlantic subtropical ocean on decadal periods up to latitudes of approximately 35°. Decadal periods are sufficient to allow the ocean to come into approximate Sverdrup balance by Rossby wave adjustment at any subtropical latitude. This section addresses whether higher latitudes would reach Sverdrup balance after longer time periods. The analysis presented in section 2.7 using the ECCO-GODAE model is repeated here with HiGEM because the longer time series allows us to determine how long it takes for the Sverdrup balance terms to reach steady state at mid-latitudes and higher. When enough time averaging is applied such that the ocean is no longer adjusting then the system will have reached the best possible Sverdrup balance that it can achieve. The equilibrium time scale is determined by first calculating the 120 year time series of the zonally integrated Sverdrup error at each latitude and cumulatively averaging it in steps from 1 year to 120 years. A five year running standard deviation is then applied at each latitude to give the Sverdrup error fluctuation. A high Sverdrup error fluctuation means that the ocean has not yet reached

equilibrium.

The latitude variation of the Sverdrup error fluctuation (Figure 3.17a; see section 2.7) and the zonally integrated Sverdrup metric, M_{zi} (Figure 3.17b) are calculated for increasing averaging time scales of the HiGEM Control run. While latitudes polewards of approximately 35° come close to reaching steady state after 120 years of time averaging, the zonally integrated transports remain consistently out of Sverdrup balance throughout the run. This indicates that Sverdrup balance is not valid at these latitudes even after long-term averaging.

Rossby waves are not responsible for the ocean adjustment at mid-latitudes and higher. Outside of the subtropics the time scales of adjustment no longer compare well to the basin crossing time of Atlantic Rossby waves. A map of the 120 year time averaged Sverdrup errors (Figure 3.18) confirms the presence of large persistent deviations from Sverdrup balance outside of the subtropics. Figure 3.18 also reveals small scale Sverdrup errors that remain even in the interior ocean away from boundary currents. This supports and extends recent findings that show small scale Sverdrup errors to persist in a 16 year average of a 1° state estimation (Wunsch, 2011).

3.9 Conclusions

This study has determined how meridional transports, averaged between 17°N and 32°N in the subtropical North Atlantic, re-organize themselves during a CO_2 forced reduction in AMOC strength in the HiGEM high-resolution coupled climate model. A 5.3 Sv reduction in southward deep transport takes place over 70 years of increasing CO_2 at 2% per year. During the remaining 30 years of the run, when CO_2 levels are held constant, the deep transport remains stable. The main result of this study is that the weakening of the model southwards deep transport is balanced solely by a weakening of the northward upper ocean western boundary current, and not by a strengthening of the interior ocean transport (Figure 3.6). This is because the interior ocean of HiGEM is in Sverdrup balance throughout the changing climate of the 2% CO_2 scenario (despite the relatively simple assumption that there is always a level of no vertical motion at 1500 m), and because the wind stress curl does not increase. Our results suggest that

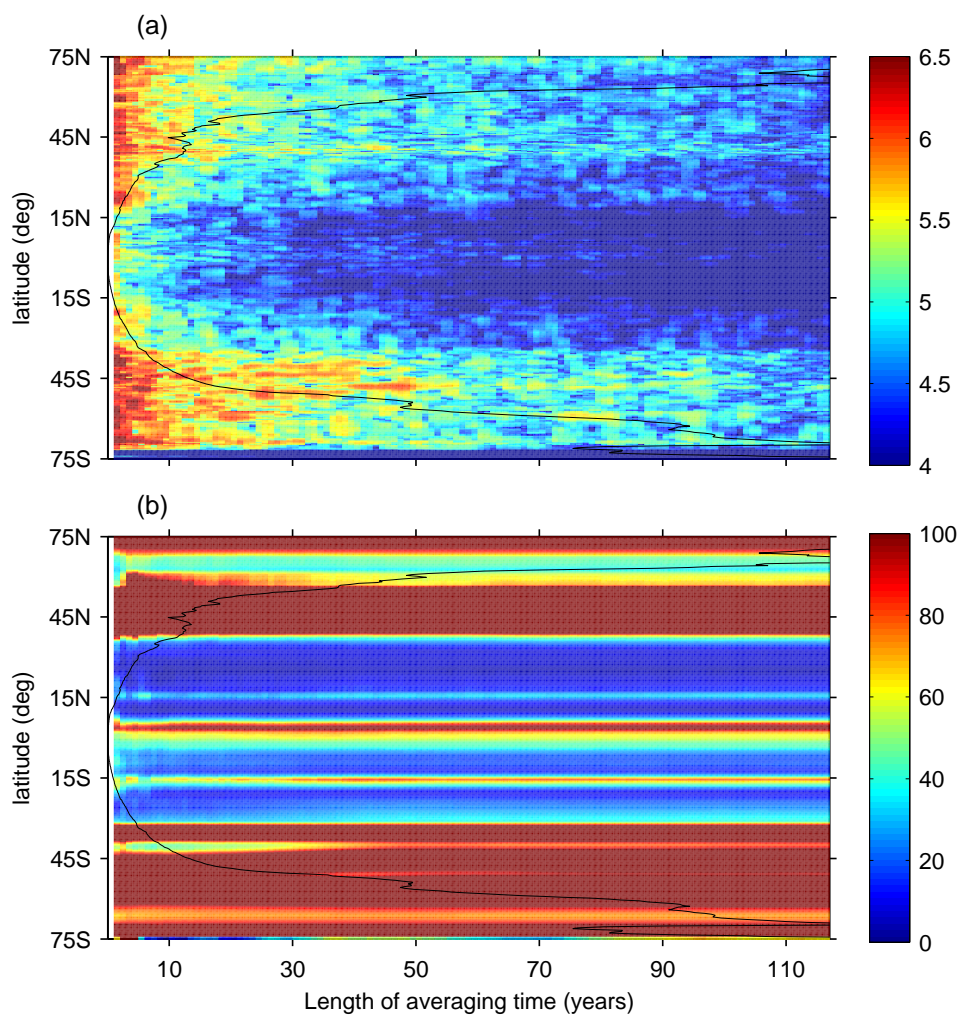


Figure 3.17: (a) The Sverdrup error fluctuation at every latitude of the subtropical Atlantic for averaging time periods of up to 120 years. The black line is the basin crossing time of a RW propagating at the non-dispersive limit according to the bottom pressure compensation theory of Tailleux and McWilliams (2001). (b) M_{zi} in the Atlantic calculated at different latitudes and for different amounts of time averaging. The black line is the basin crossing time of a RW propagating at the non-dispersive limit according to the bottom pressure compensation theory of Tailleux and McWilliams (2001). Units of (a) are $\log_{10}(\text{m}^3 \text{s}^{-1})$ and (b) are percentage.

if an AMOC reduction has already taken place over the last few decades (Bryden et al., 2005) then the upper ocean change must have occurred in the Antilles Current since no long term change has been reported in the Florida Straits Current (Meinen et al., 2010) or wind stress curl (Atkinson et al., 2010).

The model's southward interior ocean transport actually decreases in

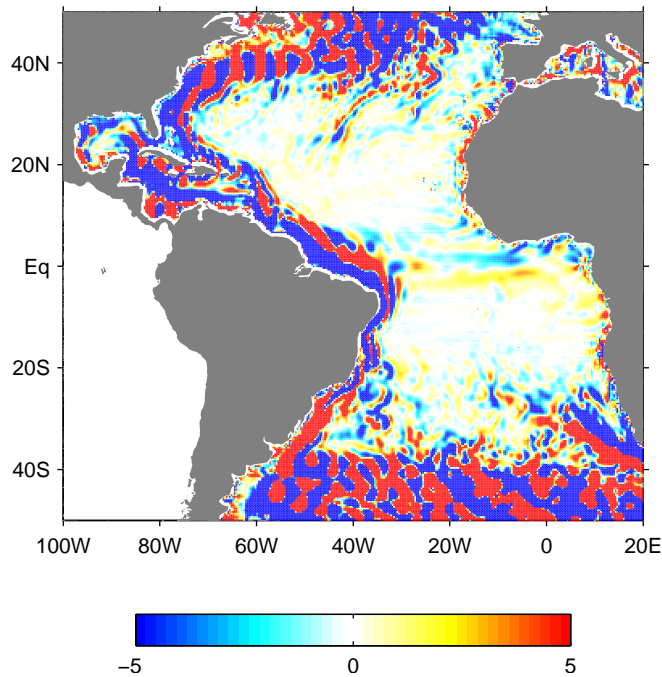


Figure 3.18: The 120 year time averaged Sverdrup error Δ_{SB} . The integration depth is 1500 m. Units are $\text{m}^2 \text{s}^{-1}$

strength by 3.0 Sv throughout the changing climate of the 2%CO₂ run. This is the result of weakening easterlies and westerlies that cause a reduced wind stress curl over the interior ocean (Figure 3.8). The outcome is an upper ocean western boundary current transport that is further reduced, by a total of 8.4 Sv. The reduction in interior ocean transport is a geostrophic transport change consistent with a climate change induced density reduction close to the eastern boundary (Figure 3.12). Both salinity and temperature changes play an important role in modifying the density.

Analysis of the transport changes in the North Pacific show a similar interior ocean response to Sverdrup transport changes (Figure 3.14). In the absence of a weakening deep transport, upper ocean western boundary transport reductions are due only to the decrease in wind stress curl. Conversely to the Atlantic, Pacific deep transports change from northwards to southwards. These changes act to partially offset the reduced upper ocean western boundary transport.

In this study the edge of the western boundary domain has been defined to lie east of all areas where Sverdrup balance clearly breaks down. At 27°N the largest reduction in upper ocean western boundary transport in our

climate change scenario occurs in the Antilles Current (Figure 3.11). This suggests that it is important to monitor both of the components of the upper ocean western boundary system at this latitude since they may contain water masses of different origin and may undergo different changes. This supports earlier findings that show the AMOC is carried mostly through the Florida Straits (Schmitz and Richardson, 1991) and the Antilles Current carries most of the gyre return flow (Lee et al., 1996).

The RAPID monitoring system at 26.5°N currently gives daily estimates of the depth structure of the meridional transport integrated across the whole Atlantic basin east of the Bahamas, and is providing valuable insight into the dynamics of AMOC variability. Our results suggest that for the purpose of monitoring change on the decadal time scale that it takes the interior ocean to adjust to Sverdrup balance, one could obtain useful supplementary information from the wind field.

Chapter 4

An Investigation into Subpolar Variability of the AMOC

4.1 Introduction

The Atlantic Meridional Overturning Circulation (AMOC) dominates the northwards heat transport in the Atlantic (Johns et al., 2011) and is an important contributor to the climate of North West Europe (Vellinga and Wood, 2002; Wood et al., 2003). Recent advances have made significant progress towards understanding the extent of temporal variability in AMOC strength (Kanzow et al., 2007; Cunningham et al., 2007). However, the strength of the AMOC is set by the strengths of many currents and processes whose individual contributions to AMOC variability are currently not well understood (Lozier, 2010; Kuhlbrodt et al., 2007). If a full understanding of possible future AMOC changes is to be gained then the spatial structure of its variability must first be understood.

The AMOC can be defined by a 2D stream function that describes a basin-wide net northwards flow of upper layer Atlantic water that is compensated by southwards flow in the deep ocean following buoyancy forced sinking at high latitudes. Buoyant tropical water gradually loses heat and moisture to the atmosphere as it flows northwards until its buoyancy is reduced enough for it to descend and mix into the deep ocean through, for example, vertical convective mixing and downwelling processes (e.g. Eden and Willebrand, 2001; Marotzke and Scott, 1999). Deep water subsequently flows southwards, eventually being brought back to the surface by Ekman

upwelling processes in e.g. the Southern Ocean (Toggweiler and Samuels, 1995) and by vertical mixing processes distributed throughout the ocean (e.g. Munk and Wunsch, 1998).

The spatial distribution of the currents that together make up the AMOC is complicated. In the upper subtropical ocean, the northwards flowing Gulf Stream (GS) splits into the southwards subtropical gyre (STG) circulation and the northwards North Atlantic Current (NAC). The NAC forms the eastern branch of the anti-clockwise flowing subpolar gyre (SPG), of which a part flows northwards across the Greenland-Scotland Ridge (GSR) into the Nordic Seas and a part remains in the SPG, flowing into and around the Irminger and Labrador seas. Along both of these pathways water increases in density through water mass transformation (WMT), sometimes until it is dense enough to convectively mix (Curry et al., 1998). The convectively formed water in the Nordic Seas eventually flows back into the SPG as dense overflow water primarily through the Denmark Straits (as Denmark Straits Overflow Water; DSOW). On exiting the Straits this exported dense water rapidly sinks into the deep ocean, entraining surrounding water as it does so (Dickson and Brown, 1994), then flows anti-clockwise around the Labrador Sea. Here it joins the convectively formed Labrador Sea Water and Irminger Sea Water which together co-source the Deep Western Boundary Current (DWBC). From the DWBC, deep water can then either recirculate back into or around the SPG (see Rhein et al., 2011, for a schematic summary of the current pathways; Figure 1.2b), or can be exported from the SPG southwards into the STG. Contrary to the traditional view that the DWBC is the dominant conduit of inter-gyre exchange, observations based on RAFOS floats have revealed that equatorwards pathways more commonly take an interior pathway offshore of the western boundary, starting near Flemish Cap (Bower et al., 2009). It is not yet fully understood what leads to the formation of the interior pathways, which contrast with the theory of deep circulation proposed by Stommel and Arons (1960), though there is evidence that eddies play an important role (Gary et al., 2011).

The intricate distribution of the currents, particularly in the subpolar gyre, is in part responsible for uncertainties that remain on the full nature of the AMOC. Furthermore, currents and processes in the North Atlantic are often inter-related, potentially complicating a diagnosis of the origin

of AMOC fluctuations. For example, Labrador Sea convection is thought to be related to the formation of dense deep water that feeds the DWBC (Bjastoch et al., 2008). It is thought also to lead to enhanced horizontal gradients (or doming) of isopycnals in the SPG that result in a spin up of the cyclonic currents of the SPG circulation (Häkkinen and Rhines, 2004; Böning et al., 2006). The strength of the cyclonic SPG circulation, indexed by what is known as the SPG strength, can subsequently mediate the cross-gyre exchange of water masses from the STG into the SPG and further into the Norwegian Seas (Hátún et al., 2005). The introduction of high salinity STG water into the Arctic leads ultimately to very dense water that, on re-entering the SPG via the straits of the DSR, can enhance the AMOC (Hátún et al., 2005). Variability of the AMOC that is due to western boundary variability may then be rapidly transmitted (within months) equatorwards along the western boundary as the ocean adjusts to forcing by Kelvin waves (e.g. Johnson and Marshall, 2002; Hodson and Sutton, 2012). Kelvin waves, on reaching the equator, subsequently propagate eastwards and then polewards along the eastern boundary where they excite westward propagating Rossby waves that bring about further AMOC adjustment on multi-year time scales (Zhai et al., 2011). AMOC fluctuations at any particular latitude are thereby influenced by variability occurring at higher latitudes.

Recent investigations using ocean models (Bingham et al., 2007) and observations (Lozier et al., 2010) have highlighted that AMOC variability does not occur coherently throughout the North Atlantic but is instead latitude dependent (de Boer, 2010). The most pronounced of the latitude differences lies between the variability of the SPG and STG. This is perhaps unsurprising given the complicated adjustment (Bingham et al., 2007) and transport pathways (Bower et al., 2009; Rhein et al., 2011) that take place both within and between the gyres of the North Atlantic, as described above. However, the first mode Empirical Orthogonal Function (EOF) of inter-annually filtered AMOC reveals that variability is dominated by an underlying meridionally coherent stream function (Bingham et al., 2007).

Studies that have revealed the latitude dependent nature of AMOC variability have generally been done according to an AMOC defined with depth as the vertical coordinate. The AMOC may also be calculated using den-

sity as a vertical coordinate (see section 4.3 below), a representation that may better capture the processes involved in overturning (Mauritzen and Häkkinen, 1999; Zhang, 2010; Bailey et al., 2005). Calculations of the AMOC in density space in a coarse resolution ocean model reveal that AMOC variability is meridionally coherent when calculations are made in density space and appropriate adjustment time scales are accounted for at each latitude (Zhang, 2010). It is possible, however, that real ocean (or high resolution model) variability is more complicated than can be captured in a coarse resolution model due to effects from eddies, particularly at high latitudes (Biaostoch et al., 2008), and because Kelvin wave speeds become more realistic in higher resolution models (e.g. Hodson and Sutton, 2012).

It is now understood that the AMOC undergoes large fluctuations on weekly to inter-annual time scales (Cunningham et al., 2007; McCarthy et al., 2012), and general circulation models display large amplitude AMOC variability on timescales of up to multi-decadal in period (e.g. Hodson and Sutton, 2012). There is evidence that much of the oceanic variability arises as a result of atmospheric fluctuations and much work has been done to link the two. For example, the sensible and latent heat lost from the ocean due to the colder temperatures and strong winds of the higher latitudes can prime the ocean for convective mixing (e.g. Eden and Willebrand, 2001). Also, the strength of the wind stress can affect the AMOC by Ekman transport changes and (along with its curl; Häkkinen et al., 2011) by modifying the shape and strength of the SPG (Hátún et al., 2005). Long timescale variability in particular has been linked to the North Atlantic Oscillation (e.g. Eden and Willebrand, 2001; Medhaug et al., 2011) and internal ocean feedbacks that respond to sustained phases of the North Atlantic Oscillation (Lohmann et al., 2009).

Compared to the atmospheric origins of AMOC variability, how regional changes in ocean variability are related to changes in the AMOC is poorly understood (Lozier, 2010). The strength of the AMOC has been shown to correlate with changes in the strength of the flow through the Denmark Straits (Gregory et al., 2005; Köhl and Stammer, 2008), to the strength of Labrador Sea convective mixing (Biaostoch et al., 2008; Latif et al., 2006), and to the SPG strength (Häkkinen and Rhines, 2004). However, the contributions of these different currents and processes to the different time scales

of AMOC variability as represented in different coordinate representations of the AMOC is not well known. Using a 120 year control run from the eddy permitting coupled model HiGEM, this chapter aims to explore the relationship between the AMOC and the localised strength of ocean currents and mixing processes on different time scales, with a particular emphasis on subpolar latitudes where deep water is formed and introduced into the North Atlantic. This is done using both depth and density space definitions of overturning to determine where and how they differ and what the implications are for the differences. The meridional coherence of AMOC variability is also investigated, building upon previous work done that has used observations (Lozier et al., 2010) and coarse resolution models (Zhang, 2010; Bingham et al., 2007).

In the next section details of the model, HiGEM, are provided. In section 4.3 the depth and density space overturning are defined and described. The variability of the model overturning is described in Section 4.4, followed by an analysis in section 4.5 of how meridionally coherent the AMOC variability is on different time scales. Section 4.6 addresses the differences between depth and density space overturning and the role of regional processes on their variability. In section 4.7 the mechanisms by which ocean processes affect the AMOC are described. The final section draws up the main conclusions.

4.2 Model Description

In this chapter data is used from the coupled climate model, HiGEM (Shafrey et al., 2009), which uses a spherical lat-lon grid between 90°S and 90°N. HiGEM is based on the Met Office HadGEM1 model (Johns et al., 2006) but uses a higher horizontal resolution of 0.83° latitude \times 1° longitude in the atmosphere and an eddy permitting 1/3° \times 1/3° resolution ocean. HiGEM also has a higher vertical resolution, with 40 vertical levels in the ocean and 38 vertical levels in the atmosphere, each unevenly spaced to allow higher surface boundary layer resolution. Initial conditions are from the World Ocean Atlas 2001 for the ocean and ECMWF analysis for the atmosphere. The eddy permitting resolution of HiGEM is considered important in this study because of the significant role of eddies in setting

high latitude AMOC variability (Bjastoch et al., 2008), and because of the improved representation of Kelvin Waves that mediate ocean adjustment to western boundary perturbations (e.g. Hodson and Sutton, 2012). Annual mean output is used from a 150 year control integration in which greenhouse gases are kept constant at present day concentrations. The most significant initial adjustments take place over approximately the first 30 years and is therefore discarded. Henceforth year 1 refers to the 31st year of the control simulation.

4.3 Coordinate representations of the AMOC

The AMOC is defined as a two dimensional stream function in depth ($\psi_z(y, z)$) and density ($\psi_\sigma(y, \sigma)$) space coordinates, respectively written,

$$\psi_z = \int_z^0 \int_{x_{east}}^{x_{west}} v_z dx dz, \quad (16)$$

$$\psi_\sigma = \int_\sigma^0 \int_{x_{east}}^{x_{west}} v_\sigma dx d\sigma, \quad (17)$$

where σ is the potential density, v_z is the meridional velocity at Cartesian location (x, y, z) and v_σ is the meridional velocity at density coordinate location (x, y, σ) . Horizontal integration limits are from the eastern (x_{east}) and western (x_{west}) boundaries. Note that v_z is output as annual averages at fixed depths, so an interpolation onto density surfaces will potentially introduce some error in v_σ . In each case, the zonally integrated meridional flow follows streamlines clockwise around positive values and vice-versa. Throughout this chapter investigations are limited to between latitudes 33°S (the southern tip of the African continent) and 65°N. South of 33°S the calculation of overturning breaks down due to the unboundedness of the Atlantic, and north of the Denmark Straits at 65°N the overturning is small (Figure 4.1a and Figure 4.2a).

The two representations of overturning can differ for two reasons, because water masses at the same depth do not necessarily have the same density and because sinking water masses do not necessarily change in density. There are three possible types of overturning, which are due to: 1) Vertical layers of opposing net meridional transports with different densities. This contributes equally to ψ_z and ψ_σ . 2) Opposing meridional transports of

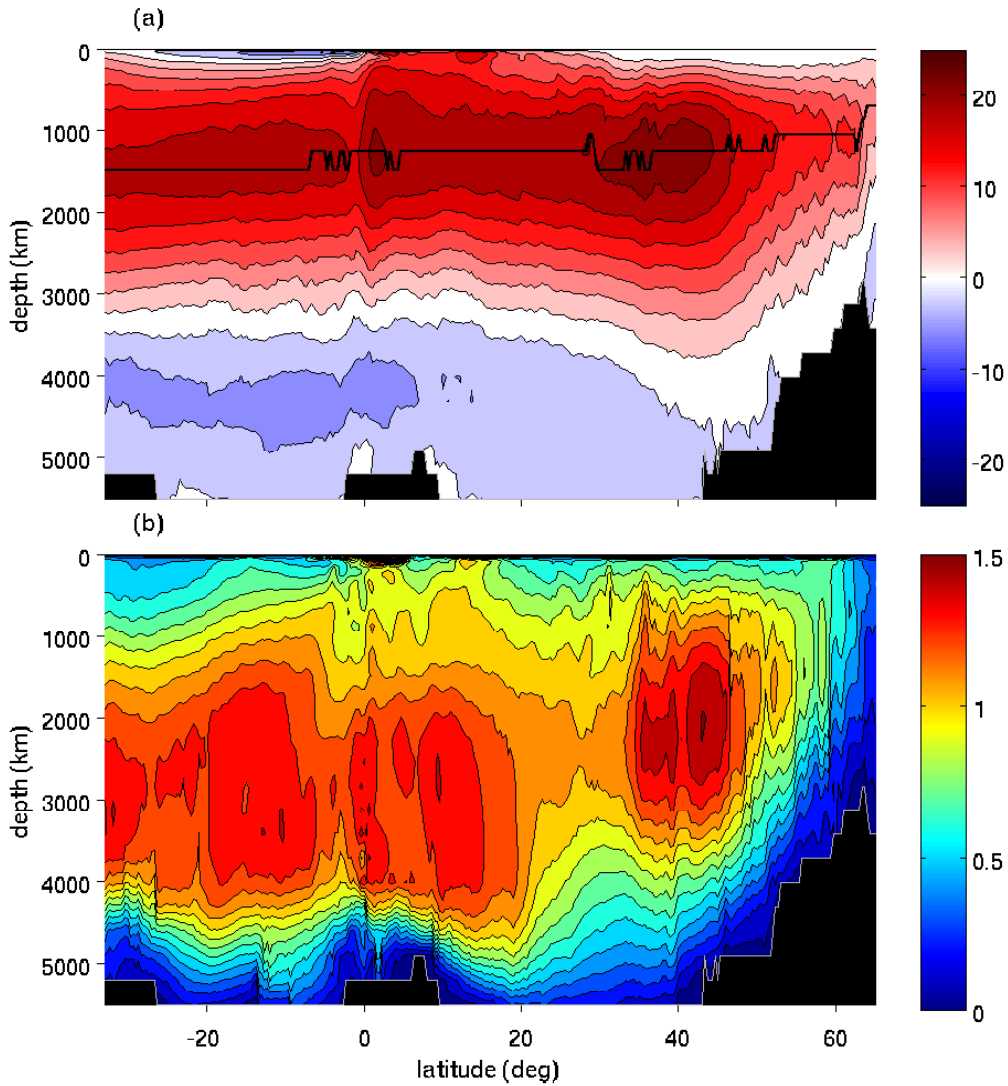


Figure 4.1: (a) 120 year mean depth-space Atlantic overturning stream function, ψ_z and (b) its temporal standard deviation from annual averages. The black line indicates the depth of maximum overturning at each latitude. Black shading shows the maximum depth of topography. Units are Sverdrups (Sv; $10^6 \text{ m}^3 \text{ s}^{-1}$). Contour intervals are (a) 3 Sv and (b) 0.1 Sv.

different density that are at the same depth. This contributes only to ψ_σ (Zhang, 2010). 3) Opposing meridional transports of the same density that are at different depths. This contributes only to ψ_z (Döös and Webb, 1994).

The 120 year time mean ψ_z is shown in Figure 4.1(a). The zonal-mean meridional flow is northwards above approximately 1500 m depth everywhere in the Atlantic up to latitudes of approximately 40°N when the zonal-mean flow begins to sink. Water returns southwards at depths between approximately 1500 m and 3000 m. Below this, Antarctic Bottom

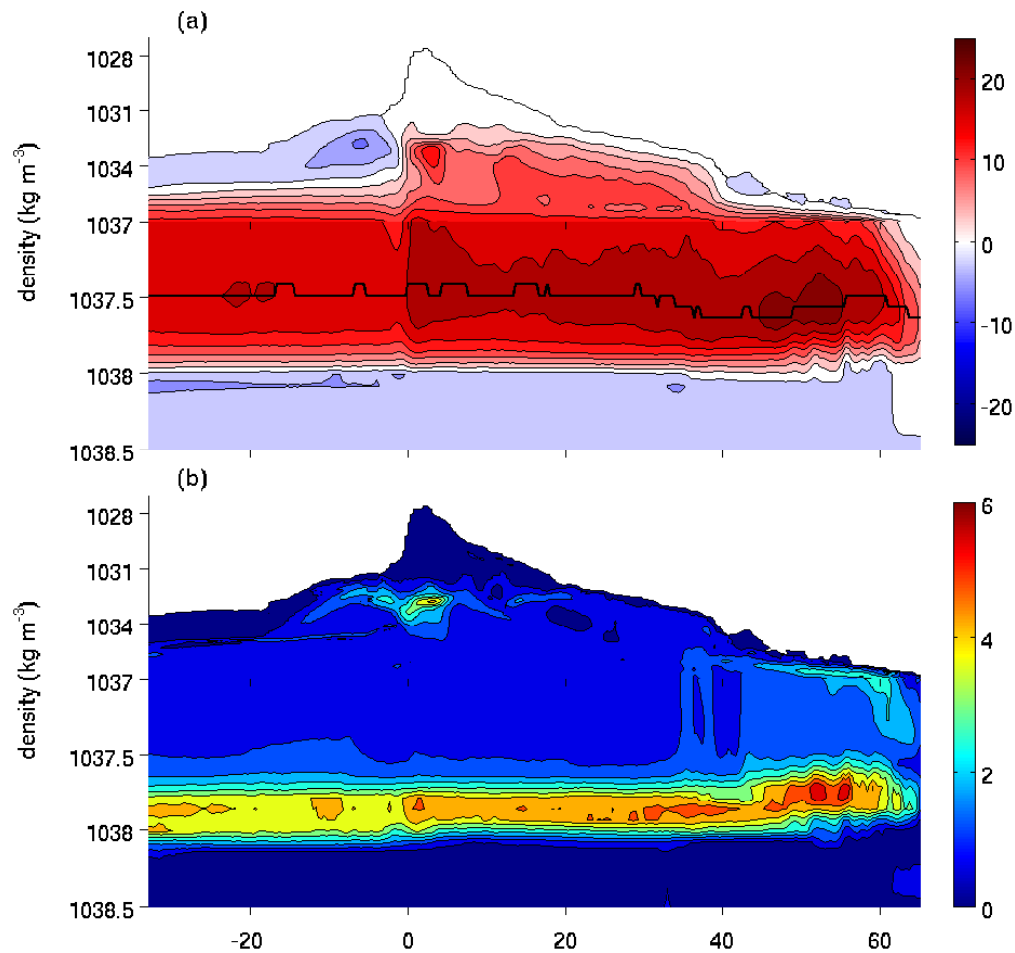


Figure 4.2: (a) 120 year mean Density-space Atlantic overturning stream function, ψ_σ and (b) its temporal standard deviation from annual averages. The black line indicates the depth of maximum overturning at each latitude. Note the change in y-axis scale at 1037 kg m⁻³. Units are Sv. Contour intervals are (a) 3 Sv and (b) 0.6 Sv.

Water forms an anti-clockwise overturning cell. The maximum ψ_z is located between latitudes 30°N and 45°N and peaks at about 25 Sv. The standard deviation of the 120 year ψ_z time series is approximately 1.2 Sv (peaking at approximately 1.5 Sv at 45°N; Figure 4.1b). The highest standard deviations lie on the northern and deep edges of the clockwise cell, indicating that most of the variability arises from temporal changes to the spatial extent of the overturning. This may be because of changes in the location of vertical convective mixing and the densities of the deep water that is formed; a meridional change in the dominant region of convection would change the location of the northern limb of the overturning cell, while

the density of the water would affect the depth of the southward flow. It has been verified that the high standard deviations are not due to any trends resulting from model spin up. Blaker et al. (2012) also find that the location of maximum AMOC variability is located at greater depths than the maximum AMOC within a global $1/4^\circ$ resolution configuration of the NEMO model.

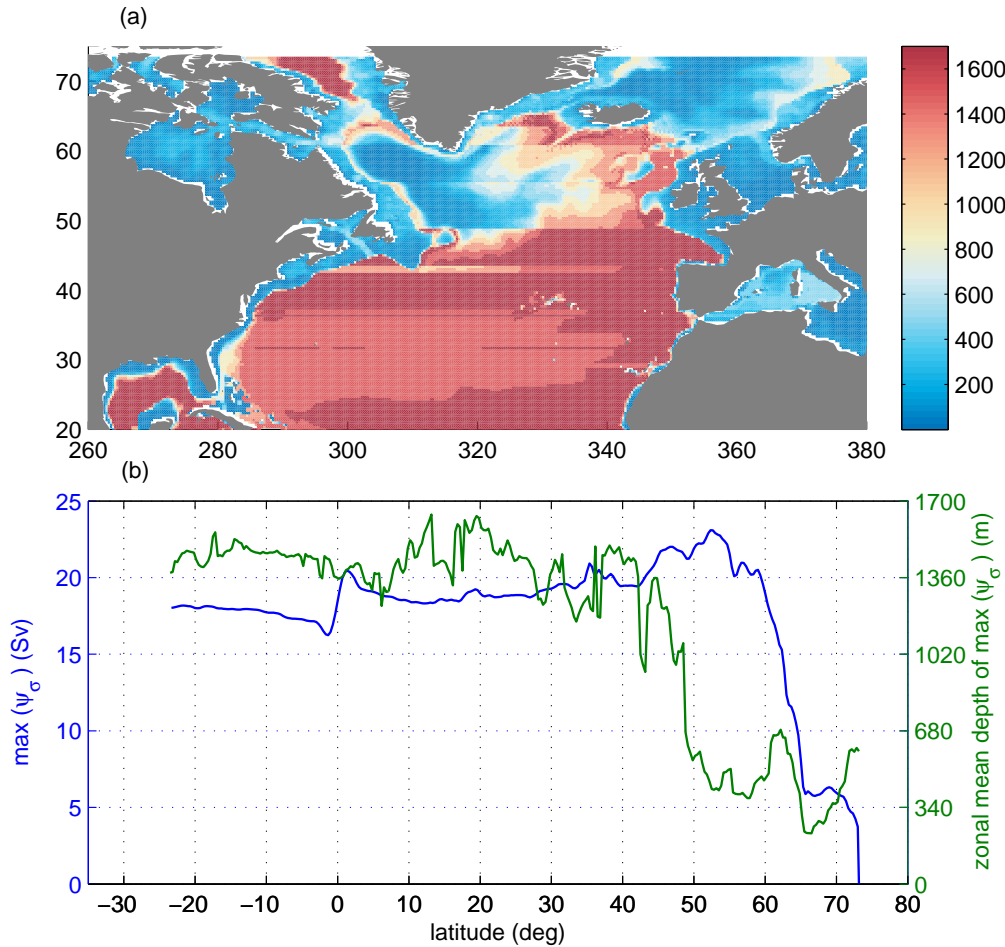


Figure 4.3: (a) The depth of the isopycnal of maximum ψ_σ (black line in Figure 4.2) in units of m. (b) The maximum ψ_σ (blue line) and the zonal mean depth of the isopycnal of maximum ψ_σ (green line) at each latitude.

The stream function of the 120 year time-mean ψ_σ is shown in Figure 4.2(a). As with ψ_z , the zonal-mean flow in density space follows streamlines clockwise around positive streamfunction contours. Water mass transformation is evident as upper ocean water flows northwards from the South Atlantic, gradually decreasing in density as it enters the tropics and then increasing again as it exits the tropics. At approximately 55°N densities

rapidly increase, likely because of significant buoyancy loss to the atmosphere during circulation around the SPG (Mauritzen and Häkkinen, 1999) and because of the introduction of water from the Nordic Seas. The maximum ψ_σ occurs between latitudes 45°N and 55°N, peaking at about 25 Sv. Locations of the maximum depth space and density space overturning in HiGEM are in agreement with estimates from other general circulation models (e.g. Langehaug, 2011; Zhang, 2010; Bailey et al., 2005). The anti-clockwise cell of Antarctic Bottom Water is evident within a narrow range of densities in ψ_σ . As with ψ_z most of the variability lies on the northern and dense edges of the clockwise circulation cell, suggesting the dominant variability might be from fluctuations in the spatial extent of the cell that arise due to variations in water density following WMT. The variability of ψ_σ is much larger than ψ_z , peaking at approximately 5 Sv. The higher variability of ψ_σ must be related to transport cancellation that occurs in either depth space or density space overturning.

The maximum overturning is consistently located at approximately 1100 m depth and 1037.5 kg m⁻³ throughout the Atlantic for ψ_z and ψ_σ respectively (bold black lines in Figure 4.1a and Figure 4.2a). For comparison to the approximately constant 1100 m depth of ψ_z we determine the depth of maximum ψ_σ , which is determined at each latitude and longitude position (Figure 4.3a). Contrary to the near-constant depth of maximum ψ_z , the depth of the maximum ψ_σ has a strong meridional dependence. Throughout the subtropics the maximum ψ_σ is located at approximately 1300 m depth, but there is a sharp transition into the western SPG where the depths are much shallower. This boundary is located approximately where the Gulf Stream forms a zonal jet in HiGEM. The transition of maximum ψ_σ from the STG to SPG is well demonstrated by Figure 4.3(b) which shows the time-mean maximum ψ_σ and the time-mean zonal average depth of maximum ψ_σ . The largest density space overturning strength in the Atlantic occurs in the SPG, and takes place on average at about 500 m depth. South of the SPG the maximum ψ_σ weakens and deepens. The isopycnal of maximum ψ_σ is generally shallower than 200 m depth in the western SPG, then steadily increases in depth towards the eastern boundary where the maximum ψ_σ everywhere lies deeper than 1000 m depth. The horizontal pattern of the isopycnal depth of maximum ψ_σ (Figure 4.3) demonstrates a link between the waters

of the STG and the eastern SPG. This agrees well with the current understanding that the eastern SPG acts as a conduit for exchange between the STG, SPG and Arctic Ocean (Hátún et al., 2005; Häkkinen et al., 2011).

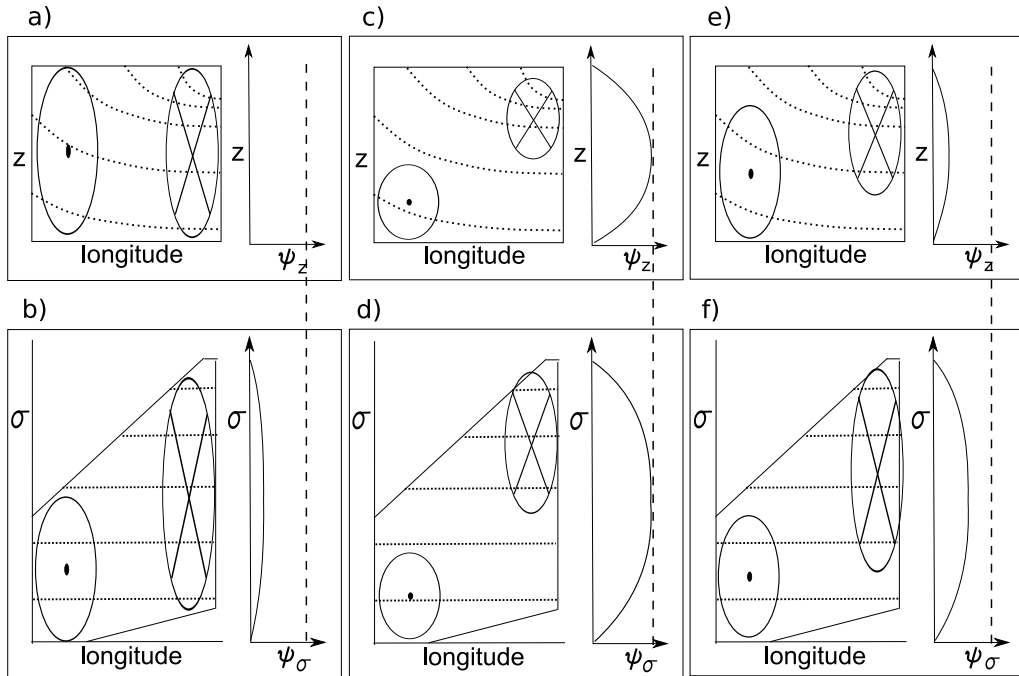


Figure 4.4: Idealised representation of the (a,c,e) depth space and (b,d,f) density space distribution of transports and corresponding ψ through a cross section of the SPG for three different scenarios. In each scenario, all northwards transports are in the east and all southwards transports are in the west. (a,b) Scenario 1) the transports are barotropic. (c,d) Scenario 2) all northwards transports occur at shallower depths than the southwards transports. (e,f) Scenario 3) the northwards transports occur in an upper layer and southwards transports in a lower layer, but they share a mid-depth range. Dotted lines represent isopycnals. Arrows into and out of the page represent northwards and southwards transports respectively, and each arrow represents the same transport strength. The vertical dashed lines represent the maximum overturning possible from these transports.

A description of how the isopycnal of maximum overturning can be located at such shallow depths in ψ_σ might be explained by zonally integrating along density contours that are sloped upwards across the SPG. Figure 4.4 schematically represents the overturning associated with three different idealised transport cross sections through a subpolar gyre with vertical boundaries. In each scenario, all northwards transports occur in the eastern basin and southwards transports occur in the western basin. For ease of comparison the transport arrows in each scenario each represent

the same area-integrated transport. Each figure panel shows the transport cross section and corresponding overturning stream function, ψ . In the first scenario (Figure 4.4a,b) the transports are barotropic and so cancel out in depth space. In density space, however, the higher densities of the southwards transports ensure that only part of the transports cancel out in the zonal integral such that there is a small overturning present. In the second scenario (Figure 4.4c,d) all the southwards transports are contained at greater depths than the northwards transports. In this case no cancellation occurs in either depth or density space so the maximum possible overturning occurs in both. In the third scenario (Figure 4.4e,f) northwards and southwards transports are contained within the upper and lower water column respectively, but such that they share a mid-depth range in ψ_z and also a mid-density range in ψ_σ . While some cancellation occurs in both coordinate spaces in this scenario, more cancellation of transports takes place in ψ_z such that there is more overturning in ψ_σ . The third scenario is expected to be the most representative of the real ocean.

As with the idealised transports of Figure 4.4, the presence of higher density waters (introduced from higher latitudes or through WMT) in the surface waters of the SPG can lead to zonal density gradients and to ψ_σ . This may explain why the isopycnal of maximum ψ_σ is located close to the surface in the western SPG. As represented in Figure 4.4(d,f), the maximum ψ_σ might be positioned on an isopycnal that is shallow in the western basin, but the largest transports are not necessarily positioned near the surface.

4.4 Variability of the AMOC

For the purposes of investigating AMOC variability it is more useful to study the maximum of the overturning stream function. The maximum AMOC is calculated as the maximum stream function between depths 500 m and 2500 m for ψ_z , and between 1037.5 kg m^{-3} and 1038.5 kg m^{-3} for ψ_σ . These depths and density ranges ensure only the clockwise streamlines are considered. Hereafter any reference to maximum ψ_z and ψ_σ will be respectively referred to as Ψ_z and Ψ_σ , and which will be the main focus throughout the remainder of the chapter. The term overturning henceforth carries a general meaning of AMOC stream function in either depth or density space

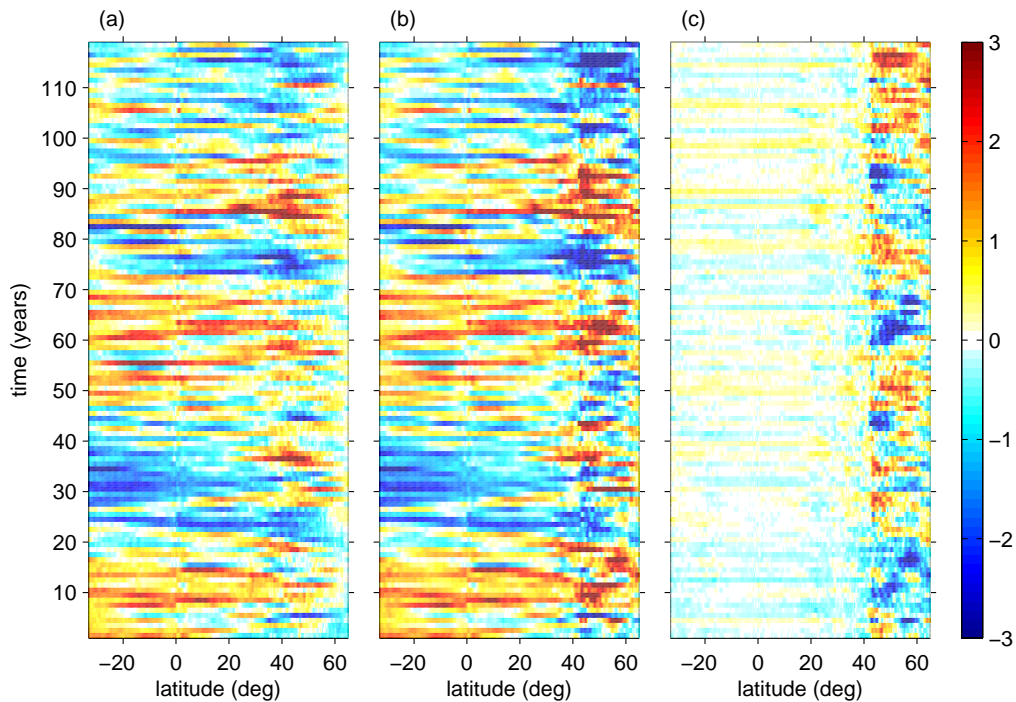


Figure 4.5: Hovmöller plots of (a) Ψ_z , (b) Ψ_σ and (c) their difference (Ψ_z minus Ψ_σ). The latitude-dependent time-mean is removed in each case to give the anomaly. Units are Sv.

coordinates.

Time series of Ψ_z and Ψ_σ are displayed as latitude-versus-time (Hovmöller) plots, plotted as anomalies from the latitude dependent time-mean (Figure 4.5a,b). The difference, Ψ_z minus Ψ_σ , is plotted in Figure 4.5(c). Similar variability is displayed by Ψ_z and Ψ_σ at all latitudes between 33°S and approximately 40°N. At these latitudes almost all overturning is therefore due to stratified layers of opposing water masses (see section 4.3). There is a strong demarcation at 40°N, north of which Ψ_σ displays different variability to Ψ_z and has stronger variability. The sharp change in the depth of maximum overturning is also located at approximately 40°N and coincides with the location of the Gulf Stream zonal extension. It is suggested here that 40°N marks a transition into a subpolar circulation regime in which Ψ_σ is dominated by opposing meridional transports of differing density that occur at the same depth. Such transports therefore contribute to Ψ_σ but not to Ψ_z (see section 4.3). This also explains why the latitude of maximum Ψ_σ (Figure 4.2) is located further north than the latitude of maximum Ψ_z (Figure 4.1). Because of the relatively weak subpolar Ψ_z variability, overturning

due to sinking water masses of equal density (which contributes only to Ψ_z ; see section 4.3) is suggested to be small.

The transition at 40°N is brought about by a southwards flattening out of the horizontal density gradients in the SPG as isopycnals in the western basin deepen under the Gulf Stream. While the 40°N demarcation appears in both Ψ_z and Ψ_σ , it is substantially more pronounced in the latter. Since Bingham et al. (2007) reveal a strong demarcation at approximately 40°N in Ψ_z containing seasonal variability, it can be suggested that the variability responsible for the demarcation occurs at shorter periods than the annual periods used in this chapter. The major focus for the remainder of this chapter is on Ψ_σ variability and the processes that are responsible for its differences to Ψ_z variability.

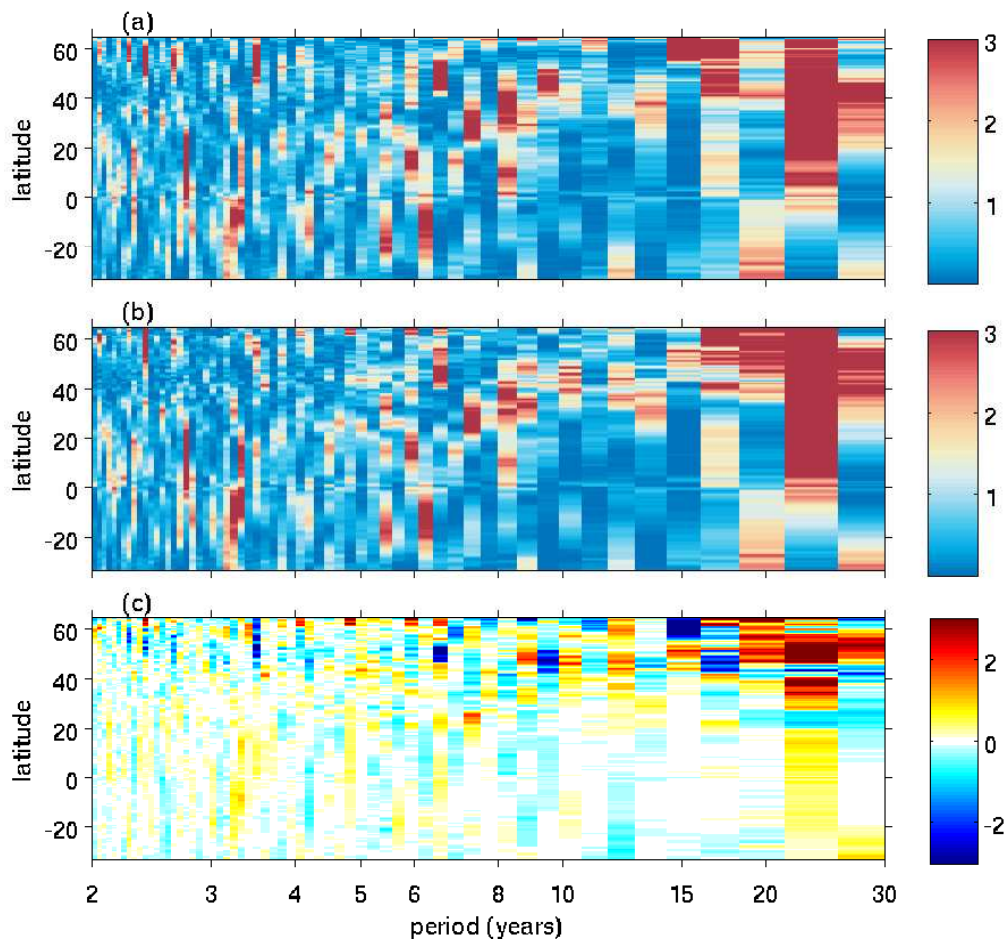


Figure 4.6: Latitude dependent periodogram of (a) Ψ_z , (b) Ψ_σ and (c) their difference (Ψ_z minus Ψ_σ). Units are $(\text{Sv})^2$.

Variability in both Ψ_z and Ψ_σ visibly contain a broad band of frequencies

up to decadal and longer in period (Figure 4.5). Applying a Fourier transform to the latitude-time plots enables the variability to be decomposed into the contributing frequencies (the spectra) or periods (periodogram; the reciprocal of the spectra). Periodograms of Ψ_z and Ψ_σ , calculated at each latitude for periods up to 30 years, exemplify the broad band of frequencies contained in overturning variability (Figure 4.6a,b). Periods beyond 30 years are not shown since their accuracy in a 120 year time series is difficult to defend. The difference between the periodograms (Ψ_z minus Ψ_σ ; Figure 4.6c) supports the findings from Figure 4.5 that the main differences between Ψ_z and Ψ_σ are mostly located at high latitudes. Differences, however, are seen at many periods and so cannot be attributed to any single process with a particular frequency.

To better understand the contributions from the relative high and low frequency components of overturning variability, the Hovmöller plots of Ψ_z and Ψ_σ are high pass and low pass filtered at a period of 5 years (Figure 4.7). This separates the variability into 2 components, containing periods greater and less than 5 years. This filtering is achieved by applying an inverse Fourier transform to the periodograms (Figure 4.6) with all undesired periods set to zero. A threshold of 5 years is chosen since it retains a large number of spectral bins in both the high and low frequency components and it approximately separates inter-annual variability from decadal variability. As with the unfiltered Hovmöller plots (Figure 4.5), 40°N stands out as a threshold in both the high and low pass filtered AMOC variability at which ψ_z and ψ_σ variability are similar to the south and different to the north.

The magnitudes of the filtered components of AMOC variability are determined by calculating the temporal standard deviation at each latitude. North of 20°N the magnitude of the low pass filtered overturning variability is larger than the high pass filtered overturning variability, up to approximately 50°N for Ψ_z and 60°N for Ψ_σ where, in each case, the high pass and low pass filtered overturning become of a similar magnitude (Figure 4.8). Throughout subtropical latitudes Ψ_z and Ψ_σ display similar magnitude variability, but in subpolar latitudes both the high frequency and low frequency variability of Ψ_σ is larger than that of Ψ_z . The variability of the low pass filtered Ψ_σ in the SPG is significantly larger than the other components of Ψ_z and Ψ_σ . High and low pass filtered overturning at 5 year

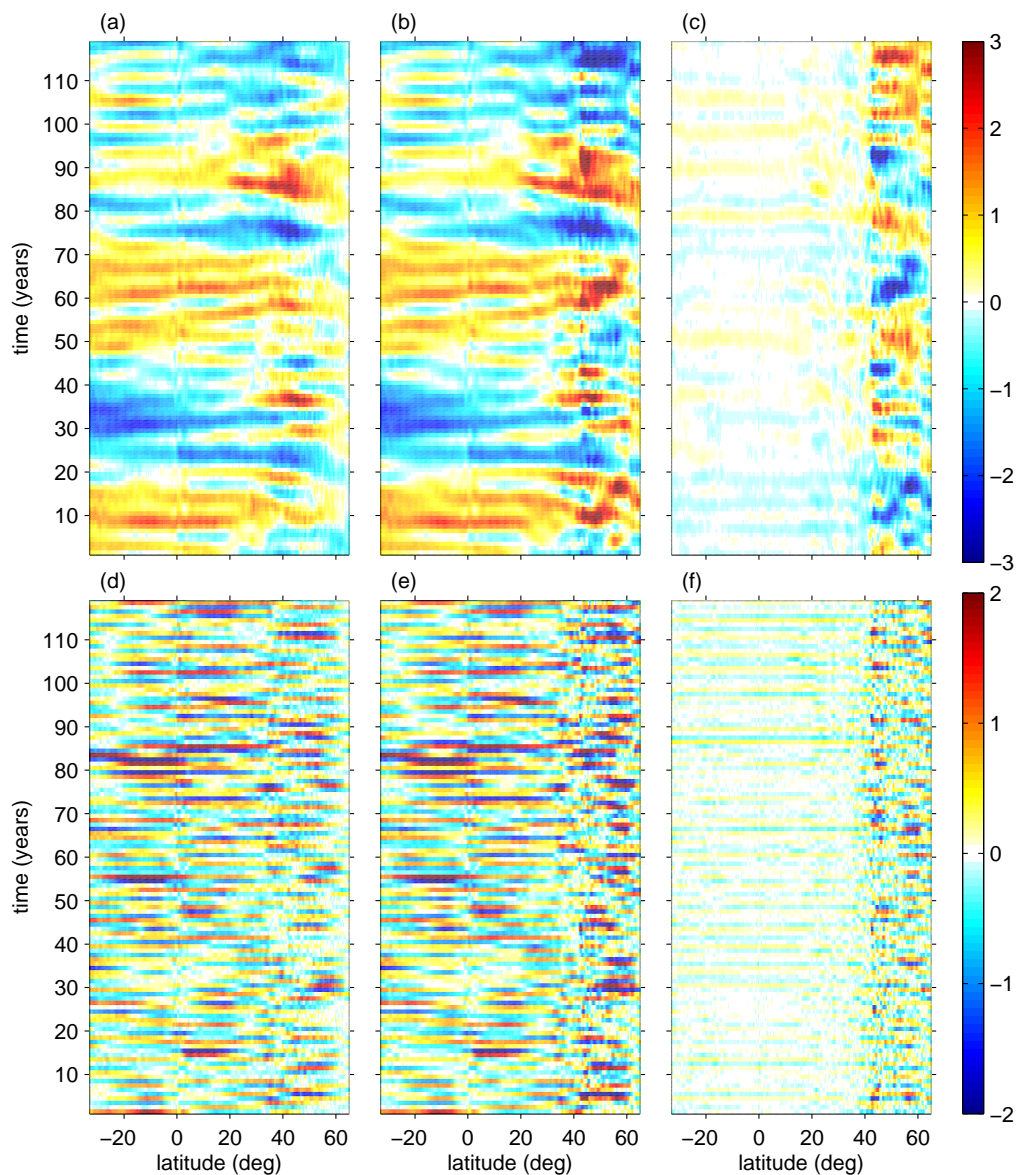


Figure 4.7: Latitude versus time plots of 5 year (a-c) lowpass and (d-f) highpass filtered (a,d) Ψ_z , (b,e) Ψ_σ and (c,f) their difference (Ψ_z minus Ψ_σ). The latitude-dependent time-mean is removed in each case to give the anomaly. Units are Sv.

period will hereon be referred to as $\Psi_{z,lp}$ and $\Psi_{z,lp}$ respectively in depth space, and $\Psi_{\sigma,lp}$ and $\Psi_{\sigma,lp}$ in density space.

4.5 Meridional coherence of the AMOC

This section addresses the latitude dependence of overturning variability. As discussed in other modelling studies (Bingham et al., 2007; Lozier et al.,

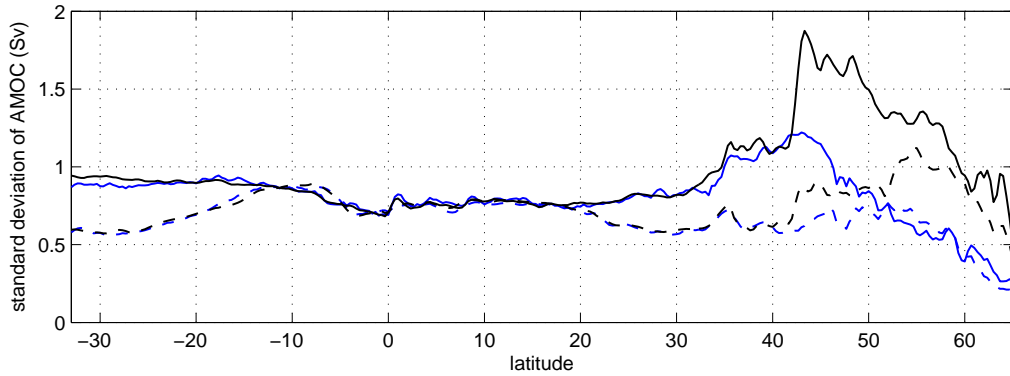


Figure 4.8: Temporal standard deviation of $\Psi_{z,lp}$ (blue solid), $\Psi_{z,hp}$ (blue dashed), $\Psi_{\sigma,lp}$ (black solid) and $\Psi_{\sigma,hp}$ (black dashed) at each latitude. Units are Sv.

2010), the discontinuity between SPG and STG overturning variability in HiGEM raises the question of how coherent the variability is between latitudes to the north and south of 40°N . Using a low resolution coupled general circulation model, GFDL CM2.1, Zhang (2010) showed that subpolar and subtropical Ψ_σ variability are meridionally coherent when calculated in density space and when the propagation time of Ψ_σ anomalies, from high to low latitudes, is accounted for. Using the same methodology we extend the study using HiGEM, which is a higher resolution model than that used by Zhang (2010) and so may capture potentially important smaller scale processes. Lagged correlations are calculated between overturning at 50°N and overturning at all latitudes (Figure 4.9a-d). Lagged correlations are the correlation between two variables at all possible lag shifts relative to each other.

Lagged correlations of Ψ_z referenced to 50°N show a continuous band of positive correlation from high to low latitudes, thereby demonstrating southwards propagation of Ψ_z variability between the gyres (Figure 4.9a). Correlations at latitudes south of approximately 20°N are less than 95% significant (calculated according to the method outlined in appendix 6.3.2), but the band of positive correlation that persists continuously throughout the Atlantic lends credence to the existence of propagating meridional Ψ_z anomalies. Given the few years of adjustment timescale, the southwards propagation is likely due to advected water masses. The meridional coherence is slightly stronger in Ψ_σ than in Ψ_z (Figure 4.9c), for which 95% significant correlations persist down to the equator. This may be because

southwards moving water masses that pass from subpolar to subtropical latitudes are not contributing to Ψ_z in the subpolar gyre because of zonal cancellation with other northwards moving water masses, but are contributing to Ψ_σ . Meridional coherence would therefore be expected to improve in density space. Lagged correlations of Ψ_σ in HiGEM, however, are poorer than those determined by Zhang (2010) from the coarse resolution model. This may be due to better resolved small scale variability in HiGEM that partially masks meridional overturning adjustment. Lagged correlations of $\Psi_{z,lp}$ (Figure 4.9b) and $\Psi_{\sigma,lp}$ (Figure 4.9d) are larger and show more pronounced meridional coherence than in lagged correlations of their unfiltered counterparts. This indicates that high frequency variability plays an important role for the latitude differences seen in overturning anomalies.

The meridional coherence on 5 year and longer time scales indicates that the RAPID array (Kanzow et al., 2007) may be used to determine overturning variability at high latitudes. Note, however, that if 55°N is used as the reference latitude instead of 50°N in lagged correlations of maximum overturning (Figure 4.9e-h) then changes are brought about in the meridional coherence of Ψ_σ and $\Psi_{\sigma,lp}$ (Figure 4.9c,d,g,h). Although their variability remains coherent from high to low latitudes, correlations with subtropical latitudes are weakened and the meridional band of correlation is less distinct. Using the higher reference latitude with Ψ_z , however, brings about relatively little change in comparison to when 50°N is used (Figure 4.9a,b,e,f). The implication is that, while Ψ_σ is more coherent than Ψ_z across the 40°N gyre boundary, Ψ_σ is less meridionally coherent than Ψ_z within subtropical latitudes. Such differences in subpolar $\Psi_{\sigma,lp}$ from one latitude to another are indicated in the Hovmöller plot of $\Psi_{\sigma,lp}$ (Figure 4.5b) by features that appear to propagate northwards rather than southwards (when sloping bands are diagonally oriented from bottom left to top right). Further work is required to understand the intra-gyre differences of subpolar Ψ_σ variability.

Using hydrographic data Lozier et al. (2010) showed that ψ_z increased in strength by 0.8 ± 0.5 Sv in the subpolar gyre and decreased by 1.5 ± 1.0 Sv in the subtropical gyre between two twenty year averaged periods, 1950-1970 and 1980-2000. It was concluded therefore that overturning variability might not be meridionally coherent but is either undergoing different (or

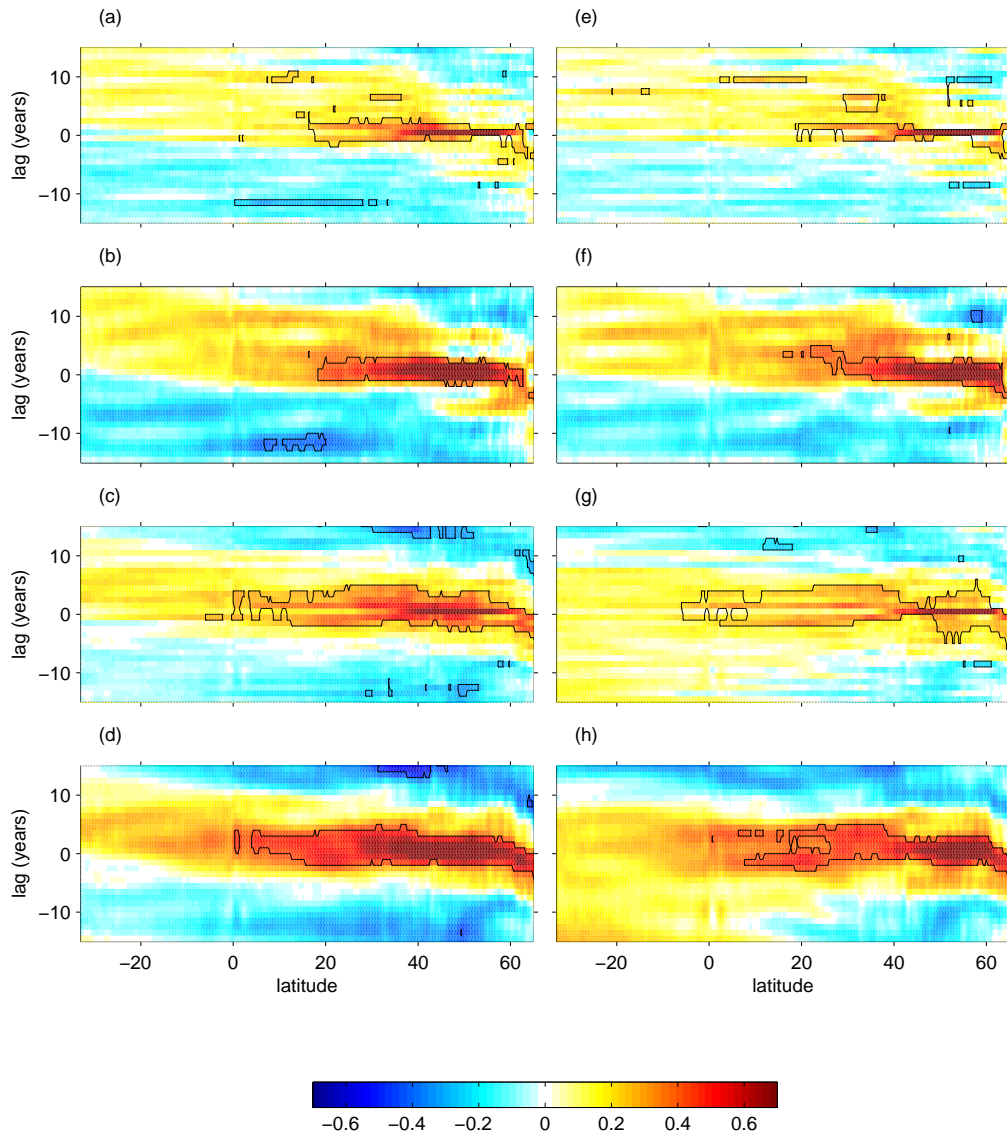


Figure 4.9: Lagged correlations of maximum overturning referenced to (a-d) 50°N and (e-h) 55°N for (a,e) Ψ_z , (b,f) $\Psi_{z,lp}$, (c,g) Ψ_σ and (d,h) $\Psi_{\sigma,lp}$. The latitude independent variable leads at positive lag. Black contours represent the 95% confidence interval. Correlation coefficients given in normalised units.

opposing) cycles within the two gyres or is displaying opposing climate trends. The results presented here suggest that Ψ_z variability, on time scales of 5 years and more, is coherent throughout the North Atlantic, but only when appropriate lag shifts are accounted for (Figure 4.9). It is possible therefore that the overturning changes reported by Lozier et al. (2010) are a result of unaccounted for phase differences between the variability occurring in the subpolar and subtropical gyres.

Figure 4.10 plots the difference between two time-means of ψ_z calculated during years 25-45 and 55-75 (Figure 4.10). The method is similar to that used by Lozier et al. (2010). These two twenty year periods coincide with periods of persistently low and high ψ_z anomalies within the STG (Figure 4.5), so that a positive ψ_z change takes place in the STG between the two periods. Within subpolar latitudes the decadal mean is influenced by positive overturning anomalies during the later part of the period 25-45 years, and by negative anomalies during the later part of the period 55-75 years, such that a negative ψ_z change takes place in the subpolar gyre. Similar results are obtained if the two twenty year periods are shifted (in the same direction) by up to ± 5 years. The Lozier et al. (2010) results might therefore be explained by natural variability rather than being due to any trends. Further, since much of the Ψ_z variability is found to be meridionally coherent in HiGEM, the (Lozier et al., 2010) results might also reflect that a single propagating decadal period AMOC anomaly is included to a different extent in the twenty year means of the subtropical and subpolar gyre. However, the subtropical and subpolar Ψ_z variability in HiGEM is at times not meridionally coherent even when a lag is accounted for (Figure 4.5), and so the results of Lozier et al. (2010) may still highlight how overturning in the SPG and STG displays different periods of variability.

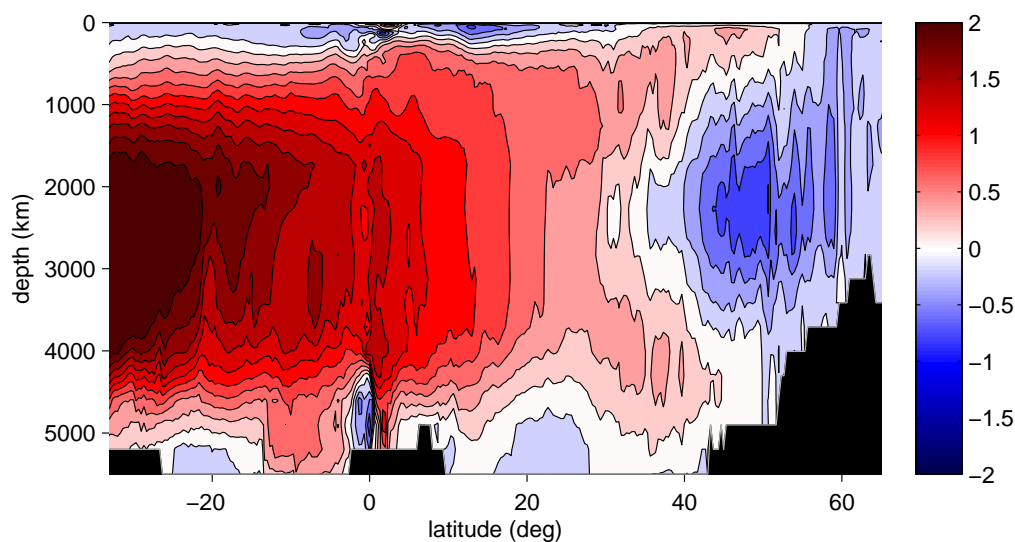


Figure 4.10: Change in 20 year time-mean ψ_z , years 55-75 minus years 25-45. Black shading shows the maximum depth of topography. Units are Sv.

An interesting feature of the lagged correlations of Ψ_z referenced to 50°N (Figure 4.9a-d) is the apparently slower meridional adjustment speed of Ψ_z relative to Ψ_σ , as evidenced by the longer lag time of the low latitude bands of maximum correlation. On the equator the bands of maximum Ψ_z and Ψ_σ correlation are respectively centred at approximately 5 years and 3 years. The source of the longer lag times appears to originate at a ‘kink’ between approximately 45°N and 37°N in the Ψ_z positive correlation band. In this latitude range the southwards propagation of Ψ_z anomalies appears to slow down relative to the propagation speeds further north and south. This kink is evident in other models (Zhang, 2010; Hodson and Sutton, 2012), and has been associated (Zhang, 2010) with the slower southwards propagation time scales of interior deep current pathways observed in this latitude range (Bower et al., 2009). The kink is particularly evident in lagged correlations of $\Psi_{z,lp}$ when the meridional Ekman transport (calculated at each latitude from the wind) has been subtracted (Figure 4.11). Since the kink is not evident in (unfiltered or low pass filtered) Ψ_σ in HiGEM it is difficult to know whether the slow down is a genuine feature of ocean adjustment to overturning variability or if it is an artifact of the spatially-integrated nature of the overturning. Removal of meridional Ekman transports from Ψ_σ is non-trivial, so it is yet to be addressed whether the Ekman transport is also disguising a change in the southwards adjustment time of Ψ_σ variability. By replacing latitude with ‘distance along the western boundary from 55°N ’ in Hovmöller plots of Ψ_z it has been verified that the geographical shape of the western boundary is not responsible for the kink.

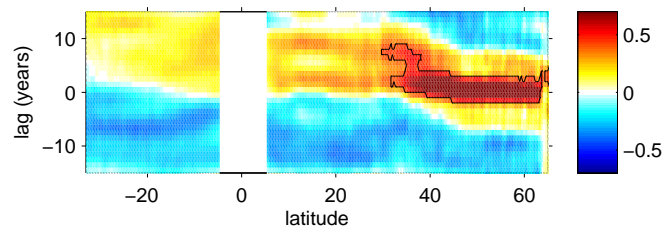


Figure 4.11: Lagged correlation at each latitude between $\Psi_{z,lp}$ at 55°N and $\Psi_{z,lp}$ with the meridional Ekman transport removed. Latitudes 5°S - 5°N have been masked because of the effect of dividing by small values of f . Correlation coefficients given in normalised units.

4.6 Depth space and density space overturning differences

4.6.1 High Latitude Ocean Processes

This section identifies which ocean processes are related to the variability of maximum overturning at high and low frequencies and discusses the potential causes for the main differences between Ψ_z and Ψ_σ variability. In the previous section, overturning variability has been shown to originate at high latitudes and to subsequently propagate to lower latitudes to bring about variability that is consistent with higher latitudes (Figure 4.9). It has also been shown that Ψ_z and Ψ_σ variability only differ substantially in subpolar latitudes (Figure 4.5 and Figure 4.7). The focus here is therefore on the relationship of the maximum overturning to various high latitude ocean variables.

We investigate high latitude ocean variables that have been associated with overturning variability in past studies: 1) the strength of the DSOW transports (e.g. Gregory et al., 2005), calculated as the net southward transport below the 1037.6 kg m^{-3} potential density isopycnal between Greenland and Iceland; 2) the SPG strength (e.g. Zhang, 2008) at 55°N , calculated as the maximum barotropic stream function at 55°N , which represents an integrated strength of the cyclonic circulation at this latitude (henceforth simply SPG strength); 3) the maximum mixed layer depth (MLD) in the Labrador, Irminger and Greenland-Iceland-Norwegian (GIN) seas; 4) maximum downwards net surface heat flux (SHF) in the Labrador, Irminger and Greenland-Iceland-Norwegian (GIN) seas; 5) the zonal mean meridional Ekman transport at 55°N since it is a component of the meridional surface flow. The MLD and SHF are chosen to act as proxies for WMT and convective mixing (e.g. Eden and Willebrand, 2001; Biastoch et al., 2008).

Time series of the ocean variables are shown in Figure 4.12. For comparison, time series of Ψ_z and Ψ_σ at 55°N are also shown. Grey lines are 5 year low pass filtered time series. Decadal means (years 1-10) of the SPG stream function, the Denmark Straits velocities, the MLD and the SHF are shown in Figure 4.13, where the black boxes in Figure 4.13(b,d) mark the boundaries used to define the Labrador, Irminger and GIN seas, and the

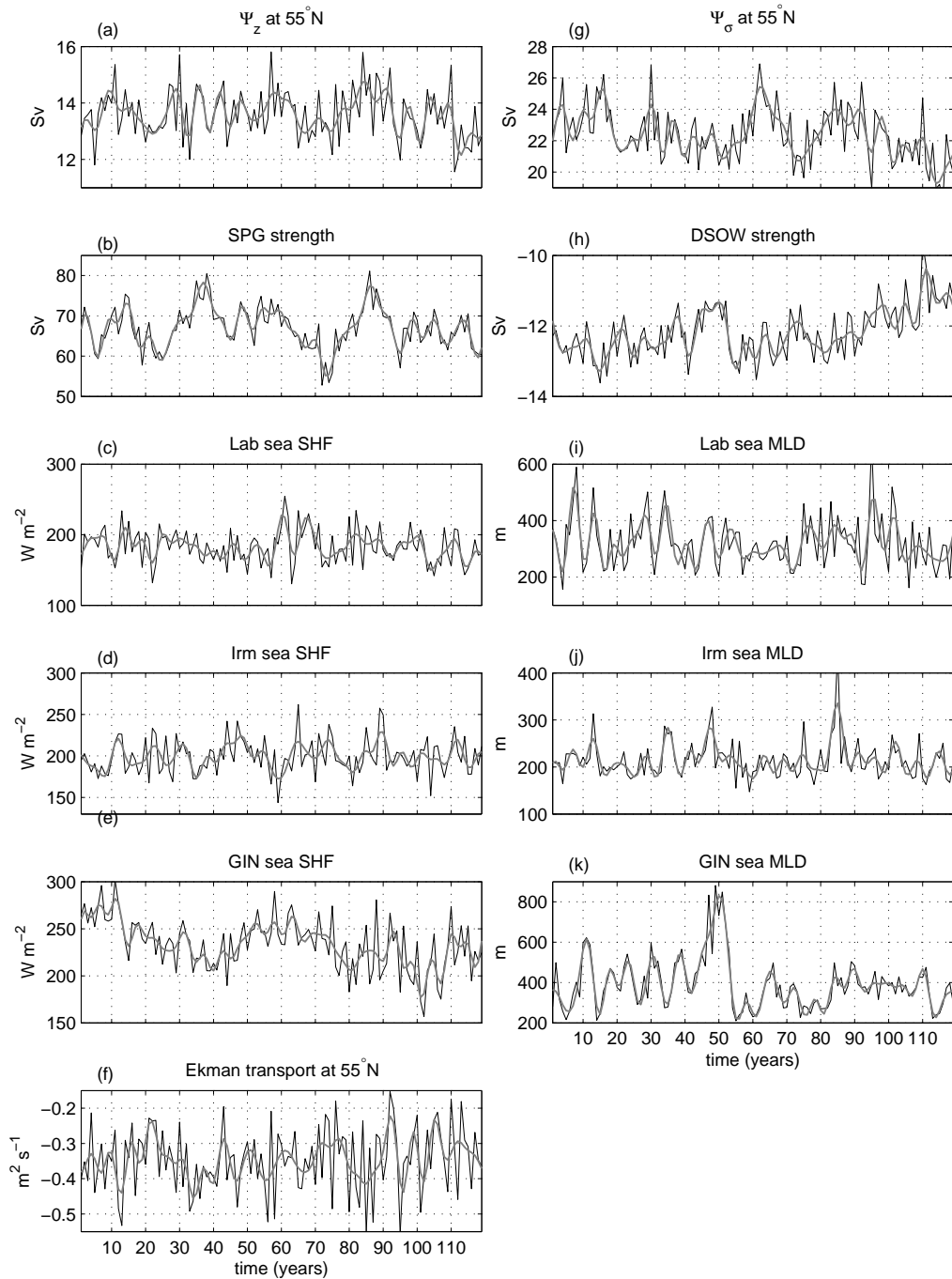


Figure 4.12: Time series of (a) Ψ_z at 55°N, (b) SPG strength, maximum upwards surface heat flux in the (c) Labrador, (d) Irminger and (e) GIN seas, (f) Zonal mean meridional Ekman transport at 55°N, (g) Ψ_σ at 55°N, (h) DSOW strength, maximum mixed layer depth in the (i) Labrador, (j) Irminger and (k) GIN seas. 5 year low pass filtered time series are in grey.

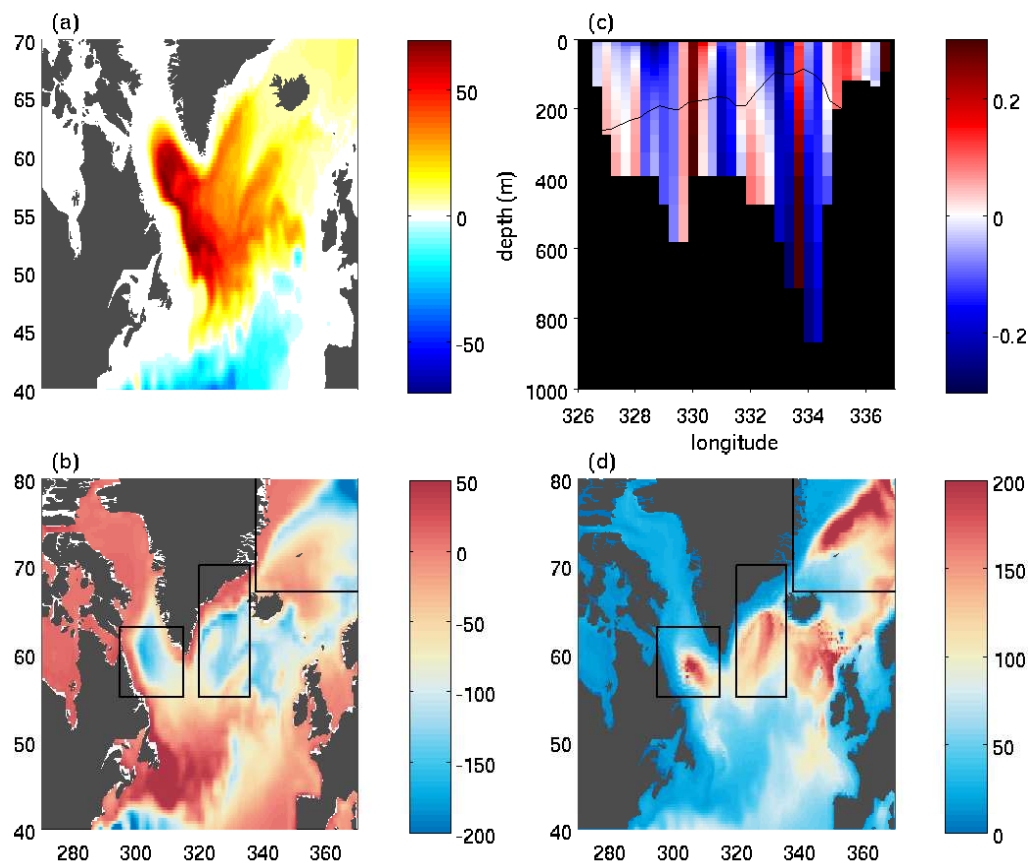


Figure 4.13: Decadal means of (a) SPG strength (in Sv), (b) North Atlantic surface heat flux (in $W m^{-2}$), (c) Denmark Straits velocities (in $m s^{-1}$) and (d) North Atlantic mixed layer depth (in m). The black contour in (c) is the potential density isopycnal of $1037.6 kg m^{-3}$. The black boxes in (b) and (d) mark the domains used to define the Labrador, Irminger and GIN seas.

black contour in Figure 4.13(c) marks the time-mean $1037.6 kg m^{-3}$ potential density isopycnal that is used to define DSOw, as described above.

4.6.2 High Frequency AMOC variability

The high frequency AMOC variability is first investigated. Time series of $\Psi_{z, hp}$ and $\Psi_{\sigma, hp}$ at $55^{\circ}N$ are shown in Figure 4.14 along with the 5 year high pass filtered Ekman transport at $55^{\circ}N$. The high pass filtered Ekman transport at $55^{\circ}N$ can be considered representative of subpolar Ekman variability since it is significantly and positively correlated to high pass filtered Ekman transport fluctuations at all other subpolar latitudes (Figure 4.15a). Variability of both $\Psi_{z, hp}$ and $\Psi_{\sigma, hp}$ correlate well with the high pass filtered

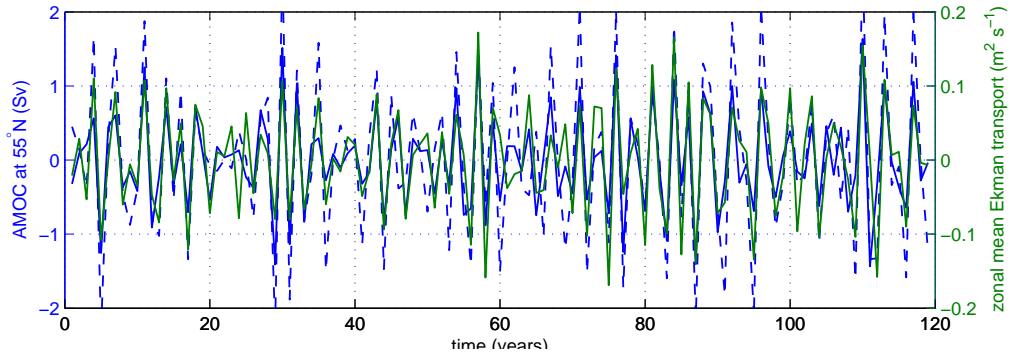


Figure 4.14: Time series of $\Psi_{z,hp}$ (blue solid, left axis), $\Psi_{\sigma,hp}$ (blue dashed, left axis) and the high pass filtered Ekman transport (green, right axis).

Ekman transport variability with respective correlation coefficients of 0.81 and 0.79 at zero lag. Correlations between the Ekman transport and the maximum high pass filtered overturning at different latitudes of the Atlantic are consistently high (Figure 4.15b,c). It is therefore suggested here that the Ekman transport variability dominates both $\Psi_{z,hp}$ and $\Psi_{\sigma,hp}$ variability. The correlations with wind stress are higher than correlations of high pass filtered maximum overturning to all other ocean variables (not shown), so it can be suggested that Ekman variability itself, rather than another process that is related to wind, is the main cause of high frequency overturning variability. The reason for why $\Psi_{\sigma,hp}$ variability is stronger than $\Psi_{z,hp}$ variability is unclear and warrants further work.

4.6.3 Low Frequency AMOC variability

To investigate the low frequency variability of the AMOC, lagged correlations of each of the low pass filtered high latitude ocean variables mentioned in section 4.6.1 are made with $\Psi_{z,lp}$ (Figure 4.16) and with $\Psi_{\sigma,lp}$ (Figure 4.17) at each latitude. Throughout the rest of this section only 5 year low pass filtered time series are considered. The general picture that emerges is that both $\Psi_{z,lp}$ and $\Psi_{\sigma,lp}$ correlate to a non-negligible extent with each of the ocean variables. Since the SPG is an integrated measure of many processes that contribute to the large scale circulation and therefore to overturning, the correlations to each of these processes may explain why both $\Psi_{z,lp}$ and $\Psi_{\sigma,lp}$ show a meridionally coherent band of correlation to the SPG strength. Positive correlations between maximum overturning and the SPG strength

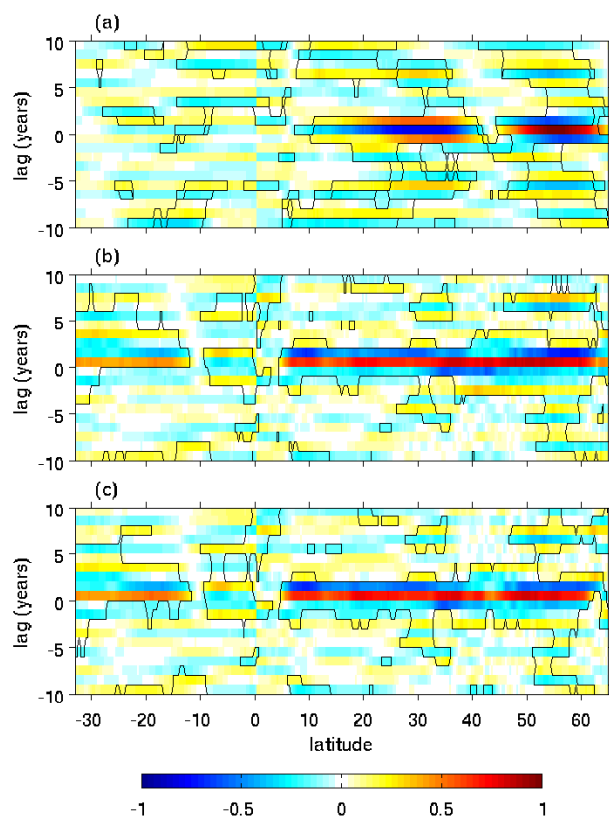


Figure 4.15: Lagged correlations at each latitude for high pass filtered: (a) Ekman transport at 55°N with the Ekman transport at each latitude; (b) Ekman transport at each latitude with Ψ_z at the same latitude; (c) Ekman transport at each latitude with Ψ_σ at the same latitude. The latitude independent variable leads at positive lag. Black contours represent the 95% confidence interval. Correlation coefficients are in normalised units.

persist throughout the Atlantic with zero lag times centred on subpolar latitudes. The results agree with previous studies that demonstrate an in-phase relationship between Ψ_z and the SPG strength (e.g. Häkkinen and Rhines, 2004; Böning et al., 2006). On the other hand, Zhang (2008) reports an anti-correlated relationship. Correlations of the SPG strength with $\Psi_{\sigma,lp}$ are smaller than with $\Psi_{z,lp}$ in subpolar latitudes (Figure 4.17). This could be due to a reduced importance of the SPG strength on $\Psi_{\sigma,lp}$ but also to an increased importance of another process (that does not increase the strength of the SPG). If the assumption is made that the southwards transport of the SPG is contained mostly in the WBC (such that fluctuations in the SPG strength must be mirrored in the strength of the WBC) then a strong relationship emerges between the WBC strength and $\Psi_{z,lp}$, and less so with $\Psi_{\sigma,lp}$.

The largest correlation differences between $\Psi_{z,lp}$ and $\Psi_{\sigma,lp}$, in the extent to which they correlate to the ocean variables, are all located in subpolar latitudes (Figure 4.16 and Figure 4.17). The largest of these differences is the stronger correlation of the DSOW strength with $\Psi_{\sigma,lp}$ throughout subpolar latitudes. This is suggested here to be the dominant reason for differences in variability displayed in the low pass filtered Hovmöller plots of Ψ_z and Ψ_σ (Figure 4.7a-c). The DSOW transport introduces dense Nordic Seas water into the DWBC. The vertical component of overturning associated with this can be expected to affect both $\Psi_{z,lp}$ and $\Psi_{\sigma,lp}$, which explains why both are correlated to the DSOW strength. However, the presence of dense Nordic Seas water in the WBC will lead to large zonal density gradients across the basin. A further effect of the DSOW strength on Ψ_σ can therefore be expected. Increases in DSOW strength are immediately followed by increases in AMOC strength at approximately 65°N and then approximately 1 to 2 years later by increases in AMOC strength in mid-subpolar latitudes. The dynamical mechanisms by which the depth and density space overturning are separately affected by fluctuations in the DSOW strength and SPG strength are investigated in more detail in the following subsection.

The maximum SHF in the Labrador Sea significantly correlates to $\Psi_{\sigma,lp}$ (Figure 4.17b) but not to $\Psi_{z,lp}$ (Figure 4.16b). This may reflect the presence of WMT that modifies surface densities enough to contribute to $\Psi_{\sigma,lp}$ but not to $\Psi_{z,lp}$. If SHF leads to WMT but only to shallow, weak or no convective mixing and downwelling then its effect on overturning will mostly be limited to $\Psi_{\sigma,lp}$. Correlations between $\Psi_{\sigma,lp}$ and the maximum SHF in the Irminger Sea, however, are generally not significant (Figure 4.17c), possibly because of smaller water mass residence times in this area. Conversely, the maximum MLD in both the Labrador and Irminger Seas correlates significantly to $\Psi_{z,lp}$ (Figure 4.16g,h) but not to $\Psi_{\sigma,lp}$ (Figure 4.17g,h). If convection related downwelling in HiGEM is occurring, and water masses are retaining a constant density throughout the sinking process, then this may explain why MLD correlates only with $\Psi_{z,lp}$ (see section 4.3). Alternatively, it is possible that the $\Psi_{\sigma,lp}$ response to the MLD is simply masked by the larger response to e.g. the DSOW strength. Increases in maximum MLD in the Labrador and Irminger seas lead increases in $\Psi_{z,lp}$ by approximately 1 to 2 years (Figure 4.16g,h). Similarly, increases in Labrador Sea maximum

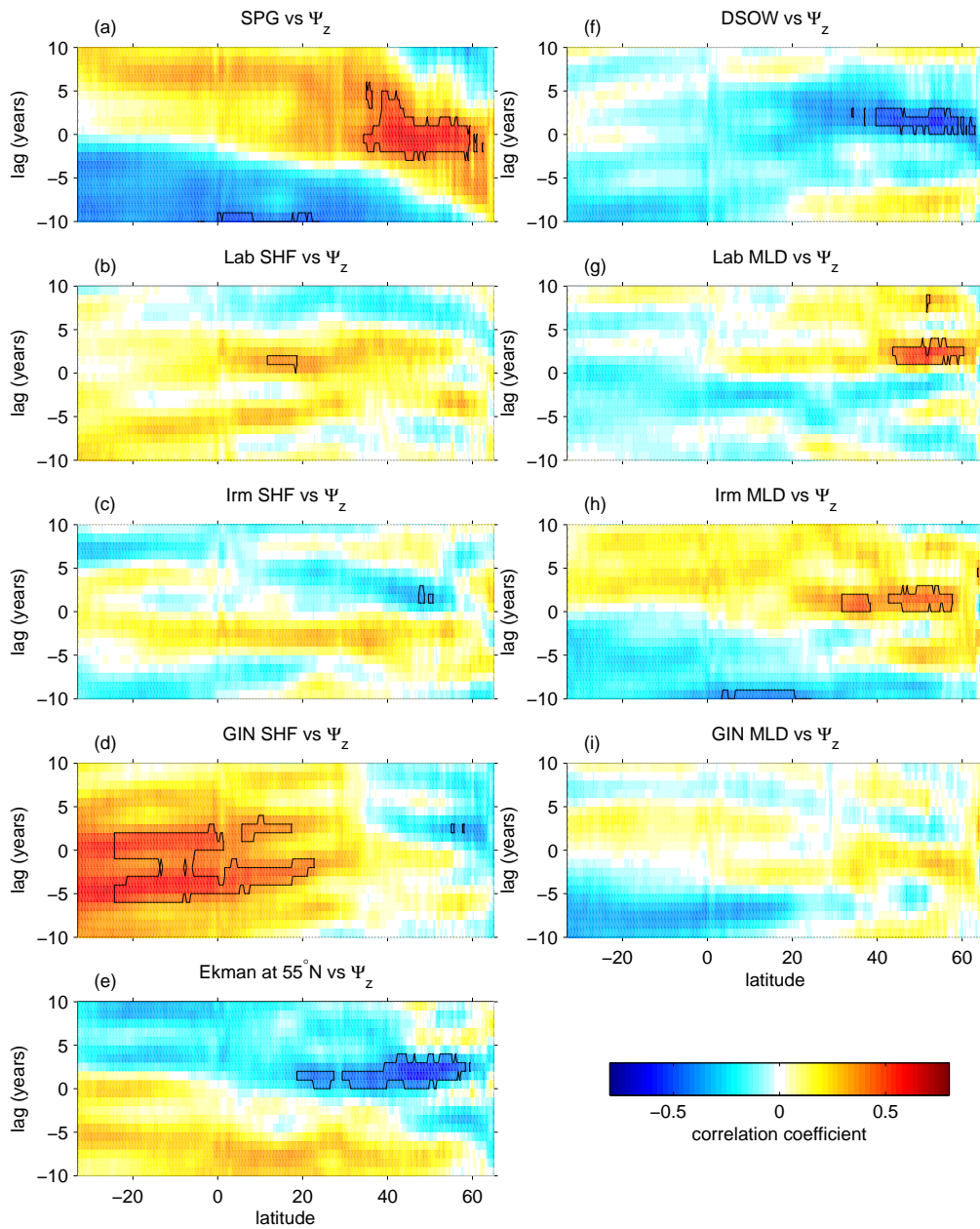


Figure 4.16: Lagged correlations at each latitude between 5 year low pass filtered Ψ_z and 5 year low pass filtered: (a) SPG strength; maximum surface heat flux in the (b) Labrador, (c) Irminger and (d) GIN seas; (e) DSOW strength; maximum mixed layer depth in the (f) Labrador, (g) Irminger and (h) GIN seas. The overturning lags at positive lag. Black contours represent the 95% confidence interval. Correlation coefficients are in normalised units.

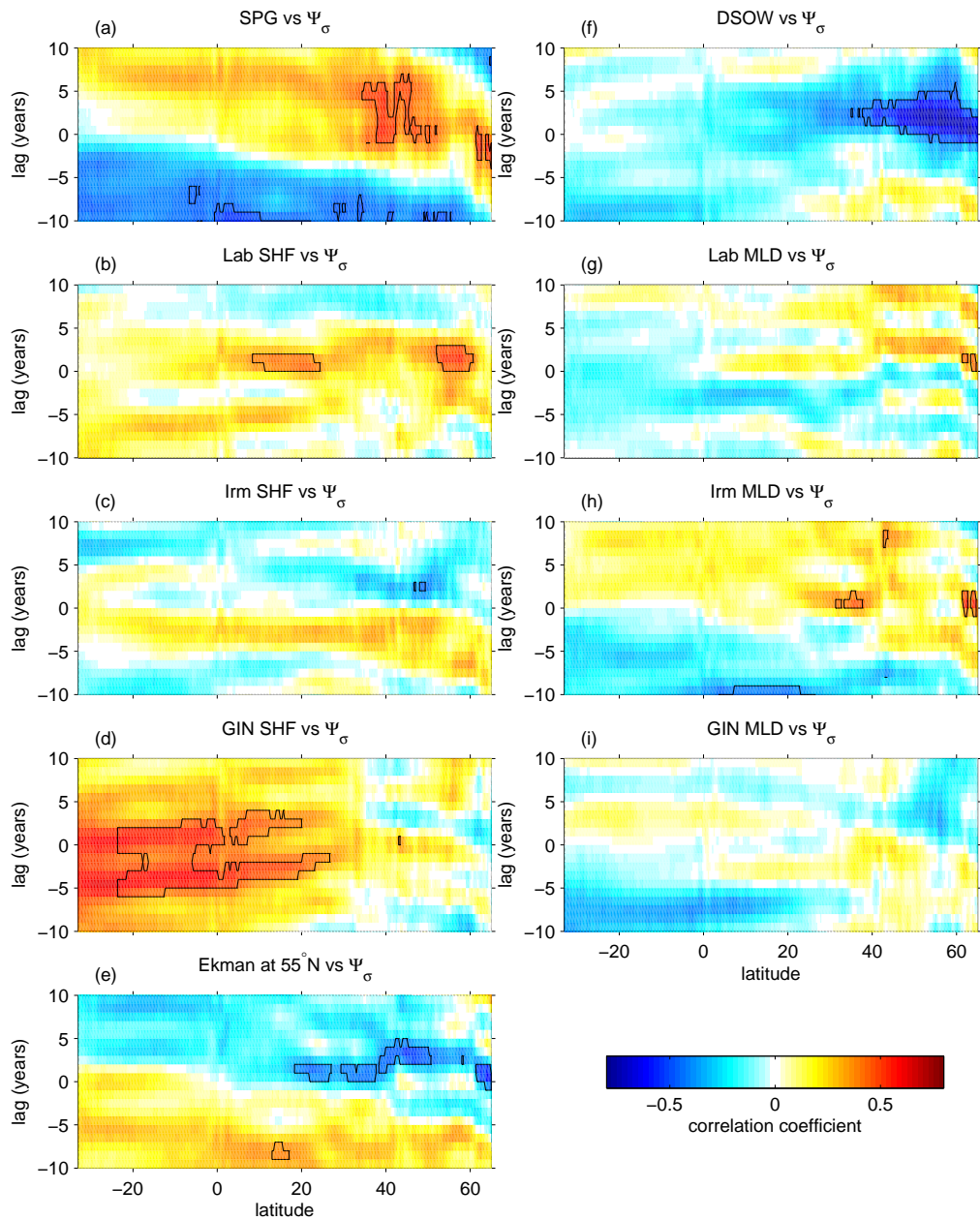


Figure 4.17: Lagged correlations at each latitude between 5 year low pass filtered Ψ_σ and 5 year low pass filtered: (a) SPG strength; maximum surface heat flux in the (b) Labrador, (c) Irminger and (d) GIN seas; (e) DSOW strength; maximum mixed layer depth in the (f) Labrador, (g) Irminger and (h) GIN seas. The overturning lags at positive lag. Black contours represent the 95% confidence interval. Correlation coefficients are in normalised units.

SHF lead increases in $\Psi_{\sigma,lp}$ by approximately 1 to 2 years (Figure 4.17b). Convective and WMT processes, if they are well represented by MLD and SHF, therefore do not have an immediate impact on the AMOC but prime it for a later increase.

While some coherent structure is evident in correlations of maximum overturning with the GIN seas maximum SHF and maximum MLD, correlations are mostly not significant in subpolar latitudes to either $\Psi_{z,lp}$ (Figure 4.16d) or $\Psi_{\sigma,lp}$ (Figure 4.17d). This does not necessarily mean that convection and dense water formation in the GIN seas are not important for overturning, but that there is no regular residence time before water is exported from the GIN seas through the Straits of the GSR. If the period of time between the formation of dense water in the GIN seas and its export into the subpolar gyre is variable, then a correlation will not be established between the dense water formation and overturning. However, the low correlations support recent observations that showed increases in DSOW are not a response to increased GIN seas convection but to enhanced recirculation of water of Atlantic origin around the rim of the GIN seas (Eldevik et al., 2009). The $\Psi_{z,lp}$ and $\Psi_{\sigma,lp}$ variability in the tropics each correlate significantly with the maximum SHF in the GIN seas at negative lag times. This might suggest that increased overturning strength in the tropics leads to increased loss of heat from the GIN seas up to 5 years later. If this is the case then a band of significant correlation might then be expected to persist throughout the Atlantic. The lack of significant correlation in the subtropics may therefore be due to the increased importance of processes unrelated to GIN seas heat loss on subtropical overturning variability.

Correlations of $\Psi_{\sigma,lp}$ and $\Psi_{z,lp}$ at 55°N with the low pass filtered Ekman transport are also 95% significant throughout subpolar and subtropical latitudes (Figure 4.16e and Figure 4.17e). Earlier studies have also discussed the importance of wind on the overturning. However, it is not straightforward to determine by what processes the wind impacts the overturning since, as well as the Ekman transport (which might be expected to have a small affect on long timescale AMOC variability; Buckley et al., 2012), it can affect e.g. the convection strength (Eden and Willebrand, 2001), the SPG strength (Häkkinen and Rhines, 2004) and intergyre exchange that ultimately impacts overturning through density modification (Hátún et al.,

2005). A decomposition of the various processes by which the winds affect overturning in depth and density space is therefore suggested for future work.

4.7 Mechanisms of Subpolar AMOC Variability

This section addresses the different mechanisms by which Ψ_z and Ψ_σ variability are separately affected by the DSOW strength and the SPG strength, the ocean variables that correlate most with overturning (Figure 4.16 and Figure 4.17). To investigate the mechanisms of variability we establish the relationship of overturning with the pointwise transports and densities in the subpolar gyre. At each latitude-longitude point the vertically averaged magnitude of the horizontal velocity vector (Figure 4.18) and depth-averaged potential density anomaly (Figure 4.19) are correlated onto $\Psi_{z,lp}$ at 55°N, $\Psi_{\sigma,lp}$ at 55°N, the low pass filtered SPG strength and the low pass filtered DSOW strength. The depth integrated transports and depth averaged density anomalies are 5 year low pass filtered. In the SPG the transports are largely equivalent barotropic and the density anomalies tend to have the same polarity at all depths so that the spatial correlations represent transport and density variations at all depths (not shown).

There is a strong relationship between $\Psi_{z,lp}$ at 55°N and the transports of the WBC. This is demonstrated by a high band of correlation that runs along the western boundary, starting in the North East Atlantic at positive lag times (at which the transport leads the AMOC) and ends south of Newfoundland at negative lag times (Figure 4.18a,e). A similar relationship exists between the SPG strength and the WBC transports. It is likely therefore that the mutual relationship to the WBC transports explains the correlation between the SPG strength and $\Psi_{z,lp}$ shown in the previous subsection (Figure 4.16a). The mechanism by which the WBC transport impacts Ψ_z is as depicted in scenario 2 and scenario 3 of Figure 4.4. Part of the southwards transport in the western SPG is deeper than the northwards transport in the eastern SPG and so do not cancel when zonally integrated.

The $\Psi_{\sigma,lp}$ variability at 55°N is correlated to a thin band of transport variability between the Denmark Straits and the southern tip of Greenland

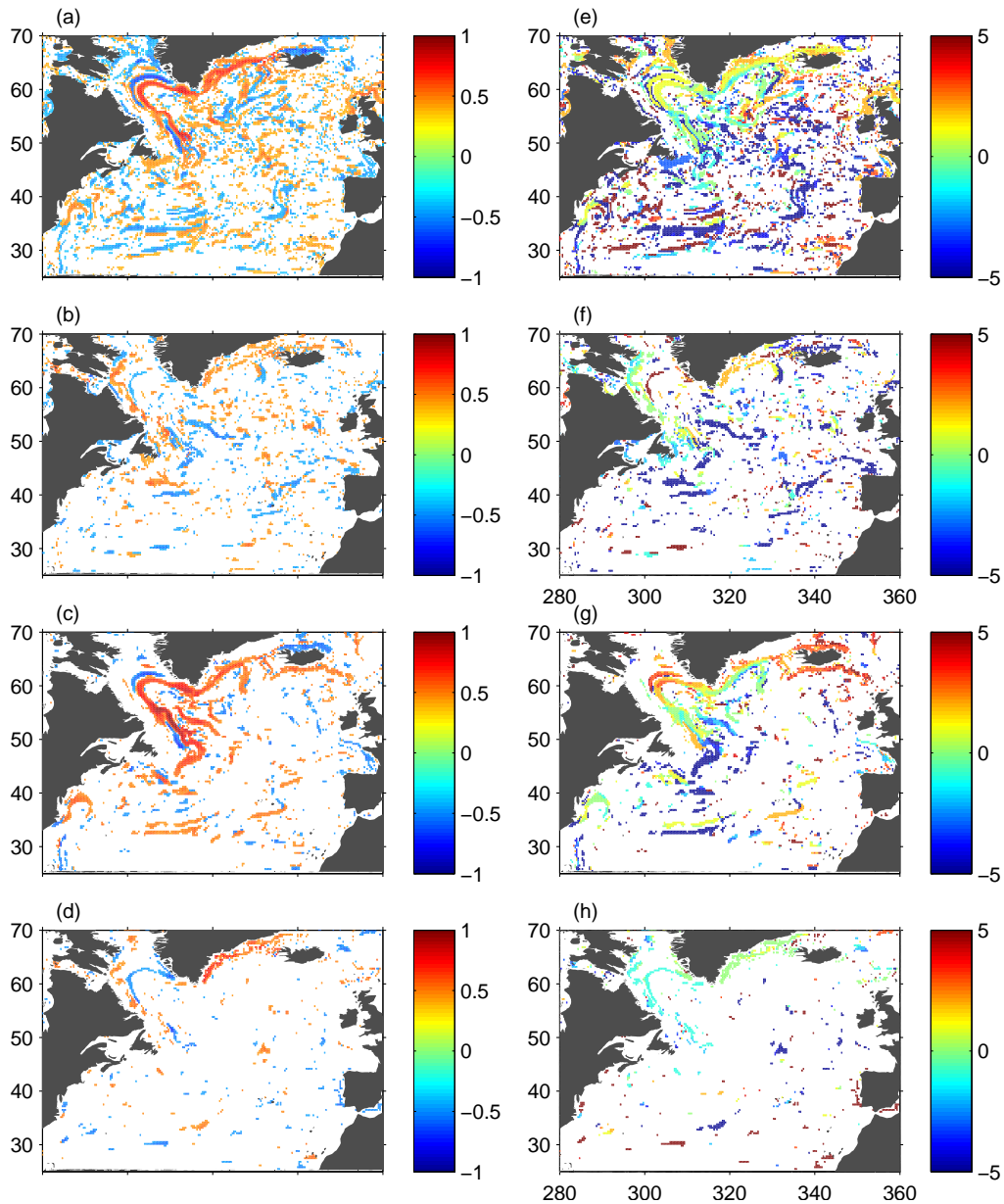


Figure 4.18: (a-d) Coefficient and (e-h) lag (in years) of maximum correlation between 5 year low pass filtered vertically averaged magnitude of the horizontal velocity vector at each location in the North Atlantic and (a,e) $\Psi_{z,lp}$ at 55°N, (b,f) $\Psi_{\sigma,lp}$ at 55°N, (c,g) 5 year low pass filtered SPG strength and (d,h) 5 year low pass filtered DSO strength. Only correlations that are significant at 95% are displayed.

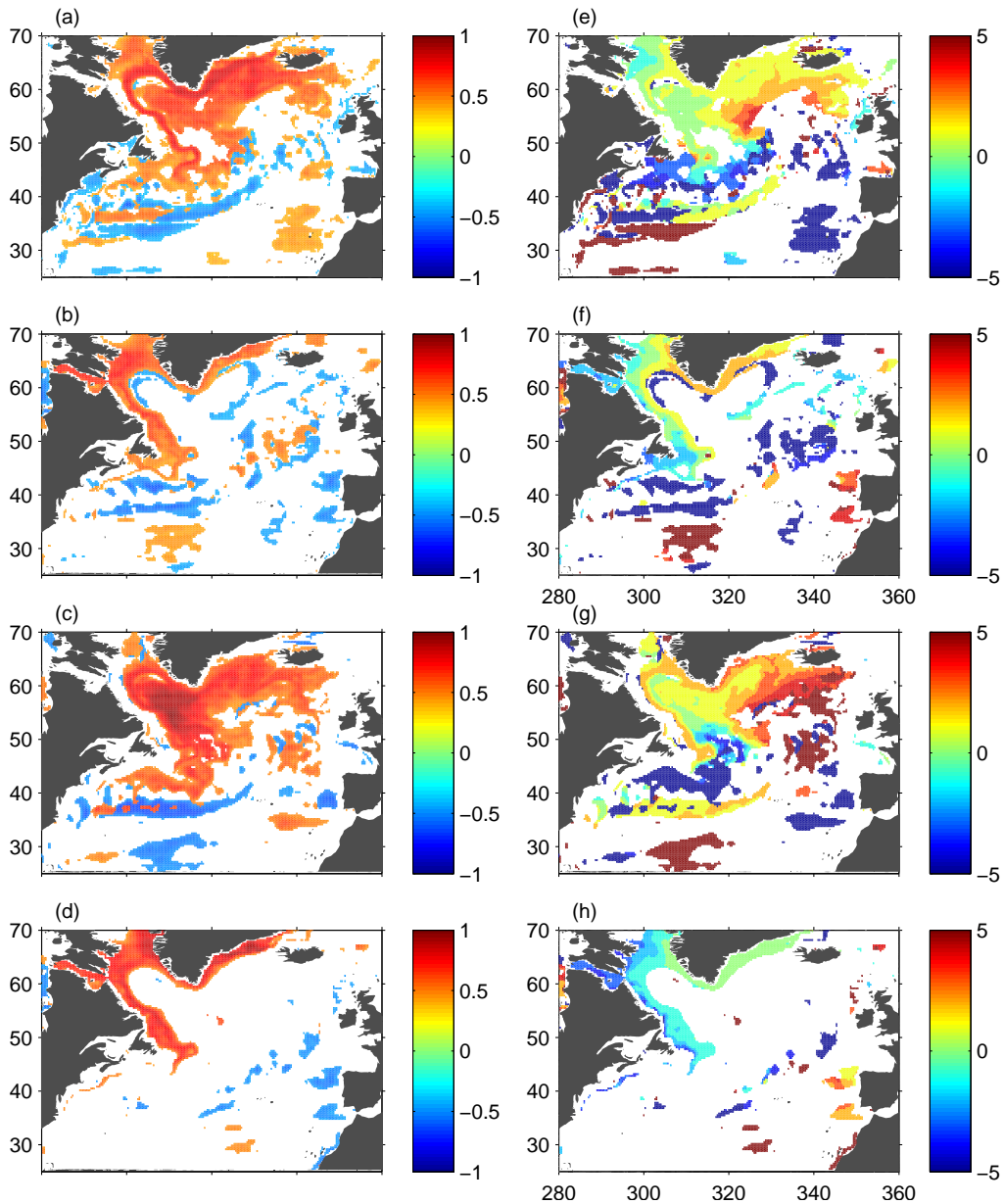


Figure 4.19: (a-d) Coefficient and (e-h) lag (in years) of maximum correlation between 5 year low pass filtered depth averaged density anomaly at each location in the North Atlantic and (a,e) $\Psi_{z,lp}$ at 55°N , (b,f) $\Psi_{\sigma,lp}$ at 55°N , (c,g) 5 year low pass filtered SPG strength and (d,h) 5 year low pass filtered DSOW strength. Only correlations that are significant at 95% are displayed.

(Figure 4.18b,f). Similar correlations are seen between the depth integrated transports and the DSOW strength (Figure 4.18d,h). Increases in DSOW strength therefore increase the transports in this region and subsequently increase $\Psi_{\sigma,lp}$, also in a manner like those depicted in scenario 2 and scenario 3 of Figure 4.4: southwards transports in this region are denser than northwards transports further east and so changes in strength can affect Ψ_{σ} . The WBC transports, however, generally show a much weaker relationship to $\Psi_{\sigma,lp}$ than they do to $\Psi_{z,lp}$. The variability of $\Psi_{\sigma,lp}$ is instead much more correlated with the density anomalies close to the western boundary region of the SPG (Figure 4.19b,f). Lag times reduce southwards around the western side of the basin from positive lag times of approximately 2 years at the Denmark Straits to approximately 0 years lag at 55°N. The very similar pattern evident in correlations between density anomaly and the DSOW strength (Figure 4.19d) indicates a link between the density of the DSOW and the strength of $\Psi_{z,lp}$. Density anomalies close to the Denmark Straits increase immediately after an increase in DSOW strength and approximately 1-2 years later at 55°N (Figure 4.19h).

An enhanced WBC density can increase the $\Psi_{\sigma,lp}$ strength by ensuring that a larger fraction of the southwards transports have a higher density than the northwards transports, and so do not cancel out in Ψ_{σ} . Increases in DSOW strength therefore inject high density water into the WBC that increase $\Psi_{\sigma,lp}$ without having to greatly enhance the volume transport of the WBC. Indeed, the density of the WBC is more important for $\Psi_{\sigma,lp}$ variability (Figure 4.19b) than the volume transport of the WBC (Figure 4.18b). This is as depicted in scenario 1 and 3 of Figure 4.4 in which more of the southwards transport contributes to Ψ_{σ} than it does to Ψ_z .

The high correlations between the DSOW strength and $\Psi_{\sigma,lp}$ shown in the previous subsection (Figure 4.17f) are therefore explained by density anomalies. Additionally, if the assumption is maintained that fluctuations in the SPG strength are mirrored in the strength of the WBC, then the reduced importance of the SPG strength on $\Psi_{\sigma,lp}$ relative to $\Psi_{z,lp}$ (Figure 4.16a and Figure 4.17a), is explained by the weak dependence of $\Psi_{\sigma,lp}$ on the WBC transports (Figure 4.18b). Note that the lag zero correlation between $\Psi_{\sigma,lp}$ at 55°N and the density anomalies occur on the Canadian shelf (Figure 4.19f). The same is true for correlations between the DSOW strength and

the density anomalies (Figure 4.19h), so it is not clear if the anomalies originate in the Denmark Straits or if both the DSOW strength and the density anomalies are driven by e.g. atmospheric forcing that causes WMT to occur over the entire region. This would agree with the results from a coarse resolution model, in which the bulk of convective activity occurred on the continental shelf (Medhaug et al., 2011). This, however, would not explain the southwards transit from the Denmark Straits as shown in the lag times of correlation (Figure 4.19f,h).

The horizontal distribution of the density anomaly correlations with $\Psi_{\sigma,lp}$ (Figure 4.19b,f) are different to those with $\Psi_{z,lp}$ (Figure 4.19a,e). Correlations between $\Psi_{z,lp}$ and density anomaly are located off the Canadian shelf, exist throughout most of the western SPG and have a lag zero correlation centred in the middle of the Labrador Sea (Figure 4.19a,e). A very similar spatial structure is displayed in correlations between the SPG strength and the density anomalies (Figure 4.19c,g). A possible mechanism might be that density anomalies in the Labrador Sea, related to isopycnal doming, lead subsequently to a spin-up of the cyclonic currents. This would increase the SPG strength and therefore also the strength of the WBC transports and $\Psi_{z,lp}$. We suggest two possible causes for the isopycnal doming. The first is that doming is related to convective activity, a mechanism that supports the findings that the MLD maximum in the Labrador Sea correlates to $\Psi_{z,lp}$ (Figure 4.16g). The second is that doming is modified by the wind stress curl which leads to Ekman pumping. This supports the findings of Häkkinen et al. (2011) who showed the wind stress curl is important for the shape and strength of the gyre circulation. Of course, both causes may contribute to doming.

4.8 Conclusions

This chapter has addressed the inter-annual to decadal period variability of the Atlantic Meridional Overturning Circulation (AMOC) using annual output from a 120 year control run of the eddy-permitting model, HiGEM. The main aim has been to determine the ocean processes that are related to AMOC variability in depth space (ψ_z) and density space (ψ_σ) and to elucidate the different mechanisms that give rise to their differences. A partic-

ular focus is given to density space overturning, which is perhaps the more climatically important (Mauritzen and Häkkinen, 1999; Zhang, 2010) yet less studied representation of overturning. Inter-annual and decadal period variability have been separately studied by splitting the AMOC variability and other variables into high and low frequency components using a 5 year Fourier filter cutoff.

Substantial differences are seen between the magnitude of the variability of ψ_z and of ψ_σ in the subpolar gyre (SPG) in HiGEM, with differences of up to a factor of 2 (Figure 4.5). In the subtropical gyre, however, the differences are negligible. The boundary between the subtropical and subpolar gyres lies at approximately 40°N and delineates a transition from weak subtropical zonal density gradients to steep subpolar zonal density gradients. In the subtropics flat isopycnals mean that any northwards and southwards transports that occur at the same depth also occur at the same density and so will cancel out in both ψ_z and ψ_σ once zonally integrated to obtain the stream function. In this case ψ_z and ψ_σ variability are the same and are caused by overlying layers of opposing transport with different densities. In subpolar latitudes, however, zonal density gradients mean that meridional transports occurring at the same depth cancel out in depth space once zonally integrated but do not in density space. Such transports therefore contribute only to ψ_σ . As a result, the latitude of maximum ψ_σ is located further north at approximately 50°N (Figure 4.1) in comparison to the more southerly 40°N of the maximum ψ_z (Figure 4.1). Moreover, in agreement with Zhang (2010), the largest ψ_σ variability is located within the subpolar gyre, whereas ψ_z variability begins to weaken here relative to the subtropical AMOC variability (Figure 4.8).

Building on earlier work that shows AMOC variability in the subpolar and subtropical gyres have different (Bingham et al., 2007) or opposing (Lozier et al., 2010) periodicity, AMOC fluctuations in HiGEM are found to be meridionally coherent when propagation timescales of AMOC anomalies from high to low latitudes are accounted for (Figure 4.9). This is true for filtered and unfiltered time series of both depth and density space AMOC, though meridional coherence is slightly enhanced in density space and in low pass filtered calculations of AMOC. The results support the findings of Zhang (2010) and demonstrate further that meridional coherence is ap-

parent in an eddy permitting coupled model and also in depth space overturning. Time scales of meridional adjustment are of the order of a few years, suggesting that AMOC signals are advected by the flow (Smethie et al., 2000) rather than propagated by waves (although the annual output used will be unlikely to resolve Kelvin wave propagation; Johnson and Marshall, 2002). As previously discussed (Zhang, 2010), meridional coherence has implications for the monitoring efforts by the RAPID array (Kanzow et al., 2007; McCarthy et al., 2012): AMOC variability at 26.5°N could potentially be used to interpret climatic signals whose origins lie at high latitudes. Note, however, that ψ_σ in the SPG in HiGEM is much more temporally variable than in the STG (Figure 4.5). Information would therefore be lost if high latitude AMOC variability was interpreted from lower latitudes. Furthermore, ψ_σ variability has been shown to be less coherent than ψ_z within subpolar latitudes (Figure 4.9), indicating that a full diagnosis of high latitude ψ_σ variability would be difficult from the RAPID array.

Lozier et al. (2010) recently identified that opposing cycles of ψ_z variability took place in the subpolar and subtropical gyres between two 20 year averages (years 1950-1970 and 1980-2000) of hydrographic data. The results here suggest that natural decadal variability can explain such changes without any long term trends being present. Further, the propagation time for a depth space overturning anomaly to reach subtropical latitudes from the subpolar gyre in HiGEM may explain the opposing cycles of variability as being a result of unaccounted for lag times in the twenty year means. Depth space overturning variability that is meridionally coherent from high to low latitudes when propagation times are accounted for might lead to opposite anomalies in the SPG and STG when averaged over 20 year periods (Figure 4.10).

The primary driver of 5 year high pass filtered AMOC variability is the meridional Ekman transport (Figure 4.14). The zonal mean meridional Ekman transport at 55°N correlates to depth and density space AMOC at the same latitude with correlations coefficients of 0.81 and 0.79 respectively. The 5 year low pass filtered AMOC is more complicated (Figure 4.17). While both depth space and density space overturning are correlated to the SPG strength and to the strength of the Denmark Straits Overflow Water, depth space AMOC relates more to the SPG strength and density

space AMOC relates more to the DSOW strength. The ψ_z relationship to the SPG strength is explained by an increased dependence on the transport strength of the western boundary current in the subpolar gyre, which follows isopycnal doming in the Labrador Sea and subsequent spin up of the gyre circulation. In contrast, ψ_σ is influenced far more by density anomalies injected into the western boundary current through the Denmark Straits. Higher densities at the western boundary mean that more of the southwards transport can contribute to ψ_σ without cancelling out when zonally integrated.

Using mixed layer depth (MLD) and surface heat flux (SHF) as indices of convection and water mass transformation (WMT) respectively, it is found that Labrador Sea and Irminger Sea convection are important for ψ_z variability (Figure 4.16g,h), and Labrador Sea WMT is important for ψ_σ variability (Figure 4.17b). The AMOC in each case lags by 1 to 2 years. However, the MLD and SHF may not be good respective indicators of convection and WMT in the annual mean output used in this study.

The differences between depth and density space representations of the AMOC have implications on how it should be monitored. The increased meridional coherence of a density space representation of the AMOC may suggest that it more accurately captures the processes that are important in setting AMOC strength. A number of past studies have established that the depth space AMOC is linked to the SPG strength (e.g. Häkkinen and Rhines, 2004; Böning et al., 2006; Zhang, 2008) and to Labrador Sea convection (e.g. Curry and McCartney, 2001; Eden and Willebrand, 2001; Biastoch et al., 2008), results that are in line with those presented here. According to this study, the reduced importance of these processes on the variability of the density space overturning may suggest that more focus be given to the transports and densities of the DSOW, which are more important for ψ_σ in HiGEM.

Some caution is required when interpreting results based on correlation statistics since only the very strongest correlations may stand out above the noise. Potentially important information may therefore be lost in some locations. Additionally, the correlation of two variables that is not supported by a clear physical mechanism may not represent causation but may be a consequence of a third mechanism that is related to both. A good exam-

ple is how the AMOC correlates with the Ekman transport, which may be because another process, such as convection or surface heat loss, is correlated to both the AMOC and the wind (and therefore Ekman transport). Model dependencies and other limitations of the study such as annual mean output and non-eddy resolving at high latitudes should also be considered. Nevertheless, the study has highlighted some potential processes that separately affect the overturning in depth and density space, and these should be further investigated in observations and other models.

Chapter 5

Conclusions and Discussion

Investigations have been made into Sverdrup balance and the Atlantic Meridional Overturning Circulation (AMOC) using two numerical ocean models. The AMOC is a two dimensional representation of a three dimensional system of currents whose variability is not well understood (Lozier, 2010). The main aim of this thesis has therefore been to investigate the variability and mechanisms of the ocean circulation that lead to changes in the AMOC, and to describe the dynamics within which those changes occur.

5.1 Sverdrup balance

Using the 16 year ECCO-GODAE state estimate of the global ocean since 1992 an investigation has been made into Sverdrup balance, which equates meridional transport to the wind stress curl. The time mean Sverdrup balance is found to be a good descriptor of the interior subtropical ocean circulation when considered away from the western boundary at spatial scales larger than approximately 5° , and when depth integrating to a mid-depth of 2200 m. More specifically, using two metrics to quantify the percentage balance of the model Sverdrup and ocean transports, the 5° smoothed Sverdrup balance is found to explain 69% of the time mean interior ocean circulation and the zonally integrated Sverdrup balance explains 80% of the circulation. Outside of the subtropics, in western boundary currents and at short spatial scales, significant departures from Sverdrup balance occur. These arise mostly due to errors from the assumption that there is a level of no motion that can be integrated to, and these errors are approximately a

factor of 2 larger than the errors from assuming linear vorticity balance. In support of the theory proposed by Anderson and Killworth (1977), the time scale of adjustment for the ocean to come into Sverdrup balance is shown to correspond with the basin crossing time for a first mode baroclinic Rossby wave.

Significant transports are found in the deep ocean below 2200 m depth that are not driven by wind but instead by Bottom Pressure Torque (BPT). This supports findings from other numerical models (Bryan et al., 1995; Hughes and de Cuevas, 2001). Interaction between deep currents and topography leads to BPT (vortex stretching) which in turn creates meridional transports through the conservation of potential vorticity. When Sverdrup balance is calculated by integrating to the ocean floor, there is a strong deviation from balance. The imbalance remains even when smoothing the terms horizontally over 5° . The BPT is found to affect the meridional velocity from the bottom up to depths of about 1.5 km. However, it is shown here that when considered at scales greater than approximately 5° the upper layer wind driven flow is effectively decoupled from the deep BPT driven flow, thereby leaving an upper layer in Sverdrup balance.

Linear vorticity balance is found to hold to a good order of approximation in the upper ocean, particularly when considered over large scales. Contrary to some earlier investigations (Lu and Stammer, 2004; Bryden, 1980), linear vorticity balance is found to hold poorly in a pointwise consideration in the deep ocean. At depths below 3000 m pointwise departures from linear vorticity balance can exceed 50% of the magnitude of the vortex stretching term when considered over the whole interior subtropics. However, much of the pointwise linear vorticity error is due to small departures that cancel out in a horizontal domain average.

5.2 Subtropical Manifestations of a Reducing AMOC

A CO₂ induced climate change scenario of the HiGEM high resolution coupled climate model has been used to investigate the hypothesis that Sverdrup balance can constrain where a reduction in deep transport is compensated in the upper subtropical ocean. Averaging between 17°N and 32°N in

the Atlantic, a steady 5.3 Sv reduction occurs in deep transports that are brought about by 70 years of increasing CO₂ levels at 2% per year. CO₂ levels are then held constant for a further 30 years, after which time the deep transports remain stable. It is found that on time scales long enough for the ocean to adjust to Sverdrup balance the southwards deep transport reduction is balanced solely by a weakening of the northwards surface western boundary current and not by a strengthening of the southwards interior ocean transport.

The transport changes are consistent with zonally integrated Sverdrup balance holding to a good approximation in the basin interior in HiGEM, as well as in ECCO-GODAE. As seen in other climate models (Lu et al., 2008) the North Atlantic subtropical wind stress curl in HiGEM weakens throughout the climate change scenario. The outcome is an average 3.0 Sv reduction between 17°N and 32°N in the Atlantic that is also compensated in the western boundary. Resultingly, western boundary transports reduce by 8.3 Sv over the first 70 years of the climate change scenario. The results suggest that long time scale monitoring of the AMOC could be achieved by observing only the western boundary and by calculating interior ocean transports according to Sverdrup balance. Such a calculation would also have to include the Antilles Current as part of the western boundary, which is not in Sverdrup balance in either HiGEM or ECCO-GODAE and which displays a strong weakening throughout the climate change scenario.

Bryden et al. (2005) found the AMOC had slowed by 30% over approximately 50 years since 1957. Although the strong AMOC variability revealed by the RAPID array (Cunningham et al., 2007) now suggests that the findings are likely a result of aliasing, historical observations do not allow for an accurate high frequency calculation of the AMOC before 2004. Since no trends are evident in the decadal time series of Florida Straits transport (Meinen et al., 2010) and wind stress curl (from NCEP reanalysis; Atkinson et al., 2010) over a similar time period, it can be concluded either that no change has occurred in the AMOC or that changes have occurred in the Antilles Current.

5.3 Subpolar AMOC Variability

The importance of ocean currents and processes of the subpolar North Atlantic for AMOC variability has been studied. There is evidence from earlier studies that various high latitude processes, such as convective mixing (e.g. Biastoch et al., 2008), Denmark Straits overflow (e.g. Gregory et al., 2005) and the cyclonic strength of the subpolar circulation (e.g. Böning et al., 2006), are important for the AMOC. Using a 120 year control run of the high resolution HiGEM model, a full investigation has been made into the relative importances of these processes for AMOC variability. Calculations of overturning in density space may be better than in depth space since flow occurs mostly along isopycnals and information on water mass transformation is contained (Mauritzen and Häkkinen, 1999; Zhang, 2010). The importance of high latitude ocean processes has therefore been studied with respect to both depth space and density space definitions of overturning.

Depth space and density space AMOC variability are very similar within tropical and subtropical latitudes. Conversely, within subpolar latitudes AMOC fluctuations are different in the two coordinate spaces both in terms of their magnitude and periods of variability. The primary focus of the study has been to determine the causes and mechanisms behind these differences, with a particular emphasis on time scales exceeding 5 years. The depth space AMOC variability is found to correlate well to the strength of the horizontal subpolar gyre circulation and to the maximum mixed layer depth (a proxy for convection) in the Labrador and Irminger seas. The density space AMOC variability is found to correlate well to the southward transport strength of the overflow through the Denmark Straits and to the maximum surface heat flux (a proxy for water mass transformation) in the Labrador Sea. The mechanism of depth space overturning is explained by a strong pointwise correlation to the transports in the western boundary. It is proposed here that a spin up of the gyre, related to doming of isopycnals in the central Labrador Sea, leads to increased deep transports in the western boundary that directly impact the depth space overturning. In contrast, the density space overturning correlates more to the densities of the western boundary current than to the transports. High densities in the boundary current, transported through the Denmark Straits as well as formed through surface water mass transformation, allows more of the southwards western

boundary transports to contribute to density space overturning. This is because higher density water in the southwards Labrador Current means that it does not cancel out with lighter eastern subpolar northwards transports once zonally integrated to get overturning.

The meridional coherence of AMOC variability has received much attention recently following some studies (Bingham et al., 2007; Lozier et al., 2010) that show the subpolar and subtropical AMOC display different periods of variability. Hydrographic observations have revealed that twenty year mean AMOC anomalies in the subpolar and subtropical gyres can fluctuate out of phase (Lozier et al., 2010). This thesis reveals that natural decadal variability, rather than the existence of any long term trends, can explain the opposing nature seen in the Lozier et al. (2010) results. The observed opposing changes may be because depth space AMOC variability can be different between the subpolar and subtropical gyres. However, the work presented here furthers the coarse resolution model study of Zhang (2010) and shows that much of the AMOC variability is meridionally coherent from subpolar to subtropical latitudes when the time scale of propagation from high to low latitudes is considered. Some indication has therefore been presented that the twenty year means of Lozier et al. (2010) may be due to capturing one cycle of variability in the subtropical gyre and only part of the same cycle in the subpolar gyre (along with a part of the next or preceding cycle). In such a case, the difference between twenty year means might result in opposing anomalies.

5.4 Wider context and Future Work

Until a high spatial density of ocean observations is available in decadal time series, state estimation products are the ideal environment in which to address the validity of Sverdrup balance. In a state estimation, observational estimates are combined into a freely running ocean model using the adjoint procedure. The result is an optimised dynamically consistent global gridded estimate that is free from adjustment discontinuities (Wunsch and Heimbach, 2007). Various potential problems of the ECCO-GODAE state estimation, however, must be accounted for when interpreting an analysis of Sverdrup balance. For example, ECCO-GODAE has a too weak deep

ocean circulation (Baehr et al., 2007). Weak transports in the deep ocean likely mean that the interaction between horizontal currents and topography, which gives rise to BPT, will also be weaker. If BPT is stronger in the real ocean then it may impact more heavily on the wind driven layer and reduce the validity of Sverdrup balance.

It is suspected that the adjoint procedure in ECCO-GODAE might introduce small scale variability into the wind stress curl (Lu and Stammer, 2004). To account for model deficiencies such as too high viscosity, the adjoint may make the winds more variable (or the ocean smoother) to account for the increased dissipation of wind energy by the ocean. Enhanced wind energy may consequently also mean that variability in the vertical velocities is enhanced due to their relationship through Ekman pumping. Indeed, vertical velocities on different parts of the model grid in ECCO-GODAE are found to be inconsistent with each other: only vertical velocities at the corner point of the grid display variability that corresponds to the wind stress curl variability. It has been shown that the assumption due to a level of no vertical motion is the largest contributor to the Sverdrup error in ECCO-GODAE, which might therefore be related to small scale unrealistic variability in the vertical velocities. It is thus recommended that future state estimation models, which might improve with the inclusion of more data (and more data types such as the RAPID array) and a move to higher resolution (Mazloff et al., 2010), are used to gain a better understanding of the realism of the small scale variability. However, an important point to consider is the similarity in the extent that Sverdrup balance holds in ECCO-GODAE and in HiGEM, despite their different horizontal resolutions. Contrary to ECCO-GODAE, the ocean component of HiGEM contains more small scale variability than the wind stress curl does. This is balanced by small scale variability in the non-linear vorticity terms in HiGEM. The error from assuming linear vorticity is therefore larger in HiGEM while the error from assuming a level of no vertical motion is higher in ECCO-GODAE. Perhaps the missing non-linear vorticity from unresolved eddies in ECCO-GODAE is merely compensated by an increase in vertical velocity (possibly because of how parameterised eddies handle horizontal flux divergence) with the result that Sverdrup balance is similar in both models. On large scale considerations in particular, the two models display a very similar Sverdrup balance.

This lends some support to whether the model representations of Sverdrup balance provide a realistic representation of the real ocean.

Some insight has been gained into the three dimensional behaviour of the currents that contribute to overturning. In the subtropical gyre AMOC changes are almost entirely manifested in the western boundary on long enough time scales for the ocean to be in Sverdrup balance. This has been demonstrated using a climate change scenario that exhibits a reducing AMOC. These results can be expected to also apply to natural decadal variability in overturning, whereby long term fluctuations in deep transport would be mirrored by changes in the western boundary transport. However, any changes that take place in the Sverdrup interior of the ocean also result in western boundary changes. A conclusion to draw from this is that if future changes are to be interpreted and understood then the full gyre must be monitored, whether through basin wide hydrographic measurements like the RAPID array or through a combined use of satellites and western boundary-only hydrographic monitoring.

The Florida Straits transport is too small in HiGEM due to poorly resolved passages into the Caribbean Sea (Shaffrey et al., 2009). Although the combined transport from the Florida and Antilles currents is reasonable in the model, the Antilles Current acts to compensate and is resultingly too large. An interesting question that can therefore not be answered using HiGEM is whether changes in the gyre transports would result in changes in the Antilles Current (as suggested by Lee et al., 1996) while changes in AMOC would result in changes in the Florida Straits transport (as suggested by Schmitz and Richardson, 1991). If AMOC changes are mostly carried in the Florida Straits, the results presented here suggest that a combined use of the Florida Straits cable (e.g. Meinen et al., 2010) with wind stress curl estimations of interior transport would be enough to monitor the AMOC on Sverdrup balance time scales. However, there is no strong evidence that all the AMOC variability is manifested in the Florida Straits. Therefore, until a better understanding is obtained of the difference in the dynamics of the Florida Straits and Antilles Current it is important to measure both.

Overturning calculations in density space provide some improvements on those made in depth space, particularly at high latitudes where significant water mass transformation occurs. Along with the finding that meridional

coherence is improved in density space, the differences between the two coordinate representations of overturning suggest that more work be done to understand density space AMOC variability. In particular, its strong dependence on the outflow through the Denmark Straits should be further explored since it implies an important connection between the AMOC in density space and the waters of the Greenland Seas and Arctic Ocean. As an example, polar water is predicted to change a great deal over the following decades due to loss of sea ice (IPCC, 2007). This may therefore be an important source of change for future overturning. A climate change scenario from a high resolution coupled model, such as HiGEM (which includes a full sea ice model), could be used to further analyse this connection.

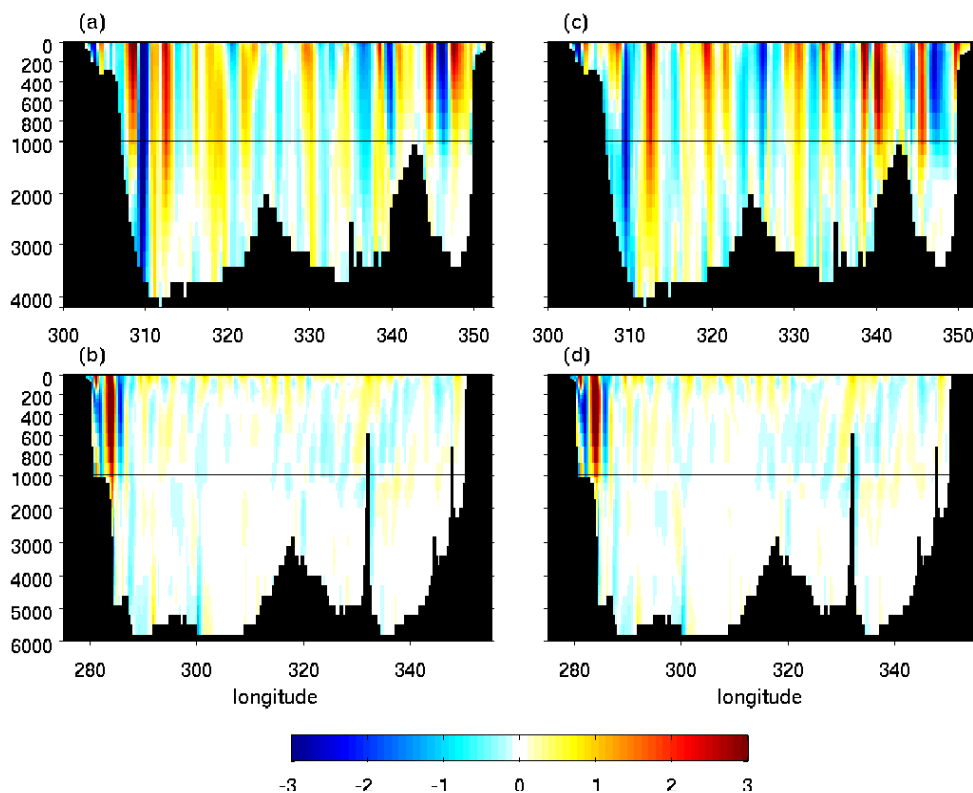


Figure 5.1: Composite difference of the meridional velocities at (a,c) 55°N and (b,d) 30°N between periods of strong and weak (a,b) depth space AMOC and (c,d) density space AMOC. Strong AMOC is defined as being stronger than 1 standard deviation above the mean and weak AMOC is 1 standard deviation below the mean. Note the change in y-axis scale at 1000 m depth. Units are m s^{-1} .

Some significant differences have been revealed in this work between the subpolar AMOC in depth and density space in HiGEM, and some clear

patterns have emerged on their relationship to western boundary transports and densities. However, more research is still required here. The annual resolution of the HiGEM output used restricts a full understanding of the mechanisms involved. This is because many of the important processes, such as convection and Denmark Straits overflow, are likely to be winter intensified. It is therefore suggested that the processes and pathways of water masses could be further elucidated through an analysis of higher temporal resolution data. For example, questions of where deep water is formed and what pathways dense water takes south of Denmark Straits could be addressed. The role of boundary waves might also be studied. The scope of possibility here is also limited by the strong reliance on correlation statistics, which may only reveal the strongest correlations. Much information might be lost regarding the sensitivity of overturning to other regions and processes of the ocean such as at the eastern boundary. This point is well demonstrated by Figure 5.1, which shows composite differences of the meridional velocities during periods of high AMOC strength (stronger than 1 standard deviation of the mean) minus velocities during low AMOC strength (weaker than 1 standard deviation of the mean). Zonal transects of the meridional velocities are shown at two latitudes, one in the subtropical gyre (at 30°N) and one in the subpolar gyre (at 55°N), for both depth and density space calculations of overturning. In the subtropical gyre, velocity changes between periods of high and low AMOC are restricted to the western boundary, in agreement with the work presented in chapter 3 of this thesis. These changes are very similar in depth and density space. In the subpolar gyre, however, strong velocity changes take place throughout the gyre and these changes are different according to the strength of the depth and density space AMOC. So although the correlation statistics indicate that only the western boundary plays a strong role in AMOC changes, there is much detail in the interior of the subpolar gyre that is yet to be understood.

The AMOC streamfunction is regularly used as an index to summarise the ocean currents and to make inferences on their climate impact. Figure 5.1 raises the question of how useful the AMOC index for representing the complex distribution of subpolar gyre currents. Subpolar AMOC changes are associated to large transports that are distributed throughout the whole

width of the basin. The AMOC at these latitudes therefore represents a relatively small residual of many strong alternating northwards and southwards transports, and so may hold no particular significance for climate. Perhaps a more three dimensional view of the circulation and its associated heat transport would provide a more accurate description of how heat is carried to higher latitudes and give a better understanding of the resulting climate impacts. The dynamics and impacts of these interior ocean subpolar transports, as well as the potential over-simplicity of the AMOC at high latitudes, should be investigated in future studies.

Chapter 6

Appendices

6.1 Appendix A: finding a Level of No Motion in ECCO-GODAE

This section describes three approaches to determine a geovarying level of no motion (LONM) where the vertical velocities are zero in the ECCO-GODAE state estimate. The aim is to try and obtain an improved calculation of Sverdrup balance relative to using a depth plane level. In Chapter 2, an analysis was made into how well Sverdrup balance describes the time mean circulation in the ECCO-GODAE state estimation. Sverdrup balance was calculated using an integration depth of 2200 m at every geographical position in the domain. This depth was determined as the optimum depth plane, optimised using the Sverdrup metrics, M_{zi} and M_{pw} (see section 2.4.3), which were calculated for all possible integration depths. Strictly speaking, this optimised depth does not give the optimum planar LONM (where velocities are smallest) but the optimum Sverdrup balance (where the Sverdrup errors are smallest). However, in the subtropics the LONM error (Δ_{LONM} ; see section 2.2) is larger than the linear vorticity error (Δ_{LV}) for all integration depths, so the optimum Sverdrup balance level also represents the optimum LONM depth plane. In reality a LONM depth, if there is one, is not expected to be a flat surface that is the same everywhere but rather one that changes according to the spatially varying wind stress curl. This raises the question of whether there exists a more accurate geovarying LONM that can be used as an integration depth in calculations of Sverdrup balance. The time mean deep ocean in ECCO-GODAE has been shown

to contain large non-wind driven vertical velocities that are not consistent with Sverdrup balance (Figure 2.1). Ideally therefore, we would want to find a near-continuous surface at a quiescent depth between wind driven upper ocean transports and deep ocean transports. Such a depth would lie at a level where both w and $\partial_z w$ are small.

Sverdrup balance requires, in the strict sense of the depth-integrated vorticity equation, a region where the vertical velocities go to zero since $\Delta_{LONM} = -fw_h/\beta$ (see section 2.2). This can theoretically therefore be a ‘zero-crossing’ depth where w equals zero but $\partial_z w$ is not zero (and so w is not zero immediately above and below the LONM). Such a zero crossing depth could be created by wind driven and BPT driven layers overlapping at some depth. If Sverdrup balance is considered to represent a depth range over which the transports are driven by the wind stress curl, such a zero-crossing depth is not considered here to be a very satisfactory LONM. This is because depths lying above the LONM would not be forced only by the wind, but by both wind and BPT. The depth of the LONM is then the result of a cancellation of transports which lies at a different location to where it would be if the layer were driven only by the wind. As such, any theoretical description of the ocean that incorporates Sverdrup theory will predict a different depth of LONM and therefore a different vertical profile. The question of whether the wind stress curl equals the transports above a zero-crossing LONM is therefore not a question of whether Sverdrup balance holds but of whether linear vorticity balance holds. Nevertheless, it is interesting to assess the difference between this ‘theoretical Sverdrup balance’ and the more practically defined Sverdrup balance that lies at a level of weak $\partial_z w$.

The first method of finding a LONM therefore finds the depth, at each geographical location, of the minimum time mean vertical velocity below the Ekman layer. The method is here called w_{min} , which gives the best possible LONM that can be achieved in the model. The depth is shown in Figure 6.2(a), and the Sverdrup errors (Δ_{SB} ; see section 2.2) that result from integrating to this depth are shown in Figure 6.1(a). For comparison, the Sverdrup errors from the optimised depth plane at 2200 m (referred to here as V_{plane}) are shown in Figure 6.1(d). Throughout the subtropics the errors in w_{min} are smaller than in V_{plane} . Values of M_{pw} , when calculated

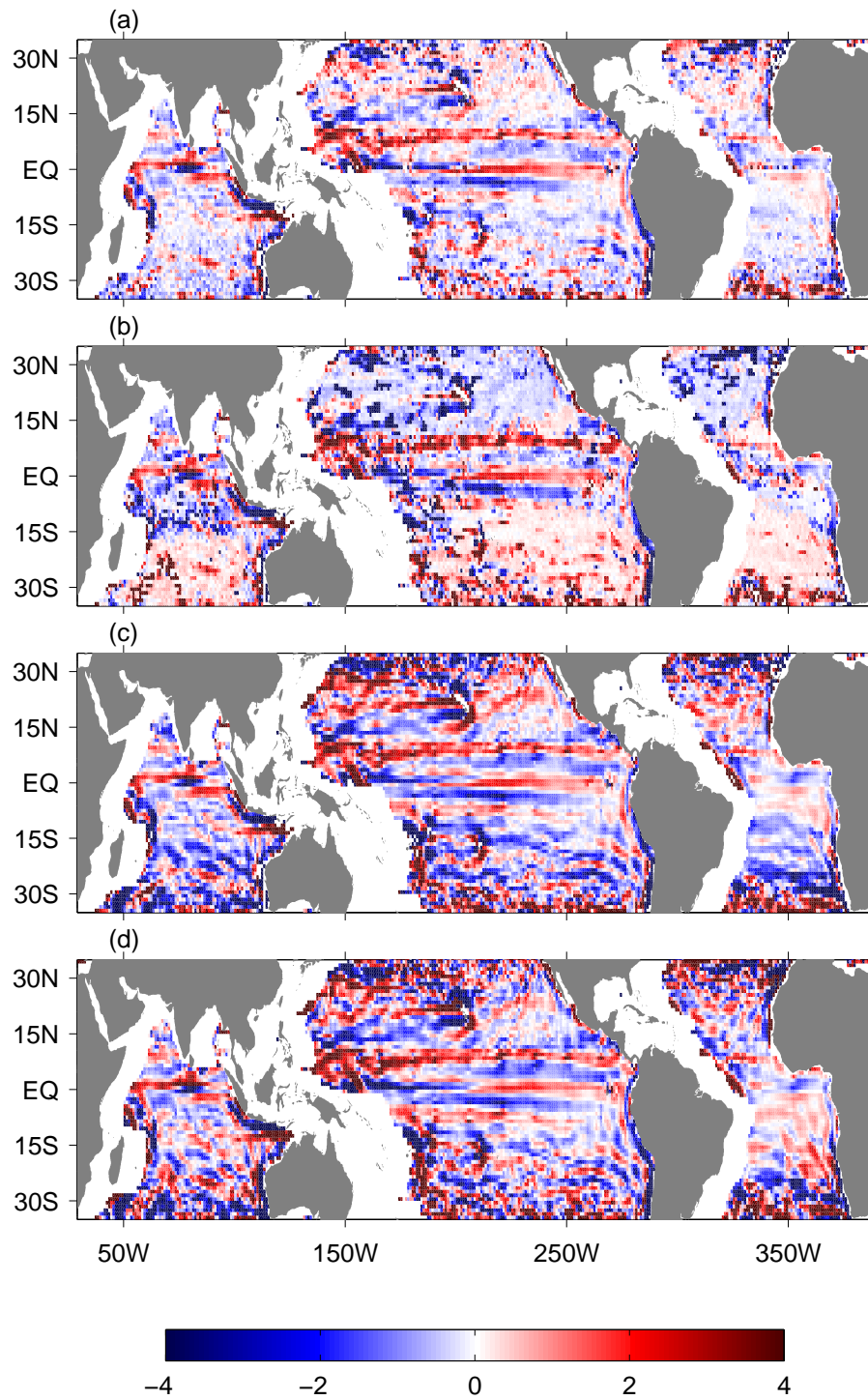


Figure 6.1: Sverdrup error, Δ_{SB} , from each of the four methods of determining a LONM in the ECCO-GODAE state estimate (a) w_{min} , (b) w_{thresh} , (c) v_{thresh} , (d) V_{plane} (see text). Units are m^2s^{-1} .

over the full masked subtropical domain, are respectively 36% and 56%. However, the LONM depth is highly variable and cannot be interpreted to

represent any physical mechanisms. As with other models, vertical velocities in ECCO-GODAE are messy (Wunsch, 2011). The w_{min} LONM is therefore unlikely to be a physically meaningful surface, but more likely a chance zero-crossing point within a noisy vertical profile.

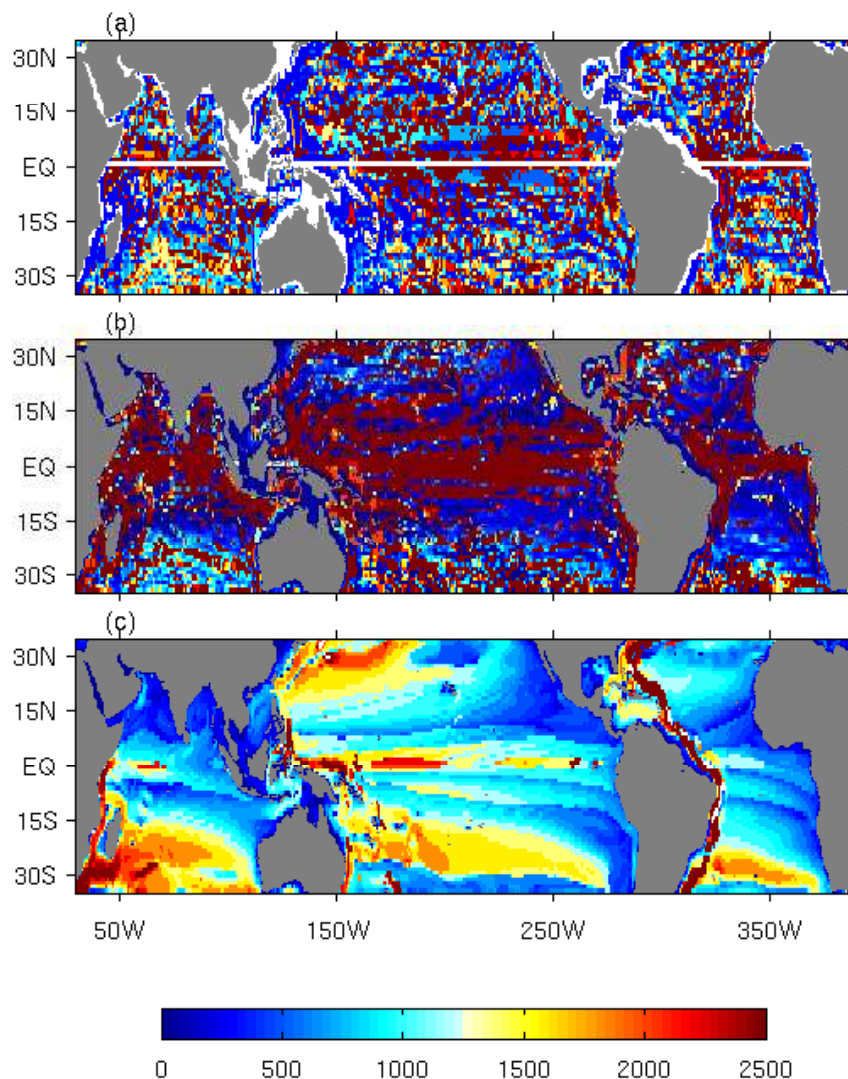


Figure 6.2: LONM from each of the four methods of determining a LONM in the ECCO-GODAE state estimate (a) w_{min} , (b) w_{thresh} , (c) v_{thresh} (see text).

The second method to find a LONM considers where both w and $\partial_z w$ become small. The inclusion of $\partial_z w$ as a constraint is hoped to reduce any issues regarding strongly variable profiles of w . The pointwise Sverdrup metric, M_{pw} , is optimised from a parameter space of w and $\partial_z w$ that are each varied from relatively low values to relatively high values. For each

combination in the parameter space of w and $\partial_z w$: 1) the shallowest depth at every location is found that exhibits w and $\partial_z w$ characteristics that are smaller than the two threshold values, 2) the Sverdrup errors are found by integrating to those depths in Sverdrup balance, 3) the value of M_{pw} is calculated. A grid of M_{pw} values is thereby created, one for each combination of w and $\partial_z w$. The smallest M_{pw} from that grid is chosen as the optimal combination of w and $\partial_z w$, for which there are associated Sverdrup errors and an associated LONM depth. It is hoped that by finding a depth at each location according to the same threshold pair, a continuous surface can be found (rather a surface that sharply changes from one location to another, as is the case for method 1; Figure 6.2a). This method is called w_{thresh} . Since the optimal Sverdrup depth is not necessarily going to be at a quiescent depth (i.e. a depth where $\partial_z w$ is small), it is important to note that at the high threshold limit of $\partial_z w$ the method limits only by w (and vice versa). However, the combination that provides the optimum M_{pw} is found when limited by both (not shown). The depths from w_{thresh} are shown in Figure 6.2(b) and the Sverdrup errors are shown in Figure 6.1(b). Despite clear regional improvements in the Sverdrup errors compared to V_{plane} , the value of M_{pw} is 0.48, only a slight improvement. This is mostly because of strong geographically localised departures where the method fails to find a LONM. There therefore appears to be some promise in this method for reducing Sverdrup errors, however, as with method w_{min} , the depths are quite variable. This is perhaps also because of the noisy nature of the vertical velocities, so it is uncertain if the depth is a good representation of the wind stress forcing.

The third method to find a LONM is identical to method two but instead uses the horizontal speed, $\sqrt{(u^2 + v^2)}$, and its vertical gradient as threshold criteria in replacement of w and $\partial_z w$. The reduced small scale noise of the horizontal velocities relative to the vertical velocities is hoped to improve the methods ability to find a physically meaningful depth. A small horizontal velocity corresponds to a small $\partial_z w$, which is not strictly a criteria for Sverdrup balance, but can be used to find a quiescent depth. This method is called v_{thresh} . The depths from v_{thresh} (Figure 6.2c) form a near continuous surface that bears some similarity to the spatial pattern of the wind driven gyres. It also exhibits some features of the Luyten et al. (1983) theory of

the thermocline depth, namely that a deep thermocline in the west of the basin that shallows eastwards. The Sverdrup errors for v_{thresh} are shown in Figure 6.1(c), for which the M_{pw} value is 0.56, the same as from V_{plane} .

Method	M_{pw} (%)	M_{zi} (%)	$\overline{M_{pw}}$ (%)	$\overline{M_{zi}}$ (%)
w_{min}	36	14	21	10
w_{thresh}	48	27	34	24
v_{thresh}	56	26	35	21
V_{plane}	56	20	31	13

Table 1: The pointwise (M_{pw}), zonally integrated (M_{zi}), 5° smoothed pointwise ($\overline{M_{pw}}$) and 5° smoothed zonally integrated ($\overline{M_{zi}}$) Sverdrup metrics for each method (a) w_{min} , (b) w_{thresh} , (c) v_{thresh} , (d) V_{plane} (see text).

The three different methods to find a LONM each find a very different surface. The methods have had some success in reducing the Sverdrup errors. Yet only from method v_{thresh} do we get a continuous surface that can be interpreted as being related to the wind, for which no improvement in the Sverdrup errors is gained relative to V_{plane} . Finding a geovarying LONM that best represents Sverdrup balance is a difficult task, and although method v_{thresh} goes some way to finding this level there is likely some improvement to be made here. However, the main point to draw from these methods is the relatively small improvement in M_{pw} that has been made compared to using a simple depth plane at 2200 m.

The results are summarised in Table 1, which shows M_{pw} and M_{zi} for each method. Also shown in Table 1 are the Sverdrup metrics for the 5° smoothed transport fields from each method (symbolised as $\overline{M_{pw}}$ and $\overline{M_{zi}}$). Differences between methods w_{thresh} , v_{thresh} and V_{plane} are minimal, particularly in considerations of the zonally integrated and smoothed fields. This is especially important given the differences in the integration depth that are output by the methods. It can therefore be concluded that so long as the ocean is everywhere integrated to below the main thermocline depth, but not so deep that non-wind driven deep transports are included, then the results are similar. Although method w_{min} gives a 20% improvement in M_{pw} relative to V_{plane} , this is the best possible LONM that can be achieved in ECCO-GODAE and is unlikely to be a level that represents the mechanisms associated to Sverdrup balance given its horizontal variability. This difference is reduced to only a 6% in M_{zi} , and on scales greater than 5°

the metrics $\overline{M_{pw}}$ and $\overline{M_{zi}}$ are respectively only different by 11% and 3% between w_{min} and V_{plane} . Any physically meaningful geovarying LONM other than that produced from v_{thresh} , if found in ECCO-GODAE, is unlikely to make a big improvement to Sverdrup balance compared to using the optimised depth plane at 2200 m, particularly in consideration of the large scale circulation.

6.2 Appendix B: calculating vertical velocities in ECCO-GODAE

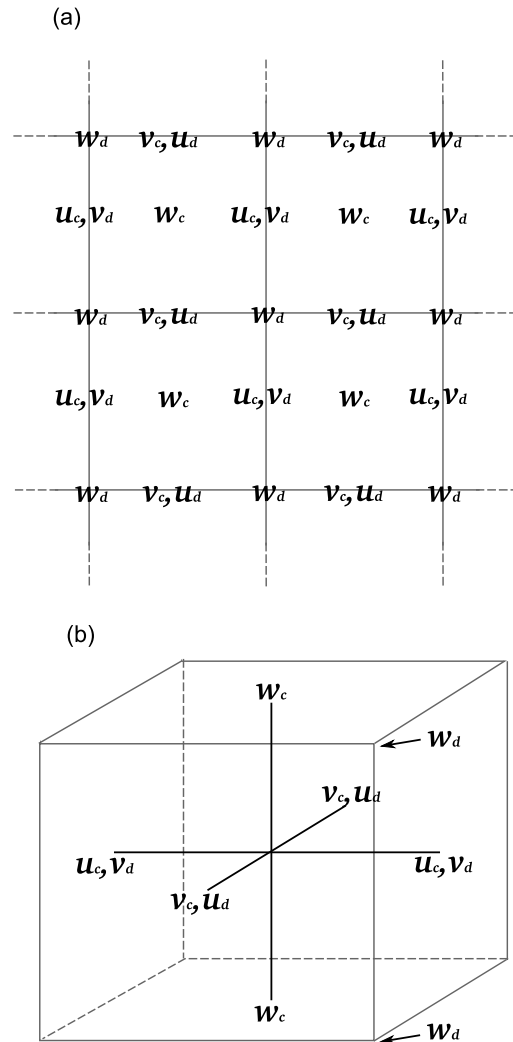


Figure 6.3: (a) The 2D horizontal and (b) 3D views of the locations of velocity variables in the Arakawa C grid and D grid configurations. Subscripts denote the grid configuration. Vertical velocities, w_c and w_d are calculated respectively as the (negative of the) vertically integrated horizontal divergence of the C grid and D grid velocities (according to the continuity equation). Cross hairs in (b) have been added as a visual aid for the location of the variables. The model spherical polar grid has here been approximated by a rectangular grid.

ECCO discretises the momentum equations using variables located on an Arakawa C grid and D grid (Figure 6.3). The C grid meridional velocities, v_c , and D grid zonal velocities, u_d , lie on the southern and northern faces of

the grid. The C grid zonal velocities, u_c , and D grid meridional velocities, v_d , lie on the east and west faces. C grid vertical velocities lie in the centres of the grid and D grid vertical velocities lie on the cell corner. All vertical velocities are located at the top and bottom of the grid cell in the vertical axis and all horizontal velocities are located in the middle of the grid cell in the vertical axis. All terms in the zonal (meridional) momentum equation are located at the point where u_c (v_c) lies. Terms in the vorticity equation lie on the corner of the grid.

The benefit of the C grid is that it retains non-divergence of the flow at all times (Arakawa and Lamb, 1977). It also aids the application of the Divergence and the Curl to the velocities, which respectively produce values in the centre and corner of the grid. A consequence of the C grid in calculations of momentum, however, is that the Coriolis term naturally lies on a different part of the grid to the remaining terms and thereby requires interpolating onto the correct grid location. Adcroft et al. (1999) demonstrated that this averaging incurs an error that grows with time. This issue is resolved in ECCO-GODAE by implementing the so-called CD-scheme, which gets its name because of the combined use of C grid and D grid velocities. By introducing two additional momentum equations that explicitly solve for zonal and meridional momentum on the D grid, the horizontal velocities arising from these equations may then be inserted into the C grid momentum equations which thereby removes the need for averaging.

In ECCO-GODAE the final three terms of equation (10) are calculated as the finite difference curl of the equivalent terms in the momentum equation. The curl of the Coriolis term gives only the difference between the first two terms of equation (10), and so the terms must be calculated separately. The first term of equation (10) is calculated as the meridional average of the D grid meridional velocities multiplied by β . The second term of equation (10) is calculated as the (negative of the) horizontal divergence of the D grid velocities multiplied by f . If the first and second terms of equation (10) are instead calculated by interpolating C grid velocities onto the cell corner then the equation will not close.

If the CD scheme is not properly accounted for then the error incurred in the 15 year mean of the momentum equation is only small. However, the error becomes relatively much larger in the vorticity equation due to

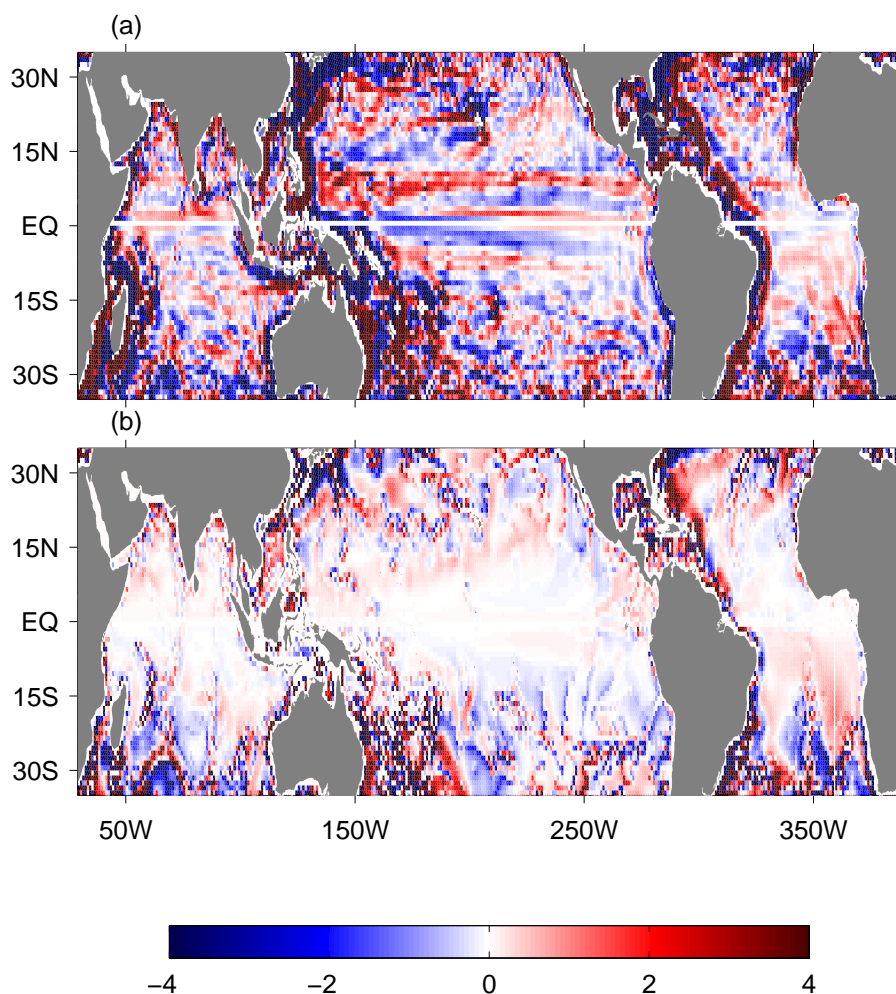


Figure 6.4: The LONM error, $\Delta_{LONM} (fw_h/\rho_0\beta)$, calculated using the (a) D grid vertical velocities and (b) C grid vertical velocities. Depth integrations are made to 2200 m. Units are in m^2s^{-1} .

large errors that arise in the second term of equation (10), with the effect that linear vorticity balance is worsened. Therefore, any calculations that involve vertical velocity will be erroneous if not calculated using the D grid velocities (Figure 6.4). It is possible that the representation of bathymetry on a staggered grid is what leads to the difference in the errors calculated from the two grids. This is because w must go to zero at the ocean floor at the grid centre, where the bathymetry is flat, but not at the cell corner, where the bathymetry is sloped.

Differences in the vertical velocity at the different grid locations may explain the inconsistencies between our study and that of Lu and Stammer (2004) who use an older version of ECCO-GODAE (that incorporates the

CD scheme). In particular, they account a much larger portion of the Sverdrup error to $\hat{\mathbf{k}} \cdot \nabla \times \text{ADV}$ (and therefore to Δ_{LV}) which they calculate as a residual of the other terms. Similarly, in the recent study by Wunsch (2011) vertical velocities at 117.5 m were used to approximate the Sverdrup transport from Ekman velocities. The C grid vertical velocities at this depth are smoother than the D grid velocities and so their use may result in an error in the estimate of the Sverdrup transport.

6.3 Appendix C: statistical methods

6.3.1 Statistical significance of a trend in data containing autocorrelation

A method for determining the statistical significance of a linear data trend that contains autocorrelation has been developed here following the work of Efron (1979). Autocorrelation is present in a data series when data points are not independent but are instead related to some extent to their neighbouring data points. A simple measure of statistical significance, such as a student's t-test, cannot be used in such a case since it assumes data points are independent. We instead use a so-called block bootstrap (Efron, 1979) method that accounts for autocorrelation when determining trend significance. This works by dividing the data into blocks that can each be considered independent from one another. The example shown in Figure 6.5 is for a time series trend, but the method can be applied to any data series.

The method works as follows:

- 1) A time series that contains a trend is detrended (Figure 6.5a).
- 2) The decorrelation time scale is calculated from the autocorrelation (Figure 6.5b). The decorrelation time is the number of time steps between two uncorrelated data points in a series. This corresponds to the shortest lag at which the correlation drops to zero. Low correlation values are not wholly trustworthy, therefore the decorrelation time scale (t_d) is taken as double the lag at which the correlation drops to 0.5.
- 3) The detrended time series is divided into blocks of length equal to $1.5t_d$ (Figure 6.5a). The factor of 1.5 is applied to ensure that whole wavelengths of correlated data points are included in each block. The division into blocks is referenced to a randomised 'start point'.
- 4) The blocked time series is re-organised into a random order and a trend is calculated.
- 5) A probability density function of possible trends is generated by repeating step (4) four thousand times (Figure 6.5c). Four thousand is considered an amount that is suitable for the purposes presented here, which uses data series less than 100 points in length, but the number of iterations should be appropriate for the length of the data series used.
- 6) The trend is considered 95% significant if the trend is greater than the

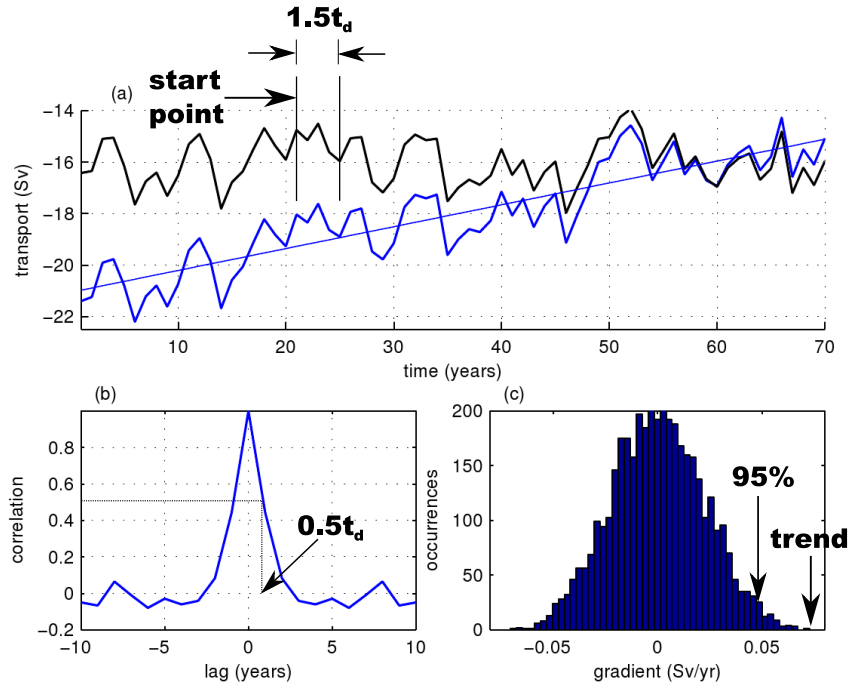


Figure 6.5: Example procedure to find the significance of a trend. (a) A data series (blue line) and detrended data series (black line; y-axis shifted for display purposes). The straight blue line shows the trend. (b) The autocorrelation of the detrended data series. (c) The probability density function of trends produced for 4000 randomly re-organised versions of the detrended data that is split into data chunks equal to $1.5t_d$ in time (see text). Time scale t_d is the decorrelation time scale. ‘95%’ marks the 95th percentile of the probability density function. ‘trend’ marks the trend of the original data trend. The trend is significant at 95% confidence if greater than the 95th percentile.

95th percentile of the probability density function (and similarly so for any other percentage significance). In this case, the trend is more significant than the 95% significance threshold.

6.3.2 Statistical significance of a correlation between data containing autocorrelation

This appendix section describes a method that has been developed to determine the significance of a correlation between two data series that contain autocorrelation. The significance of a correlation is given by $1.96/\sqrt{(N - 3)}$ (Wilks, 2011), where N is the number of degrees of freedom. If all data

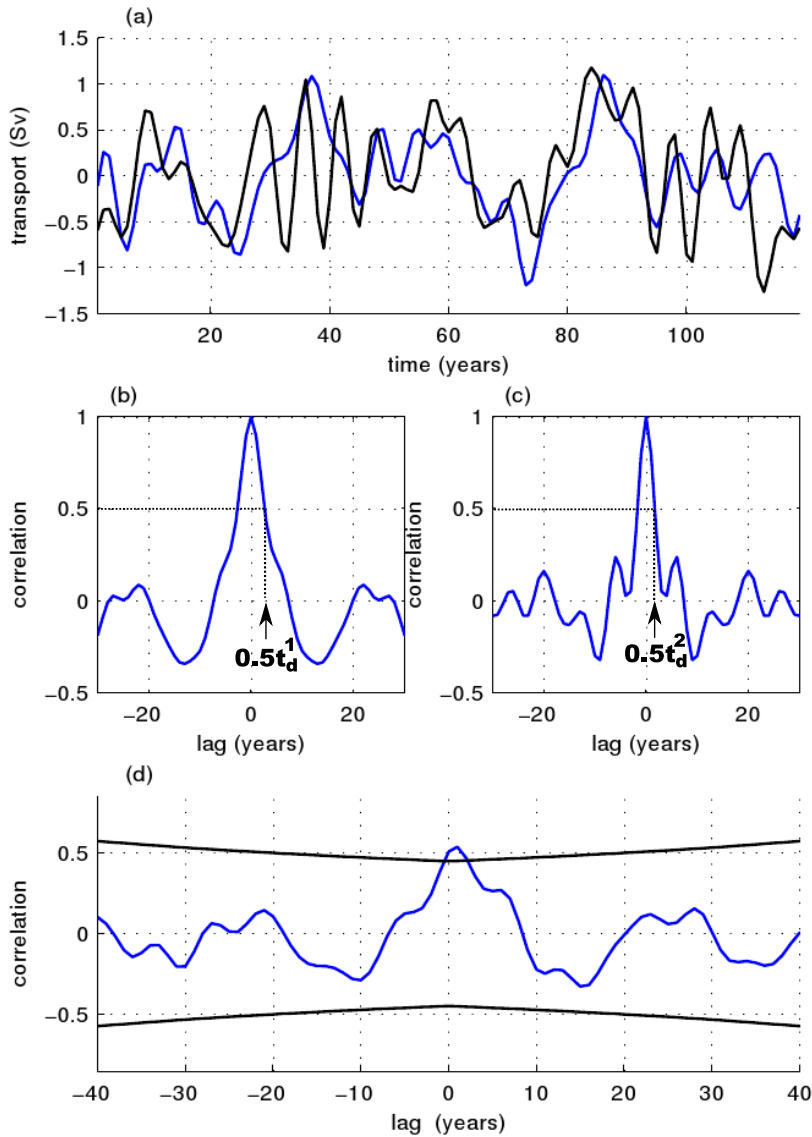


Figure 6.6: An example procedure to find the significance of a lagged correlation between two time series (blue and black curves in (a)). (b-c) The autocorrelation of the two time series. (d) The lagged correlation between the two time series (blue line) with the 95% significance level marked (black line). The correlation is significant at 95% confidence if it exceeds the 95% significance level. Time scales t_d^1 and t_d^2 are respectively the decorrelation of the two time series shown in (a).

points within either data series are independent of each other then N is equal to the number of data points in the series. If any autocorrelation is present (when any data point within a series is correlated to some extent with its neighbouring data points), then N is reduced by a factor corre-

sponding to the number of neighbouring data points that are correlated to each other. Note that for a lagged autocorrelation the number of degrees of freedom is reduced by the relative lag between the two data series. The example shown is a lagged correlation between two time series (Figure 6.6a), but the method can be applied to any two data series of equal length.

The method works as follows:

- 1) The decorrelation time scale is calculated for each time series from their respective autocorrelations (Figure 6.5b,c). The shortest lag time of zero correlation is the decorrelation time scale. Since low correlation values are not trustworthy the decorrelation time scale for each series (t_d^1 and t_d^2) is taken as double the lag at which the correlation drops to 0.5.
- 2) The largest of t_d^1 and t_d^2 is taken as the representative decorrelation time.
- 3) The number of degrees of freedom, N , is calculated as the length of the data series divided by the representative decorrelation time and minus the lag time.
- 4) The significance is calculated as $1.96/\sqrt{(N - 3)}$ (Figure 6.6d).

6.4 Appendix D: Glossary of Terms in Equations

Term	Description	Units
A_h	Coefficient of horizontal viscosity	$\text{m}^2 \text{s}^{-1}$
A_v	Coefficient of vertical viscosity	$\text{m}^2 \text{s}^{-1}$
ADV	Depth integrated advection of momentum, $\frac{1}{\beta} \int_{-h}^s \nabla \cdot (A_h \nabla \mathbf{u}) dz$, in equation (11)	$\text{m}^3 \text{s}^{-1}$
β	Meridional gradient of the coriolis parameter, $\partial_y f$	$\text{m}^{-1} \text{s}^{-1}$
BPT	Bottom Pressure Torque, $\hat{\mathbf{k}} \cdot \nabla \times (p_b \nabla H) = -fw_b$	m s^{-2}
δ_{LV}	Depth-dependent linear vorticity error term, $\hat{\mathbf{k}} \cdot \nabla \times (\nabla \cdot (A_{-h} \nabla \mathbf{u}) dz + \int_{-h}^s (\mathbf{u} \cdot \nabla) \mathbf{u} dz)$, in equation (10)	m s^{-2}
Δ_{LONM}	Level of No Motion error, $-fw_h/\beta$, in equation (11)	$\text{m}^2 \text{s}^{-1}$
Δ_{LV}	Linear Vorticity error, $\hat{\mathbf{k}} \cdot \nabla \times (\int_{-h}^s \nabla \cdot (A_{-h} \nabla \mathbf{u}) dz + \int_{-h}^s (\mathbf{u} \cdot \nabla) \mathbf{u} dz)$, in equation (11)	$\text{m}^2 \text{s}^{-1}$
Δ_{SB}	Sverdrup error, $\Delta_{LONM} + \Delta_{LV}$	$\text{m}^2 \text{s}^{-1}$
f	The Coriolis parameter	s^{-1}
H	Full depth of the ocean	m
H_i	Depth of a water column	m
HV	Depth integrated horizontal viscosity term, $\int_{-h}^s \nabla \cdot (A_h \nabla \mathbf{u}) dz$, in equation (10)	$\text{m}^3 \text{s}^{-1}$
M_{pw}	Sverdrup Balance metric for the pointwise transport field, $\frac{\langle \Delta_{SB} \rangle}{\langle \frac{\nabla \times \tau}{\rho_0 \beta} \rangle}$	%
M_{zi}	Sverdrup Balance metric for the zonally integrated transport field, $\frac{\langle \int_W^E \Delta_{SB} dx \rangle}{\langle \int_W^E \frac{\nabla \times \tau}{\rho_0 \beta} dx \rangle}$	%
p	Pressure	$\text{kg m}^{-1} \text{s}^{-2}$
p_b	Bottom pressure	$\text{kg m}^{-1} \text{s}^{-2}$
ψ_z	Atlantic meridional overturning circulation in depth space, $\int_z^0 \int_{x_{east}}^{x_{west}} v_z dx dz$	Sv

ψ_σ	Atlantic meridional overturning circulation in density space, $\int_\sigma^0 \int_{x_{east}}^{x_{west}} v_\sigma dx d\sigma$	Sv
Ψ_σ	Atlantic meridional overturning circulation in density space	Sv
$\Psi_{\sigma,lp}$	five year low pass filtered Atlantic meridional overturning circulation in density space	Sv
$\Psi_{\sigma,hp}$	five year high pass filtered Atlantic meridional overturning circulation in density space	Sv
Ψ_z	Atlantic meridional overturning circulation in depth space	Sv
$\Psi_{z,lp}$	five year low pass filtered Atlantic meridional overturning circulation in depth space	Sv
$\Psi_{z,hp}$	five year high pass filtered Atlantic meridional overturning circulation in depth space	Sv
PV	Potential Vorticity, $\frac{f+\zeta}{H}$	$\text{m}^{-1} \text{s}^{-1}$
ρ_0	constant reference density of seawater	kg m^{-3}
σ	potential density	kg m^{-3}
$\boldsymbol{\tau}$	Viscous Stress, $A_v \partial_z \mathbf{u}$	$\text{m}^2 \text{s}^{-2}$
$\boldsymbol{\tau}_s$	surface wind stress vector	$\text{kg m}^{-1} \text{s}^{-2}$
τ_s^x	zonal surface wind stress	$\text{kg m}^{-1} \text{s}^{-2}$
u	zonal velocity	m s^{-1}
\mathbf{u}	velocity vector	m s^{-1}
v	meridional velocity	m s^{-1}
v_g	meridional geostrophic velocity	m s^{-1}
v_σ	meridional velocity at density coordinate location (x, y, σ)	m s^{-1}
v_z	meridional velocity at cartesian location (x, y, z)	m s^{-1}
V	depth integrated meridional transport	$\text{m}^2 \text{s}^{-1}$
V_g	depth integrated meridional geostrophic velocity	$\text{m}^2 \text{s}^{-1}$
w	vertical velocity	m s^{-1}
w_b	bottom vertical velocity	m s^{-1}
w_E	Ekman pumping vertical velocity	m s^{-1}
w_h	vertical velocity at integration depth, $-h$	m s^{-1}

6.5 Appendix E: Glossary of Acronyms and Abbreviations

Term	Description
2%CO ₂ scenario	A 120 year climate change simulation in the HiGEM model in which atmospheric CO ₂ levels are increased at 2% per year
ADV	Depth integrated advection of momentum. See ADV in Appendix D
AMOC	Atlantic Meridional Overturning Circulation
BPT	Bottom Pressure Torque. See BPT in Appendix D
Control scenario	A 150 year control simulation in the HiGEM model
DS	Denmark Straits
DSOW	Denmark Straits Overflow Water
DSOW strength	The transport strength through the Denmark Straits below the 1037.6 kg m ⁻³ potential density (referenced to 2000 m) isopycnal. Units are m ³ s ⁻¹
DWBC	Deep Western Boundary Current
GIN seas	Greenland-Iceland-Norwegian Seas
GS	Gulf Stream
GSR	Greenland-Scotland Ridge
HV	Depth integrated horizontal viscosity term. See HV in Appendix D
Level of no motion error	See Δ_{LONM} in Appendix D
Linear vorticity error	See Δ_{LV} in Appendix D
LONM	Level Of No Motion
LSW	Labrador Sea Water
LV	Linear Vorticity

MLD	Mixed Layer Depth
NAC	North Atlantic Current
NADW	North Atlantic Deep Water
Ocean transport	See V in Appendix D
PV	Potential Vorticity. See PV in Appendix D
SHF	Surface Heat Flux
Sv	Unit of Sverdrups (m^3s^{-1})
SPG	Subpolar Gyre
SPG strength	the maximum barotropic streamfunction in the subpolar gyre in Sverdrups
STG	Subtropical Gyre
Sverdrup error	See Δ_{SB} in Appendix D
Sverdrup transport	$\hat{\mathbf{k}} \cdot \nabla \times \boldsymbol{\tau}_s$
WBC	Western Boundary Current
WMT	Water Mass Transformation

Chapter 7

Bibliography

- Adcroft, A. J., C. N. Hill, and J. C. Marshall, 1999: A new treatment of the coriolis terms in C-grid models at both high and low resolutions. *Monthly Weather Review*, **127** (8), 1928–1936.
- Anderson, D. L. T. and A. E. Gill, 1975: Spin-Up Of A Stratified Ocean, With Applications To Upwelling. *Deep-Sea Research*, **22** (9), 583–596.
- Anderson, D. L. T. and P. D. Killworth, 1977: Spin-Up Of A Stratified Ocean, With Topography. *Deep-Sea Research*, **24** (8), 709–732.
- Aoki, K. and K. Kutsuwada, 2008: Verification of the wind-driven transport in the North Pacific subtropical gyre using gridded wind-stress products. *Journal Of Oceanography*, **64** (1), 49–60.
- Arakawa, A. and V. R. Lamb, 1977: Computational design of the basic dynamical processes of the UCLA general circulation model. *Methods in Computational Physics*, **17**, 173–265.
- Atkinson, C. P., H. L. Bryden, J. J. M. Hirschi, and T. Kanzow, 2010: On the seasonal cycles and variability of Florida Straits, Ekman and Sverdrup transports at 26 degrees N in the Atlantic Ocean. *Ocean Science*, **6** (4), 837–859.
- Baehr, J., S. Cunningham, H. Haak, P. Heimbach, T. Kanzow, and J. Marotzke, 2009: Observed and simulated estimates of the meridional overturning circulation at 26.5 degrees N in the Atlantic. *Ocean Science*, **5** (4), 575–589.

- Baehr, J., H. Haak, S. Alderson, S. A. Cunningham, J. H. Jungclauss, and J. Marotzke, 2007: Timely detection of changes in the meridional overturning circulation at 26 degrees N in the Atlantic. *Journal Of Climate*, **20 (23)**, 5827–5841.
- Bailey, D. A., P. B. Rhines, and S. Häkkinen, 2005: Formation and pathways of north atlantic deep water in a coupled ice-ocean model of the arctic-north atlantic oceans. *Climate Dynamics*, **25 (5)**, 497–516.
- Biastoch, A., C. W. Böning, J. Getzlaff, J. M. Molines, and G. Madec, 2008: Causes of Interannual-Decadal Variability in the Meridional Overturning Circulation of the Midlatitude North Atlantic Ocean. *Journal of Climate*, **21 (24)**, 6599–6615.
- Bingham, R. J., C. W. Hughes, V. Roussenov, and R. G. Williams, 2007: Meridional coherence of the North Atlantic meridional overturning circulation. *Geophysical Research Letters*, **34 (23)**.
- Blaker, A. T., J. J. . M. Hirschi, B. Sinha, B. de Cuevas, S. Alderson, A. Coward, and G. Madec, 2012: Large near-inertial oscillations of the Atlantic meridional overturning circulation. *Ocean Modelling*, **42**, 50–56.
- Böning, C. W., R. Döscher, and H. J. Isemer, 1991: Monthly Mean Wind Stress And Sverdrup Transports In The North-Atlantic - A Comparison Of The Hellerman-Rosenstein And Isemer-Hasse Climatologies. *Journal Of Physical Oceanography*, **21 (2)**, 221–235.
- Böning, C. W., M. Scheinert, J. Dengg, A. Biastoch, and A. Funk, 2006: Decadal variability of subpolar gyre transport and its reverberation in the North Atlantic overturning. *Geophysical Research Letters*, **33 (21)**, L21S01.
- Bower, A. S., M. S. Lozier, S. F. Gary, and C. W. Böning, 2009: Interior pathways of the North Atlantic meridional overturning circulation. *Nature*, **459 (7244)**, 243–U126.
- Boyer, T., S. Levitus, J. Antonov, R. Locarnini, A. Mishonov, H. Garcia, and S. A. Josey, 2007: Changes in freshwater content in the North Atlantic Ocean 1955-2006. *Geophysical Research Letters*, **34 (16)**.

-
- Broecker, W. S., 1987: The Biggest Chill. *Natural History*, **96** (10), 74–8.
- Bryan, F. O., C. W. Böning, and W. R. Holland, 1995: On The Midlatitude Circulation In A High-Resolution Model Of The North-Atlantic. *Journal Of Physical Oceanography*, **25** (3), 289–305.
- Bryden, H. L., 1980: Geostrophic Vorticity Balance In Midocean. *Journal Of Geophysical Research-Oceans And Atmospheres*, **85** (NC5), 2825–2828.
- Bryden, H. L., H. R. Longworth, and S. A. Cunningham, 2005: Slowing of the Atlantic meridional overturning circulation at 25 degrees N. *Nature*, **438** (7068), 655–657.
- Buckley, M. W., D. Ferreira, J.-M. Campin, J. Marshall, and R. Tulloch, 2012: On the relationship between decadal buoyancy anomalies and variability of the Atlantic Meridional Overturning Circulation. *Journal of Climate*, **In press**.
- Catto, J. L., L. C. Shaffrey, and K. I. Hodges, 2011: Northern Hemisphere Extratropical Cyclones in a Warming Climate in the HiGEM High-Resolution Climate Model. *Journal of Climate*, **24** (20), 5336–5352.
- Chelton, D. B., M. G. Schlax, M. H. Freilich, and R. F. Milliff, 2004: Satellite measurements reveal persistent small-scale features in ocean winds. *Science*, **303** (5660), 978–983.
- Cubasch, E., et al., 2001: *Climate Change 2001: The Scientific Basis. Contribution of Working Group 1 to the Third Assessment Report of the Intergovernmental Panel on Climate Change*, chap. Projections of future climate change, 525–582. Cambridge University Press, New York.
- Cunningham, S. A. and R. Marsh, 2010: Observing and modeling changes in the Atlantic MOC. *Wiley Interdisciplinary Reviews-Climate Change*, **1** (2), 180–191.
- Cunningham, S. A., et al., 2007: Temporal variability of the Atlantic meridional overturning circulation at 26.5 degrees N. *Science*, **317** (5840), 935–938.

- Curry, R. G. and M. S. McCartney, 2001: Ocean gyre circulation changes associated with the North Atlantic Oscillation. *Journal Of Physical Oceanography*, **31** (12), 3374–3400.
- Curry, R. G., M. S. McCartney, and T. M. Joyce, 1998: Oceanic transport of subpolar climate signals to mid-depth subtropical waters. *Nature*, **391** (6667), 575–577.
- de Boer, A. M., 2010: OCEANOGRAPHY Sea change. *Nature Geoscience*, **3** (10), 668–669.
- de Boer, A. M. and H. L. Johnson, 2007: Inferring the zonal distribution of measured changes in the meridional overturning circulation. *Ocean Science*, **3**, 55–57.
- de Boer, A. M., J. R. Toggweiler, and D. M. Sigman, 2008: Atlantic dominance of the meridional overturning circulation. *Journal Of Physical Oceanography*, **38** (2), 435–450.
- Delworth, T. L. and M. E. Mann, 2000: Observed and simulated multidecadal variability in the Northern Hemisphere. *Climate Dynamics*, **16** (9), 661–676.
- Dickson, B., I. Yashayaev, J. Meincke, B. Turrell, S. Dye, and J. Holfort, 2002: Rapid freshening of the deep North Atlantic Ocean over the past four decades. *Nature*, **416** (6883), 832–837.
- Dickson, R. R. and J. Brown, 1994: The Production of North-Atlantic Deep-water - Sources, Rates, and Pathways. *Journal of Geophysical Research-oceans*, **99** (C6), 12 319–12 341.
- Döös, K. and D. J. Webb, 1994: The Deacon Cell and the Other Meridional Cells of the Southern Ocean. *Journal Of Physical Oceanography*, **24**, 429–442.
- Eden, C. and J. Willebrand, 2001: Mechanism of interannual to decadal variability of the North Atlantic circulation. *Journal Of Climate*, **14** (10), 2266–2280.
- Efron, B., 1979: 1977 Rietz Lecture - Bootstrap Methods - Another Look At The Jackknife. *Annals Of Statistics*, **7** (1), 1–26.

-
- Eldevik, T., J. E. O. Nilsen, K. A. Iovino, D. and Olsson, A. B. Sandø, and H. Drange, 2009: Observed sources and variability of Nordic seas overflow. *Nature Geoscience*, **2** (6), 405–409.
- Ganachaud, A. and C. Wunsch, 2000: Improved estimates of global ocean circulation, heat transport and mixing from hydrographic data. *Nature*, **408** (6811), 453–457.
- Ganachaud, A. and C. Wunsch, 2003: Large-scale ocean heat and freshwater transports during the World Ocean Circulation Experiment. *Journal of Climate*, **16** (4), 696–705.
- Gary, S. F., M. S. Lozier, C. W. Böning, and A. Biastoch, 2011: Deciphering the pathways for the deep limb of the Meridional Overturning Circulation. *Deep Sea Research II*, **58**, 1781–1797.
- Gent, P. R., W. G. Large, and F. O. Bryan, 2001: What sets the mean transport through Drake Passage? *Journal Of Geophysical Research-Oceans*, **106** (C2), 2693–2712.
- Getzlaff, K., C. W. Böning, and J. Dengg, 2006: Lagrangian perspectives of deep water export from the subpolar North Atlantic. *Geophysical Research Letters*, **33** (21), L21S08.
- Gill, A. E., 1982: *Atmosphere-Ocean Dynamics*. Academic Press, San Diego.
- Godfrey, J. S. and T. J. Golding, 1981: The Sverdrup Relation In The Indian-Ocean, And The Effect Of Pacific-Indian Ocean Throughflow On Indian-Ocean Circulation And On The East Australian Current. *Journal Of Physical Oceanography*, **11** (6), 771–779.
- Gregory, J. M., et al., 2005: A model intercomparison of changes in the Atlantic thermohaline circulation in response to increasing atmospheric CO₂ concentration. *Geophysical Research Letters*, **32** (12).
- Griffies, S. M., 2004: *Fundamentals of Ocean Climate Models*. Princeton University Press.
- Häkkinen, S. and P. B. Rhines, 2004: Decline of subpolar North Atlantic circulation during the 1990s. *Science*, **304** (5670), 555–559.

- Häkkinen, S., P. B. Rhines, and D. L. Worthen, 2011: Warm and saline events embedded in the meridional circulation of the northern North Atlantic. *Journal Of Geophysical Research-Oceans*, **116**, C03006.
- Hátún, H., A. B. Sandø, H. Drange, B. Hansen, and H. Valdimarsson, 2005: Influence of the Atlantic subpolar gyre on the thermohaline circulation. *Science*, **309** (5742), 1841–1844.
- Hautala, S. L., D. H. Roemmich, and W. J. Schmitz, 1994: Is The North Pacific In Sverdrup Balance Along 24-Degrees-N. *Journal Of Geophysical Research-Oceans*, **99** (C8), 16041–16052.
- Hirschi, J., J. Baehr, J. Marotzke, J. Stark, S. Cunningham, and J. O. Beismann, 2003: A monitoring design for the Atlantic meridional overturning circulation. *Geophysical Research Letters*, **30** (7), 1413.
- Hodson, D. L. R. and R. T. Sutton, 2012: The Impact of Resolution on the Adjustment and Decadal Variability of the Atlantic Meridional Overturning Circulation in a Coupled Climate Model. *Climate Dynamics*.
- Hughes, C. W. and B. A. de Cuevas, 2001: Why western boundary currents in realistic oceans are inviscid: A link between form stress and bottom pressure torques. *Journal Of Physical Oceanography*, **31** (10), 2871–2885.
- Hurrell, J. W., 1995: Decadal trends in the North Atlantic Oscillation regional temperatures and precipitation. *Science*, **269**, 676–679.
- IPCC, 2007: *Climate Change 2007: The Physical Science Basis. Contribution of working group 1 to the fourth assessment report of the IPCC*. Cambridge University Press.
- Jayne, S. R. and J. Marotzke, 2001: The dynamics of ocean heat transport variability. *Reviews Of Geophysics*, **39** (3), 385–411.
- Jiang, H., H. Wang, J. Zhu, and B. Tan, 2006: Relationship between real meridional volume transport and Sverdrup transport in the North Subtropical Pacific. *Chinese Science Bulletin*, **51** (14), 1757–1760.
- Johns, T. C., et al., 2006: The new Hadley Centre Climate Model (HadGEM1): Evaluation of coupled simulations. *Journal Of Climate*, **19** (7), 1327–1353.

-
- Johns, W. E., et al., 2011: Continuous, Array-Based Estimates of Atlantic Ocean Heat Transport at 26.5 degrees N. *Journal Of Climate*, **24** (10), 2429–2449.
- Johnson, H. L. and D. P. Marshall, 2002: A theory for the surface Atlantic response to thermohaline variability. *Journal of Physical Oceanography*, **32** (4), 1121–1132.
- Josey, S. A., E. C. Kent, and P. K. Taylor, 2002: Wind stress forcing of the ocean in the SOC climatology: Comparisons with the NCEP-NCAR, ECMWF, UWM/COADS, and Hellerman and Rosenstein Datasets. *Journal Of Physical Oceanography*, **32** (7), 1993–2019.
- Kanzow, T., et al., 2007: Observed flow compensation associated with the MOC at 26.5 degrees N in the Atlantic. *Science*, **317** (5840), 938–941.
- Kieke, D., B. Klein, L. Stramma, M. Rhein, and K. P. Koltermann, 2009: Variability and propagation of Labrador Sea Water in the southern sub-polar North Atlantic. *Deep-Sea Research Part I-Oceanographic Research Papers*, **56** (10), 1656–1674.
- Kieke, D., M. Rhein, L. Stramma, W. M. Smethie, J. L. Bullister, and D. A. LeBel, 2007: Changes in the pool of Labrador Sea Water in the subpolar North Atlantic. *Geophysical Research Letters*, **34** (6), L06 605.
- Köhl, A. and D. Stammer, 2008: Variability of the meridional overturning in the North Atlantic from the 50-year GECCO state estimation. *Journal Of Physical Oceanography*, **38** (9), 1913–1930.
- Kuhlbrodt, T., A. Griesel, M. Montoya, A. Levermann, M. Hofmann, and S. Rahmstorf, 2007: On the driving processes of the Atlantic meridional overturning circulation. *Reviews Of Geophysics*, **45** (1).
- Landsteiner, M. C., M. J. McPhaden, and J. Picaut, 1990: On The Sensitivity Of Sverdrup Transport Estimates To The Specification Of Wind Stress Forcing In The Tropical Pacific. *Journal Of Geophysical Research-Oceans*, **95** (C2), 1681–1691.
- Langehaug, H. R., 2011: Circulation and transformation of Atlantic and Arctic Water Masses. Ph.D. thesis, University of Bergen.

- Large, W. G., J. C. McWilliams, and S. C. Doney, 1994: Oceanic Vertical Mixing - A Review And A Model With A Nonlocal Boundary-Layer Parameterization. *Reviews Of Geophysics*, **32** (4), 363–403.
- Latif, M., C. Böning, J. Willebrand, A. Biastoch, J. Dengg, N. Keenlyside, U. Schweckendiek, and G. Madec, 2006: Is the thermohaline circulation changing? *Journal of Climate*, **19** (18), 4631–4637.
- Lee, T. N., W. E. Johns, R. J. Zantopp, and E. R. Fillenbaum, 1996: Moored observations of western boundary current variability and thermohaline circulation at 26.5 degrees N in the subtropical north Atlantic. *Journal Of Physical Oceanography*, **26** (6), 962–983.
- Leetmaa, A. and A. F. Bunker, 1978: Updated Charts Of Mean Annual Wind Stress, Convergences In Ekman Layers, And Sverdrup Transports In North-Atlantic. *Journal Of Marine Research*, **36** (2), 311–322.
- Leetmaa, A., P. Niiler, and H. Stommel, 1977: Does the Sverdrup Relation Account for the Mid-Atlantic Circulation. *Journal Of Marine Research*, **35** (1), 1–10.
- Leetmaa, A., P. Niiler, and H. Stommel, 1981: *Evolution of Physical Oceanography: Scientific Surveys in Honor of Henry Stommel*, chap. Equatorial currents: observations and theories, 184–196. MIT Press.
- Levitus, S., 1982: Climatological atlas of the world ocean. *NOAA prof. paper*, U.S. Govt. Printing Office.
- Levitus, S., J. Antonov, and T. Boyer, 2005: Warming of the world ocean, 1955-2003. *Geophysical Research Letters*, **32** (2).
- Levitus, S., J. I. Antonov, T. P. Boyer, and C. Stephens, 2000: Warming of the world ocean. *Science*, **287** (5461), 2225–2229.
- Lohmann, K., H. Drange, and M. Bentsen, 2009: A possible mechanism for the strong weakening of the North Atlantic subpolar gyre in the mid-1990s. *Geophysical Research Letters*, **36**, L15 602.
- Lozier, M. S., 2010: Deconstructing the Conveyor Belt. *Science*, **328** (5985), 1507–1511.

-
- Lozier, M. S., V. Roussenov, M. S. C. Reed, and R. G. Williams, 2010: Opposing decadal changes for the North Atlantic meridional overturning circulation. *Nature Geoscience*, **3** (10), 728–734.
- Lu, J., G. Chen, and D. M. W. Frierson, 2008: Response of the Zonal Mean Atmospheric Circulation to El Nino versus Global Warming. *Journal Of Climate*, **21** (22), 5835–5851.
- Lu, Y. Y. and D. Stammer, 2004: Vorticity balance in coarse-resolution global ocean simulations. *Journal Of Physical Oceanography*, **34** (3), 605–622.
- Luyten, J., H. Stommel, and C. Wunsch, 1985: A Diagnostic Study Of The Northern Atlantic Subpolar Gyre. *Journal Of Physical Oceanography*, **15** (10), 1344–1348.
- Luyten, J. R., J. Pedlosky, and H. Stommel, 1983: The Ventilated Thermocline. *Journal Of Physical Oceanography*, **13** (2), 292–309.
- Marotzke, J., R. Giering, K. Q. Zhang, D. Stammer, C. Hill, and T. Lee, 1999: Construction of the adjoint MIT ocean general circulation model and application to Atlantic heat transport sensitivity. *Journal Of Geophysical Research-Oceans*, **104** (C12), 29 529–29 547.
- Marotzke, J. and B. A. Klinger, 2000: The dynamics of equatorially asymmetric thermohaline circulations. *Journal Of Physical Oceanography*, **30** (5), 955–970.
- Marotzke, J. and J. R. Scott, 1999: Convective mixing and the thermohaline circulation. *Journal Of Physical Oceanography*, **29** (11), 2962–2970.
- Marsh, R., B. A. de Cuevas, A. C. Coward, J. Jacquin, J. J.-M. Hirschi, Y. Aksenov, A. J. G. Nurser, and S. A. Josey, 2009: Recent changes in the North Atlantic circulation simulated with eddy-permitting and eddy-resolving ocean models. *Ocean Modelling*, **28** (4), 226–239.
- Marshall, D. P. and J. C. Stephens, 2001: On the insensitivity of the wind-driven circulation to bottom topography. *Journal Of Marine Research*, **59** (1), 1–27.

- Marshall, J., C. Hill, L. Perelman, and A. Adcroft, 1997: Hydrostatic, quasi-hydrostatic, and nonhydrostatic ocean modeling. *Journal Of Geophysical Research-Oceans*, **102 (C3)**, 5733–5752.
- Mauritzen, C. and S. Häkkinen, 1999: On the relationship between dense water formation and the "Meridional Overturning Cell" in the North Atlantic Ocean. *Deep Sea Research I*, **46**, 877–894.
- Mazloff, M., P. Heimbach, and C. Wunsch, 2010: An Eddy-Permitting Southern Ocean State Estimate. *Journal of Physical Oceanography*, **40**, 880–899.
- McCarthy, G. D., et al., 2012: Observed interannual variability of the Atlantic meridional overturning circulation at 26.5 degrees N,. *Geophysical Research Letters*, **In Press**.
- Medhaug, I., H. R. Langehaug, T. Eldevik, T. Furevik, and M. Bentsen, 2011: Mechanisms for Decadal Scale Variability in a Simulated Atlantic Meridional Overturning Circulation. *Climate Dynamics*, **39**, 77–93.
- Meinen, C. S., M. O. Baringer, and R. F. Garcia, 2010: Florida Current transport variability: An analysis of annual and longer-period signals. *Deep-sea Research Part I-oceanographic Research Papers*, **57 (7)**, 835–846.
- Meinen, C. S., S. L. Garzoli, W. E. Johns, and M. O. Baringer, 2004: Transport variability of the Deep Western Boundary Current and the Antilles Current off Abaco Island, Bahamas. *Deep-Sea Research Part I-Oceanographic Research Papers*, **51 (11)**, 1397–1415.
- Munk, W. and C. Wunsch, 1998: Abyssal recipes II: energetics of tidal and wind mixing. *Deep-Sea Research Part I-Oceanographic Research Papers*, **45 (12)**, 1977–2010.
- Pedlosky, 1987: *Geophysical FLuid Dynamics*. Springer.
- Rahmstorf, S., 1997: Risk of sea-change in the Atlantic. *Nature*, **388 (6645)**, 825–826.

-
- Rhein, M., et al., 2011: Deep water formation, the subpolar gyre, and the meridional overturning circulation in the subpolar North Atlantic. *Deep Sea Research II*, **58**, 1819–1832.
- Robson, J., R. Sutton, K. Lohmann, D. Smith, and M. D. Palmer, 2012: Causes of the Rapid Warming of the North Atlantic ocean in the mid 1990s. *Journal Of Climate*, **in press**.
- Roemmich, D. and C. Wunsch, 1985: Two transatlantic sections: meridional circulation and heat flux in the subtropical North Atlantic Ocean. *Deep-Sea Research*, **32 (6)**, 619–664.
- Roussenov, V. M., R. G. Williams, C. W. Hughes, and R. J. Bingham, 2008: Boundary wave communication of bottom pressure and overturning changes for the North Atlantic. *Journal Of Geophysical Research-Oceans*, **113 (C8)**, C08 042.
- Saenko, O. A., A. Schmittner, and A. J. Weaver, 2004: The Atlantic-Pacific seesaw. *Journal Of Climate*, **17 (11)**, 2033–2038.
- Saunders, P. M., S. A. Cunningham, B. A. de Cuevas, and A. C. Coward, 2008: Decadal changes in the North Atlantic and pacific meridional overturning circulation and heat flux. *Journal Of Physical Oceanography*, **38 (9)**, 2104–2107.
- Schmitz, W. J. and P. L. Richardson, 1991: On The Sources Of The Florida Current. *Deep-Sea Research Part A-Oceanographic Research Papers*, **38**, S379–S409.
- Schmitz, W. J., J. D. Thompson, and J. R. Luyten, 1992: The Sverdrup Circulation For The Atlantic Along 24-Degrees-N. *Journal Of Geophysical Research-Oceans*, **97 (C5)**, 7251–7256.
- Searl, Y., H. T. Banks, S. Stark, and R. A. Wood, 2007: Slowing of the Atlantic meridional overturning circulation: A climate model perspective. *Geophysical Research Letters*, **34 (3)**.
- Shaffrey, L. C., et al., 2009: UK HiGEM: The New UK High-Resolution Global Environment Model-Model Description and Basic Evaluation. *Journal of Climate*, **22 (8)**, 1861–1896.

- Smethie, W. M., R. A. Fine, A. Putzka, and E. P. Jones, 2000: Tracing the flow of North Atlantic Deep Water using Chlorofluorocarbons. *Journal of Geophysical Research-Oceans*, **105**, 14 297–14 323.
- Smith, D. M., S. Cusack, A. W. Colman, C. K. Folland, G. R. Harris, and J. M. Murphy, 2007: Improved surface temperature prediction for the coming decade from a global climate model. *Science*, **317 (5839)**, 796–799.
- Spence, P., O. A. Saenko, W. Sijp, and M. H. England, 2012: The Role of Bottom Pressure Torques on the Interior Pathways of North Atlantic Deep Water. *Journal Of Physical Oceanography*, **42 (1)**, 110–125.
- Stommel, H. and A. B. Arons, 1960: On The Abyssal Circulation Of The World Ocean .1. Stationary Planetary Flow Patterns On A Sphere. *Deep-Sea Research*, **6 (2)**, 140–154.
- Stommel, H., P. Niiler, and D. Anati, 1978: Dynamic Topography And Recirculation Of The North-Atlantic. *Journal Of Marine Research*, **36 (3)**, 449–468.
- Sverdrup, H. U., 1947: Wind-Driven Currents In A Baroclinic Ocean - With Application To The Equatorial Currents Of The Eastern Pacific. *Proceedings Of The National Academy Of Sciences Of The United States Of America*, **33 (11)**, 318–326.
- Tailleux, R. and J. C. McWilliams, 2001: The effect of bottom pressure decoupling on the speed of extratropical, baroclinic Rossby Waves. *Journal Of Physical Oceanography*, **31 (6)**, 1461–1476.
- Thomas, M. D., A. M. de Boer, D. P. Stevens, and H. L. Johnson, 2012: Upper Ocean Manifestations of a Reducing Meridional Overturning Circulation. *Geophysical Research Letters*, **39**.
- Thorpe, R. B., J. M. Gregory, T. C. Johns, R. A. Wood, and J. F. B. Mitchell, 2001: Mechanisms determining the Atlantic thermohaline circulation response to greenhouse gas forcing in a non-flux-adjusted coupled climate model. *Journal of Climate*, **14 (14)**, 3102–3116.

-
- Toggweiler, J. R. and B. Samuels, 1995: Effect Of Drake Passage On The Global Thermohaline Circulation. *Deep-Sea Research Part I-Oceanographic Research Papers*, **42 (4)**, 477–500.
- Townsend, T. L., H. E. Hurlburt, and P. J. Hogan, 2000: Modeled Sverdrup flow in the North Atlantic from 11 different wind stress climatologies. *Dynamics Of Atmospheres And Oceans*, **32 (3-4)**, 373–417.
- Trenberth, K. E. and J. M. Caron, 2001: Estimates of meridional atmosphere and ocean heat transports. *Journal of Climate*, **14 (16)**, 3433–3443.
- Vellinga, M. and R. A. Wood, 2002: Global climatic impacts of a collapse of the Atlantic thermohaline circulation. *Climatic Change*, **54 (3)**, 251–267.
- Wilks, D., 2011: *Statistical Methods in the Atmospheric Sciences, 3rd Edition*. Academic Press.
- Wood, R. A., M. Vellinga, and R. Thorpe, 2003: Global warming and thermohaline circulation stability. *Philosophical Transactions of the Royal Society of London Series A-mathematical Physical and Engineering Sciences*, **361 (1810)**, 1961–1974.
- Wunsch, C., 1996: *The Ocean Circulation Inverse Problem*. Cambridge University Press.
- Wunsch, C., 2011: The decadal mean ocean circulation and Sverdrup balance. *Journal Of Marine Research*, **69 (2-3)**, 417–434.
- Wunsch, C. and P. Heimbach, 2006: Estimated decadal changes in the North Atlantic meridional overturning circulation and heat flux 1993–2004. *Journal Of Physical Oceanography*, **36 (11)**, 2012–2024.
- Wunsch, C. and P. Heimbach, 2007: Practical global oceanic state estimation. *Physica D-Nonlinear Phenomena*, **230 (1-2)**, 197–208.
- Wunsch, C. and D. Roemmich, 1985: Is The North-Atlantic In Sverdrup Balance. *Journal Of Physical Oceanography*, **15 (12)**, 1876–1880.

- Zhai, X., H. L. Johnson, and D. P. Marshall, 2011: A Model of Atlantic Heat Content and Sea Level Change in Response to Thermohaline Forcing. *Journal of Climate*, **24** (21), 5619–5632.
- Zhang, R., 2008: Coherent surface-subsurface fingerprint of the Atlantic meridional overturning circulation. *Geophysical Research Letters*, **35** (20), L20705.
- Zhang, R., 2010: Latitudinal dependence of Atlantic meridional overturning circulation (AMOC) variations. *Geophysical Research Letters*, **37**, L16703.
- Zhang, R. and G. K. Vallis, 2007: The role of bottom vortex stretching on the path of the north Atlantic western boundary current and on the northern recirculation gyre. *Journal Of Physical Oceanography*, **37** (8), 2053–2080.